A NUMERICAL STUDY OF INCOMPRESSIBLE NAVIER-STOKES EQUATIONS IN THREE-DIMENSIONAL CYLINDRICAL COORDINATES

DISSERTATION

Presented in Partial Fulfillment of the Requirements for

the Degree Doctor of Philosophy in the

Graduate School of The Ohio State University

By

Douglas Xuedong Zhu, B.S., M.S.

* * * * *

The Ohio State University

2005

Dissertation Committee:

Seppo A. Korpela, Professor, Adviser

John Yu, Associate Professor

Shoichiro Nakamura, Professor

Robert H. Essenhigh, Professor

Approved by

Adviser

Graduate Program in
Mechanical Engineering

ABSTRACT

This dissertation is on a numerical study in primitive variables of three-dimensional Navier-Stokes equations and energy equation in an annular geometry. A fast direct method is developed to solve the Poisson equation for pressure with Neumann boundary conditions in radial and axial directions, and periodic boundary conditions in azimuthal direction. The velocities and temperature are solved using Douglas-Gunn ADI method, which makes use of an implicit Crank-Nicholson scheme to discretize the governing equations. The numerical method developed in this study, after being validated by comparing the numerical solutions to analytical known solutions and results published in the literature, is then used to study thermocapillary convection, Reyleigh-Bénard convection, and Taylor-Couette flow.

In the thermocapillary convection in an annulus with heated inner cylinder, the free surface was assumed to be flat. The resulting flow is two-dimensional and axisymmetric. The flow becomes three-dimensional when a θ dependent temperature boundary condition is applied on the inner cylinder.

Numerical solution of Rayleigh-Bénard convection in a shallow annular disk results in two-dimensional axisymmetric flow when the Rayleigh number is above a critical

value. A layer of concentric rolls are formed encircling the inner cylinder. The axisymmetricity and concentricity are destroyed by an initial temperature disturbance at a single grid point, or a non-uniform boundary condition on the bottom.

Numerical solution of Taylor-Couette flow results in a series of axisymmetric toroidal rolls which encircle the inner cylinder between the cylinders and are stacked in the axial direction when Taylor number exceeds a critical value. As Taylor number further increases, the flow becomes non-axisymmetric and azimuthal waves are formed and superimposed on the Taylor vortices (wavy vortex flow).

This is dedicated to my mother, wife, and daughters

ACKNOWLEDGMENTS

I want to express my sincerest appreciation to Professor Seppo Korpela for his advice, encouragement, and patience throughout this work during the years both when I was in school and after I left school. Professor Korpela always encourages me, always makes him available for review and discussion, and always asks good but tough questions.

I am thankful to Dr. V. Babu for his early related work, and many helpful discussions. I am also thankful to the committee members Professor John Yu, Professor Shoichiro Nakamura, and Professor Robert Essenhigh for their comments and valuable time.

I would like to express my appreciation to NASA Lewis Center that funded this study while I was a full time student, and to Honeywell International and Ford Motor Company who provided tuition assistance during my employment.

VITA

1963	Born in Juxian, Shandong, China
1984	B.S.Ch.E, East China University of Science & Technology, Shanghai, China
1991	MSME, The Ohio State University, Columbus, OH
1984-1989	Engineer, Research Institute of Fertilizer Industry, Linton, Shaanxi, China
1989-1993	Graduate Research Associate, Dept. of Mechanical Engineering, The Ohio State University, Columbus, OH
1993-1996	Project Engineer, Honeywell Filters & Spark Plugs, Perrysburg, OH
1996-2000	Engineering Specialist, Honeywell Engines & Systems, Phoenix, AZ
2000-present	Product Design Engineer, Ford Sustainable Mobility Technologies, Dearborn, MI

PUBLICATIONS

Research Publications

1. D.W. Shaw, X. Zhu, M.K. Misra and R.H. Essenhigh, "Determination of Global Kinetics of Coal Volatiles Combustion", 23rd Symposium (International) on Combustion, The Combustion Institute, (1990).

2. X. Zhu, "Engineering Kinetics of Coal Volatiles Combustion", M.S. Thesis, The Ohio State University, Columbus, OH, (1990).

FIELDS OF STUDY

Major Field: Mechanical Engineering

TABLE OF CONTENTS

Page

Abstract ii

Dedication iv

Acknowledgments v

Vita vi

List of Tables xi

List of Figures xii

Chapters:

1. INTRODUCTION 1

    1.1 Literature survey 1
    1.2 Objective of this study 7

2. MATHEMATICAL FORMULATION 9

    2.1 Physical description of the problem 9
    2.2 Governing equations 11
    2.3 Boundary conditions 14
        2.3.1 Boundary conditions for thermocapillary convection 14
        2.3.2 Other boundary conditions 16
    2.4 Poisson equation of pressure 18

3. NUMERICAL METHOD 21

3.1 Overview of numerical methods 21
3.1.1 Projection method 22
3.1.2 Pressure Poisson equation method 26
3.2 Grid generation 28
3.3 Fast direct inversion of pressure Poisson equation 31
3.3.1 Discretization 32
3.3.2 Matrix decomposition 34
3.4 Finite difference method to solve for velocities and temperature . . 50
3.4.1 Crank-Nicholson scheme 50
3.4.2 ADI scheme 52
3.5 Summary of the algorithm 54

4. CODE VALIDATION 56

4.1 Introduction 56
4.2 Solutions of Poisson equations 56
4.3 Couette flow in a tall annulus with a rotating inner cylinder 57
4.4 Natural convection in a tall annulus with a heated inner wall 60
4.5 Flow in a lid-driven annulus 62
4.6 Computer performance 66

5. THERMOCAPILLARY CONVECTION 70

5.1 Introduction 70
5.2 Thermocapillary convection with uniform thermal boundary condition 71
5.3 Thermocapillary convection with non-uniform thermal boundary condition 74

6. THERMAL CONVECTION IN A SHALLOW CAVITY HEATED FROM BELOW (RAYLEIGH-BÉNARD CONVECTION) 79

6.1 Introduction 79
6.2 Rayleigh-Bénard convection study with the two-dimensional axisymmetric code 81
6.2.1 Effect of aspect ratio 82
6.2.2 Effect of Rayleigh number 84
6.3 Rayleigh-Bénard convection study with the three-dimensional code 87
6.3.1 Rayleigh-Bénard convection with an initial temperature disturbance 88

6.3.2 Rayleigh-Bénard convection with non-uniform boundary condition . . . 95

7. TAYLOR-COUETTE FLOW . . . 99

7.1 Introduction . . . 99
7.2 Taylor vortex flow . . . 102
7.3 Wavy vortex flow . . . 106

8. CONCLUSION AND DISCUSSION . . . 118

Appendices:

A. FREE SURFACE DEFLECTION . . . 121

A.1 Overview . . . 121
A.2 Formulation . . . 122
A.2.1 Kinematic condition . . . 122
A.2.2 Dynamic conditions . . . 123
A.2.3 Energy balance . . . 127
A.2.4 Global mass conservation . . . 127
A.2.5 Boundary conditions for free surface deflection . . . 128
A.3 Numerical method . . . 128
A.3.1 Grid transformation . . . 130
A.3.2 Normal stress iteration . . . 130

Bibliography . . . 134

LIST OF TABLES

Table **Page**

4.1 CPU time to run the three-dimensional code 69

4.2 CPU time to run the axisymmetric code 69

LIST OF FIGURES

Figure **Page**

2.1 Schematic of the system 10

3.1 Grid representations. 29

4.1 Numerical solution of pressure Poisson equation in comparison to the analytical solution on $z = 0$, 0.5 and 1. 58

4.2 Numerical solution of pressure Poisson equation in comparison to the analytical solution on $r = 0.1$, 0.55 and 1 and $z = 0.5$. 58

4.3 Numerical solution of pressure Poisson equation in comparison to the analytical solution on $\theta = 0$, $\pi/6$ and $\pi/3$ and $r = 0.55$. 59

4.4 Numerical solution of Couette flow. 61

4.5 Temperature and velocity contours of natural convection in a tall annulus. 63

4.6 Temperature and velocity plot along the radial gap in comparison to the analytical solutions. Natural convection in a tall annulus. 64

4.7 Numerical solution for a flow in a lid driven annulus. 67

4.8 Comparison of numerical solution with literature data for flows a lid driven cavity for $Re = 100$. 68

5.1 Numerical solution of thermocapillary convection. 73

5.2 Plots of velocity variation along r and z coordinates in thermocapillary convection. 75

5.3 Velocity and temperature contours of thermocapillary convection with non-uniform thermal boundary condition on the inner cylinder. 77

5.4 Velocities and temperature vary with θ at different radii in thermocapillary convection with non-uniform boundary thermal condtition. . . . 78

6.1 Contour plots and streamlines of Rayleigh-Bénard convection in a shallow annulus. 83

6.2 Streamline plots at different time steps. 85

6.3 Temperature and velocity varying with time on the middle height ($z = 1/2$) and three radii. 86

6.4 Temperature and velocity contours on $z = 0.5$. 89

6.5 Temperature and velocity contours on $\theta = 0$. 90

6.6 Temperature and velocity contours on $z = 0.5$. An initial temperature disturbance was applied at the center grid on $\theta = \pi$. 92

6.7 Vertical (axial) velocity contours on a several θ sections. 93

6.8 Vertical (axial) velocity contours on three surfaces along the radius. . 94

6.9 Temperature and velocity contours on $z = 0.5$. Non-uniform thermal boundary condition on the bottom surface. 97

6.10 Temperature and velocity contours on $\theta = 0$. 98

7.1 Velocity contours of Taylor vortex flow. 104

7.2 Isometric view of radial velocity contours in the middle of the gap. . . 105

7.3 Streamlines at different time steps. 107

7.4 Radial and axial velocities varies with non-dimensional time on three points inside the gap. 108

7.5 The velocity norms vary with non-dimensional time. 109

7.6 Radial velocity contours in the mid gap at time 100. 111

7.7 Velocity contours in the mid gap at time 100. 112

7.8 Velocity contours on $\theta = 0$ at time 100. 113

7.9 Radial velocity contours on the mid gap at time 10 and 50. 115

7.10 Time variation of the velocity components and their norms 116

CHAPTER 1

INTRODUCTION

This dissertation is on a numerical study in primitive variables of three-dimensional Navier-Stokes equations and energy equation in an annular geometry. A fast direct method is developed to solve the Poisson equation for pressure with Neumann boundary conditions in radial and axial directions, and periodic boundary conditions in azimuthal direction. The velocities and temperature are solved using Douglas-Gunn ADI method, which makes use of an implicit Crank-Nicholson scheme to discretize the governing equations. The numerical method developed in this study, after being validated by comparing the numerical solutions to analytical known solutions or results published in the literature, is then used to solve different convection problems including thermocapillary convection and Reyleigh-Bénard convection, and to study the Taylor-Couette flow.

1.1 Literature survey

Extensive numerical studies using the Navier-Stokes equations to solve general flow problems can be attributed to the general availability of digital computer since 1960's.

However, the early numerical methods of the incompressible viscous flow were mainly based on two-dimensional stream function - vorticity formulation. This began in 1963 with the work of Fromm and Harlow [26], who developed an explicit forward difference method based on the stream function-vorticity formulation of viscous flow problems. Kawaguti [34] (see [14]) in 1961 using stream function - vorticity formulation studied flow in a lid-driven square cavity using central differences, and obtained numerical solutions for the range of Reynolds number $Re = 0$ to 64, but was unable to obtain a convergent solution for a larger Reynolds number. Burggraf [14] in 1966 by changing Kawaguti's iteration procedure, obtained convergent solutions at a higher Reynolds number ($Re = 400$). Studies of thermocapillary flows are of more recent origin. Zebib et al. [67] in 1985 solved the vorticity transport equation for large Marangoni number flows, in a two-dimensional square cavity for surface tension-driven problems. They studied flow of fluids for a range of Prandtl numbers and for Reynolds number up to $50,000$. Later Ramanan [55] and Ramanan and Korpela [56], using stream function - vorticity approach and a multi-grid method, studied natural convection in a tall vertical cavity in two-dimensional rectangular coordinates and thermocapillary convection in an axisymmetric weld pool.

The major limitation of the stream function - vorticity approach is that it is only applicable in two-dimensional coordinates. However, for three-dimensional flows the stream function generalizes to a vector potential. Thus Aziz and Hellums [7] in 1967 introduced the three-dimensional vorticity - vector potential formulation by transforming the Navier-Stokes equations into equations of vorticity and vector potential. Using this method, they obtained solutions for three-dimensional natural convection

in a cavity by solving the three vorticity transport equations using alternating direction implicit method (ADI), and three Poisson equations for the three vector potential components using iterative methods. In 1973 Mallinson and de Vahl David [40] presented solutions of three dimensional natural convection in a cavity using the vorticity - vector potential formulation with a false transient, similar to Chorin's artificial compressibility method [17].

Dennis et al. [24] in 1979 studied the flow in a lid driven cavity by formulating the problem in terms of the velocity and vorticity, and presented solutions for Reynolds number up to 100. Agarwal [3] in 1981 solved the lid-driven cavity problem using the velocity-vorticity formulation. He set the time derivatives to zero in the vorticity transport equations and solved the resulting set of elliptic equations for the velocity and vorticity using an alternating direction line-iterative scheme. In 1987, Osswald et al. [49] implemented the velocity-vorticity formulation to study the flow in a lid-driven cavity using Gaussian elimination algorithm to solve for Poisson equations for the velocity components and a modified ADI method to solve the vorticity transport equations. Similar to the vorticity-vector potential methods, one needs to solve six equations (three vorticity transport equations and three Poisson equations of velocity components) for the six unknowns (three velocity components and three vorticity components).

Numerical methods in primitive variables can be traced to late 1960's. Pioneering work was carried out by Harlow and Welch in 1965 [33], who developed the pressure Poisson equation for pressure and then solved for velocity field in a two-dimensional

cavity with free surface by advancing in time the unsteady momentum equations in primitive variables in two-dimensional Cartesian coordinates. Chorin [17] in 1967 proposed the artificial compressibility method by adding a time derivative of the pressure divided by a large constant to the incompressible continuity equation so as to enable the use of standard compressible flow techniques. Using this technique, Chorin studied steady three-dimensional convection patterns in a liquid layer heated from below. The following year, Chorin proposed a projection method to solve the three-dimensional convection in primitive variables [18]. Adopting some of the concepts proposed in these studies, Patankar and Spalding [51] developed an implicit formulation in terms of primitive variables. Takami and Kuwahara [64] studied a three-dimensional flow in a lid-driven cavity using primitive variable formulation. Their method is a variant of Chorin's splitting method [18] on a staggered grid. They presented solutions for Reynolds numbers equal to 100 and 400. Goda [30] also studied the same problem with a method based on an ADI scheme to solve the momentum equation. Babu [8] and Babu and Korpela [9] developed a fast direct method in non-uniform rectangular domains to solve the pressure Poisson equation in Cartesian coordinates, and then calculated the velocity and temperature in primitive variables in a three-dimensional cubic cavity.

The advantages of primitive variable formulation are its straightforwardness and the fact that only four variables (u,v,w, and p) need to be solved. They arise from the four equations - three momentum equations and the continuity equation. Actually Poisson equation for pressure is derived from them and it replaces the continuity equation. However, a major difficulty in primitive variable formulation is the poor

convergence of the Neumann problem of pressure Poisson equation if the traditional relaxation method is used [1], [32]. Briley [11] identified the reason for this poor convergence; namely the pressure field in the discretized form may not satisfy the integral constraint from Green's theorem. He proposed a remedy , which consists of adding a term uniformly at all grid points to the source term of the Poisson equation that satisfies the solvability condition in discretized form to machine accuracy at each time step. With this modification, Briley [11], Ghia et al. [29], Ghia et al. [27], and Adballah [2] were able to obtain converged steady state solutions for the incompressible Navier-Stokes equations. Miyakoda recommended [46] (see [1]) that the boundary conditions be incorporated directly into the finite-difference scheme at interior points adjacent to the boundaries. One popular approach is to use staggered grids, as was done in Harlow and Welch's formulation, in which the continuity equation is satisfied in each cell. It is known that solution methods for the incompressible Navier-Stokes equations based on traditional non-staggered grid, in which all the variables are defined at the cell center, may produce spurious oscillations in the pressure field, or "the checkerboard" pattern [50]. One of the fundamental causes is that, in a traditional non-staggered grid, a straightforward discretization of the continuity equation does not enforce mass conservation in the cell and causes decoupling of the pressure field between adjacent grids. To prevent the decoupling, Zang and Street [66] developed a numerical method in a non-staggered grid by defining the volume flux on its corresponding face of the cell in addition to the velocity components at the cell center.

Most numerical studies for incompressible Navier-Stokes equations have been in Cartesian coordinates. In three-dimensional cylindrical coordinates the periodic boundary

conditions destroy the simple structure of a banded matrix by two extra elements on the corners. Strikwerda and Nagel [63] studied fluid-filled cylinders undergoing spinning and coning motion by solving the steady three-dimensional incompressible Navier-Stokes equations and the continuity equation (rather than transformed pressure equation) in cylindrical coordinates by approximating the derivatives using finite difference method in the radial and axial directions but as a Fourier series in the angular direction.

In recent years, projection methods based on Hodge decomposition have become popular. The method was originally described by Chorin [18], [19] where he first estimated the velocity field by neglecting the pressure term, then corrected it by solving pressure Poisson equation by assuring the velocity field to be divergence free. Based on this method, Kim and Moin [36] developed a projection method, where they first solved an intermediate velocity field by ignoring the pressure gradient, and then updated the new velocity by projecting the intermediate velocity to the divergence free field. Bell et al. [10] formulated a similar method, but the pressure was included when calculating the intermediate velocity field, and the new pressure and velocity are updated by projecting the intermediate velocity to the divergence free field. Brown et al. [13] studied a class of projection methods, including these two and pointed that projection methods although second order in time and space for velocity, are only first order in time for pressure. They improved the projection method to have second order in time for pressure as well. They also compared the projection methods with the pressure Poisson equation formulation, and concluded the mathematical differences

between them to be very subtle. The major differences are the number of fractional steps and the order in which they are taken.

1.2 Objective of this study

The objective of this study was to extend the work of Babu [8] to cylindrical coordinates. Thus this research continues the work of Babu and Korpela [9] for convection problems, by extending their work to three-dimensional cylindrical coordinates with non-uniformed grids and for annular geometries.

The detailed objectives of the studies in this dissertation include:

- Develop and code a fast direct method to solve Poisson equation in three-dimensional cylindrical coordinates. This method is used to solve for pressure in Navier-Stokes equations in cylindrical coordinates. This effort extends the numerical method developed by Babu and Korpela [9] in rectangular coordinates to three-dimensional cylindrical coordinates.

- Develop and code a numerical method and solve Navier-Stokes equations and energy equation in three-dimensional cylindrical coordinates to solve for velocity and temperature variables.

- Verify the numerical codes by solving problems for which the solutions are known analytically, or have been published.

- Use the numerical code to study flow problems including thermocapillary convection in an annulus, free convection in a shallow annular disc (Rayleigh-Bénard convection), and flow in a tall narrow annulus with a rotating inner cylinder (Taylor-Couette flow).

CHAPTER 2

MATHEMATICAL FORMULATION

In this chapter, the formulation for solving three-dimensional incompressible Navier-Stokes equations and energy equation in cylindrical coordinates is given. The formulation and the numerical method described in the next chapter are derived for thermocapillary problem, but it is valid for general incompressible viscous flow. The first three sections describe the problem description, the formulation of the general governing equations, and the velocity and temperature boundary conditions. The last section presents the pressure Poisson equation derived from the momentum equations and the continuity equation.

2.1 Physical description of the problem

Consider an incompressible liquid of density ρ, kinematic viscosity ν, and thermal diffusivity α, confined to an annular container of inner radius r_i, outer radius r_o, and height H (Fig. 2.1). The boundary conditions depend on the particular problem to be studied.

First consider the thermocapillary convection. The outer cylinder, inner cylinder, and the bottom surface are fixed. The top surface of the liquid is free and in contact with

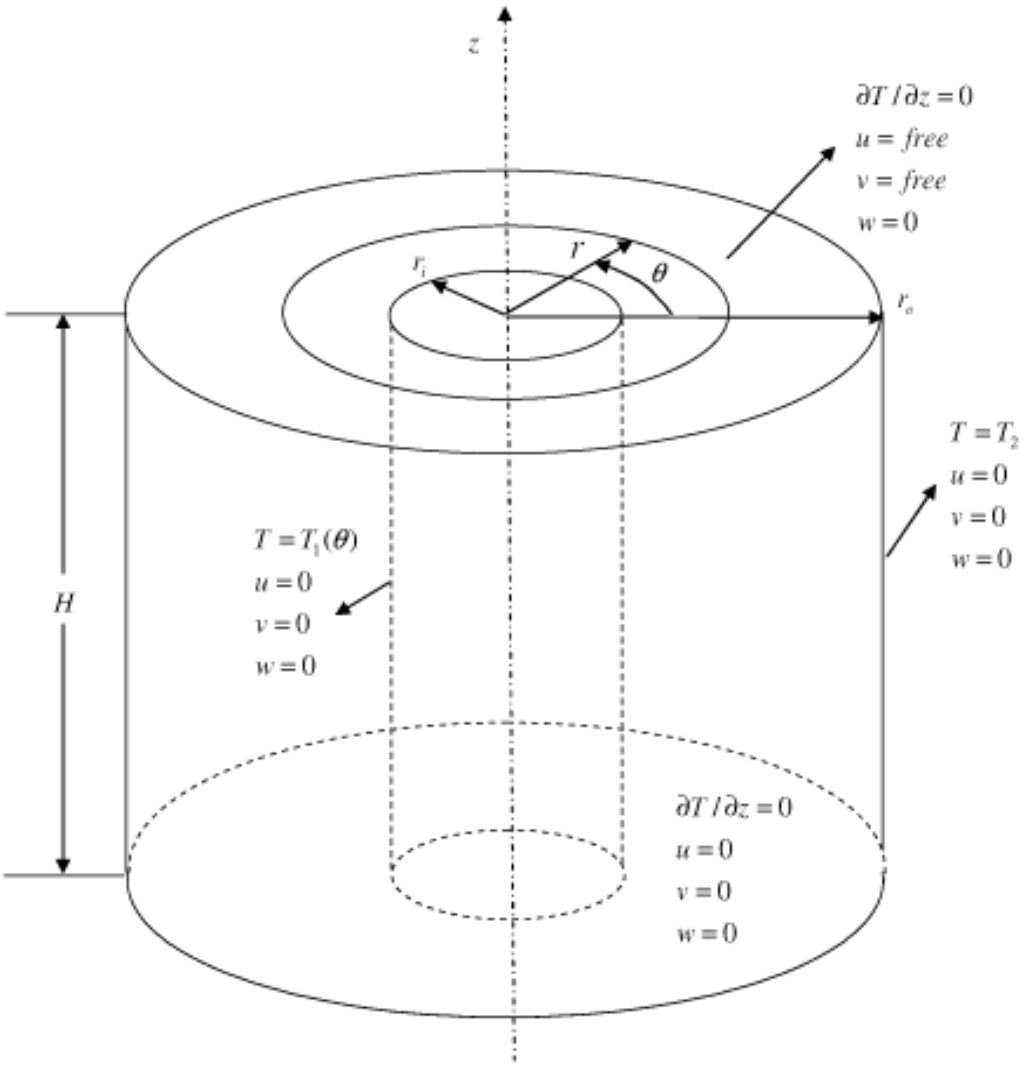

Figure 2.1: Schematic of the system

a gas above. The inner and the outer cylinder walls are maintained at fixed temperatures T_1 and T_2, respectively, such that the inner wall is hotter than the outer one ($T_1 > T_2$). Assume the bottom wall to be insulated, and the liquid-gas interface to have negligible heat transfer. A temperature variation on the free surface induces a thermocapillary stress. This causes liquid to be pulled from the hot side to the cold side. The surface stress induces viscous stresses that cause the interior motions.

Lid-driven flow problem is very similar to the problem of thermocapillary convection, except the velocity on the top surface is not caused by surface tension, but it is driven by moving surfaces of known velocity. A variation of lid-driven flow problem is flow in an annulus with rotating inner cylinder (Taylor-Couette flow), which is one of the subjects in this study.

Natural convection in an annular enclosure includes two types of boundary conditions. The first type is similar to thermocapillary convection but with a fixed upper surface. The inner cylinder is heated and the top and bottom surfaces are insulated. The analytical solution for a tall annulus is known and the solution is used to partially validate the numerical code. The second type is Rayleigh-Bénard convection in a shallow annular disk heated from the bottom. This is also considered in this study.

2.2 Governing equations

The equations that govern the motion of the fluid are the incompressible Navier-Stokes equations and the energy equation. The non-dimensionalized equations in three-dimensional cylindrical coordinates are the continuity equation

$$\frac{1}{r}\frac{\partial(ru)}{\partial r}+\frac{1}{r}\frac{\partial v}{\partial\theta}+\frac{\partial w}{\partial z}=0 \tag{2.1}$$

the momentum equations using Boussinesq approximation,

$$\begin{aligned}\frac{\partial u}{\partial t}+u\frac{\partial u}{\partial r}+\frac{v}{r}\frac{\partial u}{\partial\theta}-\frac{v^2}{r}+w\frac{\partial u}{\partial z}&=-\frac{\partial p}{\partial r}\\ &+\frac{1}{Re}\left\{\frac{\partial}{\partial r}\left[\frac{1}{r}\frac{\partial(ru)}{\partial r}\right]+\frac{1}{r^2}\frac{\partial^2 u}{\partial\theta^2}-\frac{2}{r^2}\frac{\partial v}{\partial\theta}+\frac{\partial^2 u}{\partial z^2}\right\}\end{aligned} \tag{2.2}$$

$$\begin{aligned}\frac{\partial v}{\partial t}+u\frac{\partial v}{\partial r}+\frac{v}{r}\frac{\partial v}{\partial\theta}+\frac{uv}{r}+w\frac{\partial v}{\partial z}&=-\frac{1}{r}\frac{\partial p}{\partial\theta}\\ &+\frac{1}{Re}\left\{\frac{\partial}{\partial r}\left[\frac{1}{r}\frac{\partial(rv)}{\partial r}\right]+\frac{1}{r^2}\frac{\partial^2 v}{\partial\theta^2}+\frac{2}{r^2}\frac{\partial u}{\partial\theta}+\frac{\partial^2 v}{\partial z^2}\right\}\end{aligned} \tag{2.3}$$

$$\begin{aligned}\frac{\partial w}{\partial t}+u\frac{\partial w}{\partial r}+\frac{v}{r}\frac{\partial w}{\partial\theta}+w\frac{\partial w}{\partial z}&=-\frac{\partial p}{\partial z}\\ &+\frac{1}{Re}\left\{\frac{1}{r}\frac{\partial}{\partial r}\left(r\frac{\partial w}{\partial r}\right)+\frac{1}{r^2}\frac{\partial^2 w}{\partial\theta^2}+\frac{\partial^2 w}{\partial z^2}\right\}+\frac{Gr}{Re^2}T\end{aligned} \tag{2.4}$$

and the energy equation

$$\frac{\partial T}{\partial t}+u\frac{\partial T}{\partial r}+\frac{v}{r}\frac{\partial T}{\partial\theta}+w\frac{\partial T}{\partial z}=\frac{1}{Ma}\left\{\frac{1}{r}\frac{\partial}{\partial r}\left(r\frac{\partial T}{\partial r}\right)+\frac{1}{r^2}\frac{\partial^2 T}{\partial\theta^2}+\frac{\partial^2 T}{\partial z^2}\right\} \tag{2.5}$$

where

$$Re=\frac{U_R H}{\nu} \tag{2.6}$$

$$Pr=\frac{\nu}{\alpha} \tag{2.7}$$

$$Gr = \frac{g\beta(T_1 - T_2)H^3}{\nu^2} \tag{2.8}$$

are Reynolds, Prandtl, and Grashof numbers, respectively. The Marangoni number is given by

$$Ma = RePr = \frac{U_R H}{\alpha} \tag{2.9}$$

where

$$U_R = \frac{\gamma(T_1 - T_2)}{\mu} \tag{2.10}$$

is a reference velocity for thermocapillary flow. It is obtained by putting the boundary condition at the free surface into non-dimensional forms, a step that will be explained in the next section. The reference velocity for lid-driven flow or Taylor-Couette flow is the prescribed velocity of the moving surface. The reference velocity for natural convection problem is defined by:

$$U_R = \frac{g\beta(T_1 - T_2)H^2}{\nu} \tag{2.11}$$

which makes the Reynolds number (Re) be identical to the Grashof number (Gr) for natural convection, and Marangoni number is to be replaced by Rayleigh number (Ra).

The other reference quantities used in the non-dimensionalization are annulus height H for length (r and z), H/U_R for time, and $\rho {U_R}^2$ for pressure. The dimensionless temperature is defined by:

$$T' = \frac{T - T_2}{T_1 - T_2} \tag{2.12}$$

where the T_1 is the inner wall or bottom surface temperature, while T_2 is the outer wall or top surface temperature, and T is the dimensional temperature. The prime is dropped in the nondimensional governing equations (2.4 and 2.5).

2.3 Boundary conditions

2.3.1 Boundary conditions for thermocapillary convection

The inner and outer cylinder walls are rigid and maintained at fixed temperatures, so the boundary conditions on the two walls are simple.

$$u = v = w = 0, \quad T = T_1 \quad \text{on} \quad r = r_i \tag{2.13}$$

$$u = v = w = 0, \quad T = T_2 \quad \text{on} \quad r = r_o \tag{2.14}$$

The bottom surface is also rigid, but it is insulated, so the boundary conditions are:

$$u = v = w = 0, \quad \frac{\partial T}{\partial z} = 0 \quad \text{on} \quad z = 0 \tag{2.15}$$

The top free surface is assumed flat, so the vertical velocity vanishes on the upper boundary. Thus

$$w = 0 \quad \text{on} \quad z = 1 \tag{2.16}$$

The radial and azimuthal velocities on the free surface are governed by force balance between shear stresses and thermocapillary stresses. For flat surface approximation,

$$\mu\frac{\partial u}{\partial z} = -\frac{\partial \sigma}{\partial r} = -\gamma\frac{\partial T}{\partial r} \tag{2.17}$$

$$\mu\frac{\partial v}{\partial z} = -\frac{1}{r}\frac{\partial \sigma}{\partial \theta} = -\frac{\gamma}{r}\frac{\partial T}{\partial \theta} \tag{2.18}$$

where γ is the temperature coefficient of surface tension. It is defined in the equation,

$$\sigma = \sigma_{ref} + \gamma(T - T_{ref}) \tag{2.19}$$

The non-dimensionalization requires

$$\frac{\gamma(T_1 - T_2)}{U_R\mu} = 1 \tag{2.20}$$

from which the velocity scale

$$U_R = \frac{\gamma(T_1 - T_2)}{\mu} \tag{2.21}$$

is obtained. This is the reference velocity (2.10) that is used to non-dimensionalize the momentum and energy equations for thermocapillary problem. Thus the boundary condition on the free surface can be written as:

$$\frac{\partial u}{\partial z} = -\frac{\partial T}{\partial r}, \quad \frac{\partial v}{\partial z} = -\frac{1}{r}\frac{\partial T}{\partial \theta}, \quad w = 0, \quad \frac{\partial T}{\partial z} = 0 \tag{2.22}$$

In general for a true free surface, the height of the top surface is given,

$$z = 1 + h \tag{2.23}$$

where h is the surface deflection, which is a function of radius (r), azimuthal angle (θ), and time (t),

$$h = h(r, \theta, t) \tag{2.24}$$

The boundary conditions (2.22) are replaced by a series of more complex non-linear equations, governed by mass conservation of fluid (kinematic equation of the free surface), shear stress balance (dynamic condition), and energy balance. Those equations, along with normal stress balance (equation governing surface curvature) determine the deflection of the free surface. Details of those equations are given in Appendix A.

The periodic boundary conditions in θ direction is straightforward:

$$u_{\theta+2\pi} = u_\theta, \quad v_{\theta+2\pi} = v_\theta, \quad w_{\theta+2\pi} = w_\theta, \quad T_{\theta+2\pi} = T_\theta \tag{2.25}$$

2.3.2 Other boundary conditions

The dimensionless governing equations and the boundary conditions given above are derived for thermocapillary convection problem. The boundary conditions differ for other problems investigated in this dissertation.

Variable temperature on the inner surface

The inner cylinder temperature is constant for the case above ($T_1 = \text{const}$). It may be a function of θ. In this case, the T_1 can not be used to define the dimensionless temperature. The average value $\bar{T}_1$ can be used instead.

$$T' = \frac{T - T_2}{\bar{T}_1 - T_2} \tag{2.26}$$

The boundary condition is then changed to:

$$T_1' = \frac{T_1 - T_2}{\bar{T}_1 - T_2} \quad \text{on} \quad r = r_i \tag{2.27}$$

An example is that T_1' is a sinusoidal function of θ.

$$T_1' = \bar{T}_1'(1 + \epsilon \sin n\theta) \tag{2.28}$$

where ϵ is the amplitude of the dimensionless temperature variation of the inner wall or bottom surface T_1', and n is the wave number.

Natural convection in an enclosed cavity

The velocities on the free surface are driven by surface tension variation in thermo-capillary convection. For natural convection in an enclosed cavity, all the velocity components on the enclosing surfaces are fixed. Equation 2.22 is replaced by

$$u = v = w = 0, \quad \frac{\partial T}{\partial z} = 0 \quad \text{on} \quad z = 1 \tag{2.29}$$

The thermal boundary conditions remain the same for convection problems in which the temperatures of the inner and outer surfaces are fixed while the top and bottom surfaces are insulated.

For Rayleigh-Bénard convection problem in which the cavity is heated from the bottom, the inner and outer surfaces are insulated, the thermal boundary conditions become

$$T = T_1, \quad T = T_2 \quad \text{on} \;\; z = 0 \;\; \text{and} \;\; z = 1 \tag{2.30}$$

$$\frac{\partial T}{\partial z} = 0 \quad r = r_i \;\; \text{and} \;\; r = r_o \tag{2.31}$$

Flow in a lid driven cavity

For lid driven flow in radial direction, the boundary conditions on the top surface are:

$$u = u_{z1}, \quad v = w = 0, \quad \frac{\partial T}{\partial z} = 0 \quad \text{on} \;\; z = 1 \tag{2.32}$$

where u_{z1} is the radial velocity value or velocity profile on the top surface.

Flow with a rotating inner surface

The inner surface is assumed to be fixed for the cases discussed above. If the flow is caused by rotating the inner surface, the azimuthal velocity is no longer zero. The boundary condition on the inner walls (2.13) becomes,

$$u = w = 0, \quad v = v_0, \quad T = T_1 \quad \text{on} \;\; r = r_i \tag{2.33}$$

where v_0 is the azimuthal velocity of the inner surface.

2.4 Poisson equation of pressure

Divergence of the momentum equation results in a Poisson equation for pressure

$$\nabla^2 p = -\frac{\partial}{\partial t}(\nabla \cdot \mathbf{V}) - \nabla \cdot [(\mathbf{V} \cdot \nabla)\mathbf{V}] + \frac{1}{Re}\nabla^2(\nabla \cdot \mathbf{V}) + \frac{Gr}{Re^2}\frac{\partial T}{\partial z} \tag{2.34}$$

The convective term can be expressed explicitly as:

$$\begin{aligned}\nabla \cdot [(\mathbf{V} \cdot \nabla)\mathbf{V}] &= u\frac{\partial}{\partial r}(\nabla \cdot \mathbf{V}) + \frac{v}{r}\frac{\partial}{\partial \theta}(\nabla \cdot \mathbf{V}) + w\frac{\partial}{\partial z}(\nabla \cdot \mathbf{V}) \\ &+ \left(\frac{\partial u}{\partial r}\right)^2 + \frac{1}{r^2}\left(\frac{\partial v}{\partial \theta}\right)^2 + \left(\frac{\partial w}{\partial z}\right)^2 + \frac{2}{r}\frac{\partial u}{\partial \theta}\frac{\partial v}{\partial r} + 2\frac{\partial u}{\partial z}\frac{\partial w}{\partial r} + \frac{2}{r}\frac{\partial v}{\partial z}\frac{\partial w}{\partial \theta} \\ &+ \frac{u^2}{r^2} + 2\frac{u}{r^2}\frac{\partial v}{\partial \theta} - 2\frac{v}{r}\frac{\partial v}{\partial r}\end{aligned} \tag{2.35}$$

The terms containing $\nabla \cdot \mathbf{V}$ in (2.34) and (2.35) may be allowed to vanish by virtue of the continuity equation. How they are treated in the numerical solution will be discussed in the next chapter.

Boundary conditions for the Poisson equation are derived from the Navier-Stokes equations above. From (2.2 - 2.4), it follows that

$$\frac{\partial p}{\partial r} = \frac{1}{Re}\frac{\partial^2 u}{\partial r^2} + \frac{v^2}{r} \quad \text{on} \quad r = r_i \quad \text{and} \quad r = r_o \tag{2.36}$$

on the inner and outer surfaces. All other terms disappear owing to velocity boundary conditions and continuity equation. The term $\frac{v^2}{r}$ is zero in all cases except when flow is driven by the rotating inner cylinder. On the top and bottom surfaces

$$\frac{\partial p}{\partial z} = \frac{1}{Re}\left(\frac{\partial^2 w}{\partial z^2}\right) + \frac{Gr}{Re^2}T \quad \text{on} \quad z = 0 \quad \text{and} \quad z = 1 + h \tag{2.37}$$

and for pressure the periodicity condition

$$p(\theta + 2\pi) = p(\theta) \tag{2.38}$$

holds in θ-direction.

Equation (2.34) together with these boundary conditions (2.36 - 2.38) leads to a Neumann problem for the pressure. The resulting Poisson equation simplifies the problem greatly, since the pressure is decoupled from the velocity and temperature variables. However the right hand side of the equation must be known.

It is well known that a solution to this problem is unique only to an arbitrary constant and it is subject to an integral constraint given by

$$\int\int\int \nabla^2 p \, dV = \int\int \frac{\partial p}{\partial n} \, dS \tag{2.39}$$

The solution techniques are discussed in the following chapter.

CHAPTER 3

NUMERICAL METHOD

3.1 Overview of numerical methods

The mathematical equations described in the last chapter are non-linear second order partial differential equations. When the free surface is assumed flat ($h = 0$) in thermocapillary convection, and there are five unknowns (u, v, w, T, and p) and five independent equations: (2.1 - 2.5). Although the Poisson equation (2.34) is also used to solve for the variable p, it is derived from the five independent equations, and it is considered to be the replacement of the continuity equation (2.1).

The surface deflection adds one additional unknown, but it only affects the boundary on the free surface and the grids of the flow domain, with no impact on the governing equations. In this dissertation, the free surface is assumed to be flat at the leading order by imposing a small capillary number.

The Poisson equation is a linear equation for the pressure if the terms on the right hand side are assumed known. It has Neumann boundary conditions in r and z directions and periodic boundary condition in θ direction. It is solved by the fast direct

inversion method, a technique developed by Buzbee et al. [15] and extended to non-uniform grids in three-dimensional Cartesian coordinates by Babu [8] and Babu and Korpela [9]. This work further extends it to three-dimensional cylindrical coordinates.

The momentum and energy equations are parabolic, non-linear and coupled equations. These equations are solved by time marching. Crank-Nicholson implicit scheme is used in the discretization of the momentum and energy equations. The difference equations are then solved by Douglas-Gunn ADI method.

The pressure Poisson equation, the momentum equation, and the energy equation are discretized to second order accuracy in space using central differences.

3.1.1 Projection method

Projection methods, or fractional step methods, advance the momentum equation and enforce the continuity condition in separate steps. These methods use Hodge decomposition theorem, which states that any vector can be decomposed into the sum of a vector with zero divergence (solenoidal) and a vector of zero curl (irrotational).

The incompressible Navier-Stokes equations in vector form are,

$$\mathbf{v}_t + (\mathbf{v} \cdot \nabla)\mathbf{v} = -\nabla p + \frac{1}{Re}\nabla^2 \mathbf{v} + \mathbf{g} \tag{3.1}$$

$$\nabla \cdot \mathbf{v} = 0 \tag{3.2}$$

with boundary conditions

$$\mathbf{v}|_{\partial\Omega} = \mathbf{v}_b \tag{3.3}$$

The Hodge theorem states a vector $\mathbf{v}^*$ can be decomposed into a divergence-free part $\mathbf{v}$ and a gradient of a potential ϕ. That is,

$$\mathbf{v}^* = \mathbf{v} + \nabla\phi \tag{3.4}$$

with $\nabla \cdot \mathbf{v} = 0$.

The divergence-free part of the fictitious velocity vector $\mathbf{v}^*$ that does not satisfy continuity constraint can be obtained by a projection onto the orthogonal subspace of divergence-free vectors and their complement.

$$\mathbf{v} = \mathcal{P}(\mathbf{v}^*) \tag{3.5}$$

$$\nabla\phi = \mathcal{Q}(\mathbf{v}^*) \tag{3.6}$$

Symbolically the projection operator and its complement are:

$$\mathcal{P} = \mathbf{I} - \nabla[(\nabla^2)^{-1}\nabla\cdot] \tag{3.7}$$

$$\mathcal{Q} = \nabla[(\nabla^2)^{-1}\nabla\cdot] \tag{3.8}$$

The projection operator $\mathcal{P}$ and its complements $\mathcal{Q}$ are purely representations for the principle and numerical steps needed to solve the governing equations for the velocity and pressure variables. Using this principle, the projection method first approximates the momentum equation

$$\mathbf{v}_t^* + (\mathbf{v}^* \cdot \nabla)\mathbf{v}^* = -\nabla q + \frac{1}{Re}\nabla^2 \mathbf{v}^* + \mathbf{g} \tag{3.9}$$

and the boundary condition

$$B(\mathbf{v}^*) = 0 \tag{3.10}$$

with an intermediate velocity $\mathbf{v}^*$, which does not satisfy the continuity constraint in general. Here q is a pressure-like quantity - an approximation to the pressure.

After the intermediate velocity $\mathbf{v}^*$ is solved by advancing 3.9 in time t, the Hodge decomposition is applied to $\mathbf{v}^*$,

$$\mathbf{v}^* = \mathbf{v} + \nabla\phi \tag{3.11}$$

Taking divergence of 3.11 and substitution of 3.2 results in a Poisson equation for ϕ

$$\nabla^2\phi = \nabla \cdot \mathbf{v}^* \tag{3.12}$$

with the boundary condition,

$$\hat{\mathbf{n}} \cdot \nabla\phi|_{\partial\Omega} = 0 \tag{3.13}$$

The divergence-free velocity field $\mathbf{v}$ and the pressure can then be recovered with

$$\mathbf{v} = \mathbf{v}^* - \nabla\phi \tag{3.14}$$

$$p = q + f(\phi) \tag{3.15}$$

or its gradient form

$$\nabla p = \nabla q + f(\nabla \phi) \tag{3.16}$$

where f, which commutes with ∇, represents the dependence of p on ϕ. The way in which these calculations are carried out over each time step is discussed next.

Various projection methods differ in their approximation of pressure-like quantity q, function $f(\phi)$ in pressure update (3.15) or (3.16), the boundary condition $B(\mathbf{v}^*)$ (3.10), the advective terms $(\mathbf{v} \cdot \nabla)\mathbf{v}$, and how (3.9) is advanced (explicitly or implicitly). Bell et al. [10] advance (3.9) using Crank-Nicolson for time integration, approximate the advective terms with a Godunov procedure, and use the time-centered pressure gradient from previous time step to approximate ∇q,

$$\frac{\mathbf{v} - \mathbf{v}^n}{\Delta t} + ((\mathbf{v} \cdot \nabla)\mathbf{v})^{n+1/2} = -\nabla p^{n-1/2} + \frac{1}{2Re}(\nabla^2 \mathbf{v}^* + \nabla^2 \mathbf{v}^n) \tag{3.17}$$

with the body force being ignored here. The pressure gradient is updated with

$$\nabla p^{n+1/2} = \nabla p^{n-1/2} + \frac{1}{\Delta t}\nabla \phi \tag{3.18}$$

and the boundary condition for $\mathbf{v}^*$ to be the same as for $\mathbf{v}$

$$B(\mathbf{v}^*) = (\mathbf{v}^* - \mathbf{v})|_{\partial\Omega} = 0 \tag{3.19}$$

Therefore $\nabla q = \nabla p^{n-1/2}$ and $f(\nabla \phi) = 1/\Delta t \nabla \phi$ in this case.

Brown et al. [13] argue the above method is a second order in both time and space for velocity, but it is first order in time for pressure although second order in space.

Using the same q and boundary condition for $\mathbf{v}^*$, they improved the pressure update to enable the pressure accuracy to be second order in time with,

$$f(\nabla\phi) = \frac{1}{\Delta t}(\nabla\phi - \frac{1}{Re}\nabla^2\nabla\phi) \tag{3.20}$$

In Kim and Moin's pressure-free projection method [36] (see [13]), q is set to zero in (3.9), but the boundary condition for $\mathbf{v}^*$ is no longer identical to that for $\mathbf{v}^{n+1}$. But with an additional term at each time step,

$$\mathbf{v}^* = \mathbf{v} + \Delta t\nabla\phi \tag{3.21}$$

No pressure update is needed since the pressure does not appear in the solution method, but the authors in [36] give the relation $f(\phi) = \phi - (\nu\Delta t/2)\nabla^2\phi$.

3.1.2 Pressure Poisson equation method

Although the pressure - Poisson formulation used in this dissertation is somewhat different from the projection method described above, it follows the same principle. It first carries out a divergence on (3.1) to obtain the Poisson equation. By enforcing the divergence constraint ($\nabla \cdot \mathbf{v} = 0$) at the new time level, the pressure is then solved from the Poisson equation with the source term on the right hand side being evaluated at time t^n. The new pressure value is then used to advance the temperature and velocity fields to the new time level.

The major difference of the pressure Poisson equation method from projection methods is that there is no intermediate velocity involved. The pressure is solved directly from the pressure Poisson equation using the velocity from the previous time step,

and the new pressure value is available in solving for the velocity field at the new time step. In projection methods, the pressure is solved using an intermediate velocity, or the pressure can even totally be ignored [36]. The intermediate velocity is then used to solve for the "true" velocity which is divergence free.

The major drawback of the traditional pressure Poisson equation approach is that it is prohibitively expensive for complex three-dimensional applications, because iterative solution of the pressure Poisson equation is needed at each time step. For this reason, Chorin [17] resorted the artificial compressibility method. The direct inversion of the pressure Poisson equation in this dissertation eliminates the iterative aspect of the pressure solution, since the eigenvectors and eigenvalues can be used to calculate the pressure with Neumann boundary conditions and they depend on grids only. These computations are only needed once prior to advancing momentum equations. Matrix inversions involved with simple matrix multiplications are only needed at each time step. The direct inversion method also guarantees the solution accuracy to the discretization error or machine accuracy without subject to the number of the iterations or convergence criteria. Therefore it eliminates the possibility of the pressure fluctuations carried from the errors from the initial condition or previous steps (checkerboard pattern).

Divergence of the Navier-Stokes equation 3.1 results in pressure Poisson equation,

$$\nabla^2 p^{n+1} = -\frac{(\nabla \cdot \mathbf{v}^{n+1} - \nabla \cdot \mathbf{v}^n)}{\Delta t} - \nabla \cdot [(\mathbf{v} \cdot \nabla)\mathbf{v}]^n + \frac{1}{Re}\nabla^2(\nabla \cdot \mathbf{v})^n + \nabla \cdot \mathbf{g}^n \quad (3.22)$$

with

$$\nabla \cdot \mathbf{v}^{n+1} = 0 \tag{3.23}$$

The boundary conditions are Neumann type in r and z directions where the normal pressure gradients on the boundaries are computed from the momentum equations applied on the boundaries using known velocity field, and periodic in θ direction.

With pressure known, the velocities are solved from the momentum equations represented in (3.1).

In this dissertation, a direct inversion method is used to solve for pressure from the pressure Poisson equation in non-staggered grids, and Crank-Nicolson implicit scheme is used to discretize the momentum equations, that are solved for velocities using Douglas-Gunn ADI scheme. The details of the numerical techniques and discussions are presented next.

3.2 Grid generation

The pressure, temperature, and velocities are solved on regular, non-staggered girds generated in r, z, and θ directions.

Non-staggered grids store all the variables at the same set of grid points as shown in Fig. 3.1 (a). Non-staggered grids have significant advantages over staggered grids, especially when the boundaries have slope discontinuities or the boundary conditions are discontinuous [25]. They can also be used in non-orthogonal curvilinear coordinates and when using complex numerical techniques such as multi-grid method. The

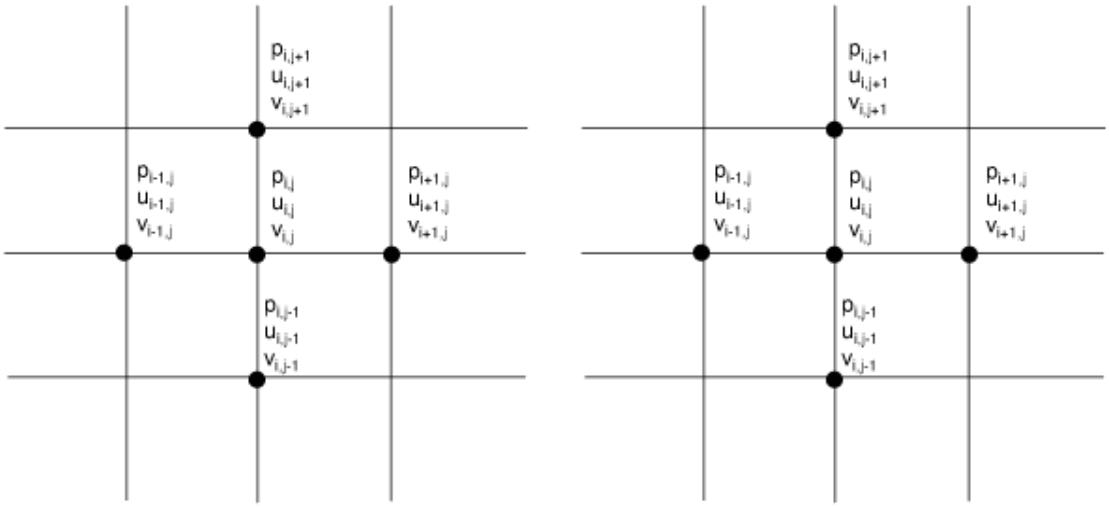

Figure 3.1: Grid representations. (a) Non-staggered grid, (b) staggered grid. Non-staggered grids are used in this dissertation.

compatibility condition is automatically satisfied on non-staggered grids, but that is not the case for staggered grids [62]. However, from the time the staggered grid was introduced in mid-1960s until the early 1980s, the non-staggered grid was hardly used, owing to difficulties caused by pressure-velocity decoupling and the occurrence of oscillations in the pressure. When improved pressure-velocity decoupling algorithms were developed in the 1980's, the popularity of the non-staggered arrangement began to rise [25].

Staggered grids were first used by Harlow and Welch [33], and they became popular ever since. In such grids, the scalar variables (pressure, density, and etc.) are located in the center of the neighboring grids, and the velocity components are placed in the middle of the corresponding sides, as shown in Fig. 3.1 (b) for two-dimensional

system. The staggered grids enable the pressure difference to be represented with second-order accuracy at the grid center using velocity components at adjacent grids instead of alternate grid points, and therefore the decoupling does not take place [6]. In fact, the strong coupling between pressure and velocities is the biggest advantage of staggered grids and it is the main reason for the popularity of the configuration. This helps to overcome convergence problems and oscillations in pressure and velocity fields [25]. However because the variables are not defined at the same grid point, accurately evaluating the nonlinear convective terms becomes difficult.

To overcome the pressure-velocity decoupling and to ensure mass conservation on non-staggered grids, the disretization on both sides of the Poisson equation needs to be consistent with the divergence and gradient operator, since the Laplacian operator is the product of divergence operator in the continuity equation and the gradient operator in the momentum equation. If forward differences are used for the divergence operator, the gradient operator should use backward differences, and vice versa. If central differences are used for one, they are required for the other [25]. In addition, the continuity equation needs to be forced at the new time step, and the divergence of velocity from the previous time step needs to be retained in the source term calculation unless the velocity field is totally divergence-free. With these treatments, numerical oscillation caused by pressure-velocity decoupling can be avoided with non-staggered grids. In addition, the direct inversion of pressure Poisson equation method without need of the iterations provides consistent and accurate solution without pressure oscillations.

To reduce the number of grid points necessary for convergence and accuracy, the problem can be solved on a non-uniform grid. The grid transformation used in this work is the same as that used by Babu [8]. The transformation carried out for both the $r-$ and $z-$directions is,

$$x_i = \alpha \tanh\left[\frac{1}{2}\log\left(\frac{\alpha+1}{\alpha-1}\xi\right)\right] \tag{3.24}$$

where ξ is the coordinate in the computational domain, corresponding to $x_i = r$, or z coordinate in the physical domain, and α is stretching parameter ($\alpha > 1$). All the equations and boundary conditions are transformed using one-dimensional transformations of the form $\xi = \xi(x_i)$ to a computational domain with uniform grids. Under the transformation, the derivatives of the coordinates become:

$$\frac{\partial}{\partial x_i} = \xi' \frac{\partial}{\partial \xi}, \qquad \frac{\partial^2}{\partial {x_i}^2} = \frac{\partial^2}{\partial \xi^2} + \xi'' \frac{\partial}{\partial \xi} \tag{3.25}$$

where ξ' and ξ'' are the first and second derivatives with respect to x_i.

$$\xi' = \frac{d\xi}{dx_i}, \qquad \xi'' = \frac{d^2\xi}{d{x_i}^2} \tag{3.26}$$

3.3 Fast direct inversion of pressure Poisson equation

It has been shown that the divergence-free velocity field and curl-free pressure field can be solved separately based on Hodge decomposition. The pressure at the new time step is first solved from the Poisson equation obtained from the divergence of (3.1) using the velocity and temperature fields from the previous time step while enforcing the divergence constraint at the new time step. The velocity and temperature fields at the new time step are then solved using the new pressure and temperature values.

3.3.1 Discretization

The Poisson equation (2.34) in the cylindrical coordinates can be written as

$$\nabla^2 p^{n+1} = c^n + \mathcal{O}(\Delta t) \tag{3.27}$$

where the left hand side is evaluated at time t^{n+1}, whereas the right hand side mainly involves terms at t^n only, with the exception of the divergence term which involves both the new and old time steps. The discretization error is first order in time and second order in space. Here

$$\nabla^2 = \frac{\partial^2}{\partial r^2} + \frac{1}{r}\frac{\partial}{\partial r} + \frac{1}{r^2}\frac{\partial^2}{\partial \theta^2} + \frac{\partial^2}{\partial z^2} \tag{3.28}$$

$$c^n = -\frac{1}{\Delta t}(D^{n+1} - D^n) - \nabla \cdot \left[(\mathbf{V}^n \cdot \nabla)\,\mathbf{V}^n\right] + \frac{1}{Re}\nabla^2 D^n + \frac{Gr}{Re^2}\frac{\partial T}{\partial z} \tag{3.29}$$

and D represents the divergence of the velocity,

$$D = \nabla \cdot \mathbf{V} = \frac{1}{r}\frac{\partial (ru)}{\partial r} + \frac{1}{r}\frac{\partial v}{\partial \theta} + \frac{\partial w}{\partial z} \tag{3.30}$$

The divergence constraint requires that the divergence of the velocity field at the new time step to be zero:

$$\nabla \cdot \mathbf{V}^{n+1} = 0 \tag{3.31}$$

This eliminates the t^{n+1} terms in right side of (3.27) and leaves t^n terms only. Equation (3.29) thus becomes

$$\nabla^2 p^{n+1} = \frac{D^n}{\Delta t} - \nabla \cdot \left[(\mathbf{V}^n \cdot \nabla)\,\mathbf{V}^n\right] + \frac{1}{Re}\nabla^2 D^n + \frac{Gr}{Re^2}\frac{\partial T}{\partial z} \tag{3.32}$$

Theoretically, D^n term should be zero by virtue of continuity equation. This is true for staggered grids, where the continuity constraint is enforced on each cell. For the method used in this dissertation, the D^n is not zero because of the discretization error. The term is retained here to prevent nonlinear instabilities in the solution of the momentum equations [33], [2], [25].

To enforce the integral constraint, integral of the right sides of the discretized Poisson equation is forced to zero by re-distributing the errors to each grid.

Boundary conditions

The boundary conditions (2.36 - 2.37) are used to solve for pressure values on the three solid walls ($r = r_i$, $r = r_o$, and $z = 0$) and one free surface ($z = 1 + h$). Second order one sided difference is used to discretize the right side of (2.36 - 2.37). On the inner surface $r = r_i$,

$$\left(\frac{\partial p}{\partial r}\right)_{k=0} = \frac{1}{Re}\left(\frac{\partial^2 u}{\partial r^2}\right)_{k=0} + \frac{{v^2}_{k=0}}{r_0} \tag{3.33}$$

where the diffusion term is evaluated by a central difference on the boundary

$$\left(\frac{\partial^2 u}{\partial r^2}\right)_{k=0} = ({\xi'}_0)^2 \frac{2u_{k=1}}{(\Delta\xi)^2} \tag{3.34}$$

where a fictitious velocity outside of the boundary $u_{k=-1} = u_{k=1}$ is used owing to

$$\frac{\partial u}{\partial r} = {\xi'}_0 \frac{u_{k=1} - u_{k=-1}}{\Delta t \xi} = 0 \tag{3.35}$$

The zero gradient above is determined by continuity equation on the boundary.

Alternatively, the second-order one-sided difference can be used to evaluate the derivative directly.

$$\left(\frac{\partial^2 u}{\partial r^2}\right)_{k=0} = (\xi'_0)^2 \frac{2u_{k=0} - 5u_{k=1} + 4u_{k=2} - u_{k=3}}{(\Delta\xi)^2} \tag{3.36}$$

The above equations (3.33 - 3.36) are examples of evaluating the boundary conditions. Other boundary conditions on the outer wall $r = r_o$, the bottom wall $z = 0$ and the free surface $z = 1 + h$ are evaluated similarly.

3.3.2 Matrix decomposition

The procedure to solve (3.32) follows that of Babu and Korpela [9] for three-dimensional Cartesian coordinates. In cylindrical coordinates, some complications appear. First, the coefficients of the derivatives of the pressure Poisson equation (in uniform grids) are no longer constant but functions of r instead. Second, the boundary conditions in the θ-coordinate are periodic. This leads to two extra elements in the matrix for each discretized r and z, in addition to the regular banded structure in the Cartesian coordinates. As a result, unlike the Cartesian coordinates, where there is no preference in the order in which the matrix decomposition is carried out, the preferred arrangement for the cylindrical coordinates is such that r is the outer most, θ is the inner most, and z is the intermediate coordinate. Otherwise, the algorithm developed previously for the Cartesian coordinates does not apply directly. (For two-dimensional $r - z$

coordinates, this is not critical, as only one level of diagonalization is needed.)

The Poisson equation for non-uniform grids is obtained by substituting (3.25) to (3.27). Dropping the superscripts, we write

$$\frac{1}{r^2}\frac{\partial^2 p}{\partial \theta^2} + (\xi')^2\frac{\partial^2 p}{\partial \xi^2} + (\xi'\frac{1}{r} + \xi'')\frac{\partial p}{\partial \xi} + (\eta')^2\frac{\partial^2 p}{\partial \eta^2} + \eta''\frac{\partial p}{\partial \eta} = c \tag{3.37}$$

The right hand side c is

$$\begin{aligned} c = & \frac{1}{\Delta t}\left(\xi'\frac{\partial u}{\partial \xi} + \frac{u}{r} + \frac{1}{r}\frac{\partial v}{\partial \theta} + \eta'\frac{\partial w}{\partial \eta}\right) + \eta'\frac{Gr}{Re^2}\frac{\partial T}{\partial \eta} \\ & - \left[\left(\xi'\frac{\partial u}{\partial \xi}\right)^2 + \frac{1}{r^2}\left(\frac{\partial v}{\partial \theta}\right)^2 + \left(\eta'\frac{\partial w}{\partial \eta}\right)^2 + \xi'\frac{2}{r}\frac{\partial u}{\partial \theta}\frac{\partial v}{\partial \xi}\right. \\ & \left. + 2\xi'\eta'\frac{\partial u}{\partial \eta}\frac{\partial w}{\partial \xi} + \eta'\frac{2}{r}\frac{\partial v}{\partial \eta}\frac{\partial w}{\partial \theta} + \frac{u^2}{r^2} + 2\frac{u}{r^2}\frac{\partial v}{\partial \theta} - \xi'\frac{2v}{r}\frac{\partial v}{\partial \xi}\right] \\ & - \left[u\frac{\partial}{\partial r} + \frac{v}{r}\frac{\partial}{\partial \theta} + w\frac{\partial}{\partial z}\right](\nabla \cdot D) + \frac{1}{Re}\nabla^2(\nabla \cdot D) \end{aligned} \tag{3.38}$$

where $\nabla \cdot D$ is the numerical representation of the divergence term. It needs to be discretized to the fourth order in order to get the second order accuracy for the Poisson equation.

The discretized form of the equation is:

$$\begin{aligned} & f_{i,j,k-1}p_{i,j,k-1} + e_{i,j-1,k}p_{i,j-1,k} + b_{i-1,j,k}p_{i-1,j,k} + d_{i,j,k}p_{i,j,k} \\ & + a_{i+1,j,k}p_{i+1,j,k} + g_{i,j+1,k}p_{i,j+1,k} + h_{i,j,k+1}p_{i,j,k+1} = c_{i,j,k} \end{aligned} \tag{3.39}$$

which holds for $1 \le i \le L$, $1 \le j \le M$, $1 \le k \le N$. The points on the r and z boundaries are eliminated using second order one sided differences for discretizing the

boundary conditions. For example, on the inner wall $r = r_i$, the discretized form is given as,

$$\xi_0' \frac{-p_{i,j,2} + 4p_{i,j,1} - 3p_{i,j,0}}{2\Delta\xi} = \left(\frac{\partial p}{\partial r}\right)_{k=0} \tag{3.40}$$

We thus obtain

$$p_{i,j,0} = \frac{4}{3}p_{i,j,1} - \frac{1}{3}p_{i,j,2} - \frac{2\Delta\xi}{3\xi_0'}\left(\frac{\partial p}{\partial r}\right)_{k=0} \tag{3.41}$$

Equation (3.39) becomes:

$$\begin{aligned} &e_{i,j-1,1}p_{i,j-1,1} + b_{i-1,j,1}p_{i-1,j,1} + \widetilde{d}_{i,j,1}p_{i,j,1} \\ &\quad + a_{i+1,j,1}p_{i+1,j,1} + g_{i,j+1,1}p_{i,j+1,1} + \widetilde{h}_{i,j,2}p_{i,j,2} = \widetilde{c}_{i,j,1} \end{aligned} \tag{3.42}$$

with

$$\widetilde{d}_{i,j,1} = d_{i,j,1} + \frac{4}{3}f_{i,j,0} \tag{3.43}$$

$$\widetilde{h}_{i,j,2} = h_{i,j,2} - \frac{1}{3}f_{i,j,0} \tag{3.44}$$

$$\widetilde{c}_{i,j,1} = c_{i,j,1} - \frac{2\Delta\xi}{3\xi'_0}\left(\frac{\partial p}{\partial r}\right)_{k=0} f_{i,j,0} \tag{3.45}$$

The $(\partial p/\partial r)_{k=0}$ term has been evaluated in (3.33), also using second order one sided difference.

The boundary conditions on the outer wall $r = r_o$, the bottom wall $z = 0$, and the free surface $z = 1 + h$ are treated similarly.

The periodic boundaries change the indices of the points on the θ boundaries. For $i = 1$, $p_{0,j,k} = p_{L,j,k}$, and $\alpha_{j,k} = b_{1,j,k}$. Equation (3.39) is then changed to:

$$\begin{aligned} f_{1,j,k-1}p_{1,j,k-1} + e_{1,j-1,k}p_{1,j-1,k} + d_{1,j,k}p_{1,j,k} + a_{2,j,k}p_{2,j,k} \\ + \alpha_{j,k}p_{L,j,k} + g_{1,j+1,k}p_{1,j+1,k} + h_{1,j,k+1}p_{1,j,k+1} = c_{1,j,k} \end{aligned} \tag{3.46}$$

Similarly, for $i = L$, $p_{L+1,j,k} = p_{1,j,k}$, and $\beta_{j,k} = a_{L+1,j,k}$. Equation (3.39) is changed to

$$\begin{aligned} \beta_{j,k}p_{1,j,k} + f_{L,j,k-1}p_{L,j,k-1} + e_{L,j-1,k}p_{L,j-1,k} + b_{L-1,j,k}p_{L-1,j,k} \\ + d_{L,j,k}p_{L,j,k} + g_{L,j+1,k}p_{L,j+1,k} + h_{L,j,k+1}p_{L,j,k+1} = c_{L,j,k} \end{aligned} \tag{3.47}$$

We can write the system of equations in a matrix form,

$$Q\ P = C \tag{3.48}$$

where Q is a block tridiagonal matrix.

$$Q = \begin{bmatrix} D_1 & H_2 & 0 & \cdots & 0 \\ F_1 & D_2 & H_3 & 0 & \cdots \\ \cdots & \cdots & \cdots & \cdots & \cdots \\ \cdots & 0 & F_{N-2} & D_{N-1} & H_N \\ 0 & \cdots & 0 & F_{N-1} & D_N \end{bmatrix}$$

This matrix is singular because of the natural boundary conditions in $r-$ and $z-$ directions, and periodic boundary condition in θ-direction. The unknown vector for the pressure can be written as

$$
\begin{aligned}
P &= [P_1, P_2, P_3, \cdots, P_k, \cdots, P_N]^T \\
P_k &= [P_{1,k}, P_{2,k}, \cdots, P_{j,k}, \cdots, P_{M,k}]^T \\
P_{j,k} &= [p_{1,j,k}, p_{2,j,k}, \cdots, p_{i,j,k}, \cdots, p_{L,j,k}]^T
\end{aligned}
\tag{3.49}
$$

and the right hand side is

$$
\begin{aligned}
C &= [C_1, C_2, C_3, \cdots, C_k, \cdots, C_N]^T \\
C_k &= [C_{1,k}, C_{2,k}, \cdots, C_{j,k}, \cdots, C_{M,k}]^T \\
C_{j,k} &= [c_{1,j,k}, c_{2,j,k}, \cdots, c_{i,j,k}, \cdots, c_{L,j,k}]^T
\end{aligned}
\tag{3.50}
$$

The diagonal blocks D_k are themselves block tridiagonal matrices,

$$
D_k = \begin{bmatrix}
D_{1,k} & G_{2,k} & 0 & \cdots & 0 \\
E_{1,k} & D_{2,k} & G_{3,k} & 0 & \cdots \\
\cdots & \cdots & \cdots & \cdots & \cdots \\
\cdots & 0 & E_{M-2,k} & D_{M-1,k} & G_{M,k} \\
0 & \cdots & 0 & E_{M-1,k} & D_{M,k}
\end{bmatrix}
$$

where

$$
D_{j,k} = \begin{bmatrix}
d_{1,j,k} & a_{2,j,k} & 0 & \cdots & 0 & \alpha_{j,k} \\
b_{1,j,k} & d_{2,j,k} & a_{3,j,k} & 0 & \cdots & 0 \\
\cdots & \cdots & \cdots & \cdots & \cdots & \cdots \\
0 & \cdots & 0 & b_{L-2,j,k} & d_{L-1,j,k} & a_{L,j,k} \\
\beta_{j,k} & 0 & \cdots & 0 & b_{L-1,j,k} & d_{L,j,k}
\end{bmatrix}
$$

$$
G_{j,k} = \begin{bmatrix}
g_{1,j,k} & 0 & \cdots & \cdots & \cdots \\
0 & g_{2,j,k} & 0 & \cdots & \cdots \\
\cdots & \cdots & \cdots & \cdots & \cdots \\
\cdots & \cdots & 0 & g_{L-1,j,k} & 0 \\
0 & \cdots & \cdots & 0 & g_{L,j,k}
\end{bmatrix}
$$

$$E_{j,k} = \begin{bmatrix} e_{1,j,k} & 0 & \cdots & \cdots & \cdots \\ 0 & e_{2,j,k} & 0 & \cdots & \cdots \\ \cdots & \cdots & \cdots & \cdots & \cdots \\ \cdots & \cdots & 0 & e_{L-1,j,k} & 0 \\ 0 & \cdots & \cdots & 0 & e_{L,j,k} \end{bmatrix}$$

The off-diagonal blocks H_k and F_k are block diagonal matrices,

$$H_k = \begin{bmatrix} H_{1,k} & 0 & \cdots & \cdots & 0 \\ 0 & H_{2,k} & 0 & \cdots & \cdots \\ \cdots & \cdots & \cdots & \cdots & \cdots \\ \cdots & \cdots & 0 & H_{M-1,k} & 0 \\ 0 & \cdots & \cdots & 0 & H_{M,k} \end{bmatrix}$$

$$F_k = \begin{bmatrix} F_{1,k} & 0 & \cdots & \cdots & 0 \\ 0 & F_{2,k} & 0 & \cdots & \cdots \\ \cdots & \cdots & \cdots & \cdots & \cdots \\ \cdots & \cdots & 0 & F_{M-1,k} & 0 \\ 0 & \cdots & \cdots & 0 & F_{M,k} \end{bmatrix}$$

where

$$H_{j,k} = \begin{bmatrix} h_{1,j,k} & 0 & \cdots & \cdots & 0 \\ 0 & h_{2,j,k} & 0 & \cdots & \cdots \\ \cdots & \cdots & \cdots & \cdots & \cdots \\ \cdots & \cdots & 0 & h_{L-1,j,k} & 0 \\ 0 & \cdots & \cdots & 0 & h_{L,j,k} \end{bmatrix}$$

$$F_{j,k} = \begin{bmatrix} f_{1,j,k} & 0 & \cdots & \cdots & 0 \\ 0 & f_{2,j,k} & 0 & \cdots & \cdots \\ \cdots & \cdots & \cdots & \cdots & \cdots \\ \cdots & \cdots & 0 & f_{L-1,j,k} & 0 \\ 0 & \cdots & \cdots & 0 & f_{L,j,k} \end{bmatrix}$$

Symmetrization

Examine matrix Q and its submatrices. Each block diagonal matrix $D_{j,k}$ is a symmetric matrix, since uniform grid is used in θ-direction.

$$b_{i,j,k} = a_{i+1,j,k} = \beta_{j,k} = \alpha_{j,k} = \frac{1}{{r_k}^2(\Delta\theta)^2} \tag{3.51}$$

For each j, the $g_{i,j,k} = \tilde{g}_j$ and $e_{i,j,k} = \tilde{e}_j$, where $\tilde{g}_j$ and $\tilde{e}_j$ are scalar function of j. Thus

$$G_{j,k} = \tilde{g}_j I_{[L \text{ by } L]}$$

$$E_{j,k} = \tilde{e}_j I_{[L \text{ by } L]}$$

For each k, $h_{i,j,k} = \tilde{h}_k$ and $f_{i,j,k} = \tilde{f}_k$, where $\tilde{h}_j$ and $\tilde{f}_j$ are scalar function of k. Thus

$$H_k = \tilde{h}_k I_{[LM \text{ by } LM]}$$

$$F_k = \tilde{f}_j I_{[LM \text{ by } LM]}$$

Since all the innermost tridiagonal matrices $D_{j,k}$ are already symmetric, the first level of symmetrization is to make $e_{i,j,k} = g_{i,j+1,k}$, so that the block tridiagonal matrices D_k are symmetric. It is done by multiplying both sides of (3.48) by a sequence of elementary matrix operations $R_{j,k}$, resulting in overall matrix operation R. Equation (3.48) is transformed to:

$$R\ Q\ P = R\ C \tag{3.52}$$

where

$$R = R_N\ R_{N-1} \cdots R_k \cdots R_1 \tag{3.53}$$

For each $k = 1, 2, \cdots, N$

$$R_k = R_{M-1,k}\ R_{M-2,k} \cdots R_{j,k} \cdots R_{1,k} \tag{3.54}$$

For each $j = 1, 2, \cdots, M-1$

$$R_{j,k} = R_{L,j,k}\ R_{L-1,j,k} \cdots R_{i,j,k} \cdots R_{1,j,k} \tag{3.55}$$

where

$$R_{i,j,k} = I_{[LMN \text{ by } LMN]} + \frac{g_{i,j+1,k}}{e_{i,j,k}} \Phi_{\mathcal{I},\mathcal{J}} \tag{3.56}$$

In (3.56), all the elements of the LMN by LMN matrix $\Phi_{\mathcal{I},\mathcal{J}}$ is identically zero except

$$\phi_{\mathcal{I},\mathcal{J}} = 1 \tag{3.57}$$

with

$$\begin{aligned} \mathcal{I} &= (k-1)LM + (j-1)L + i \\ \mathcal{J} &= \mathcal{I} + L = (k-1)LM + jL + i \end{aligned} \tag{3.58}$$

The operations do not affect the symmetry of the innermost tridiagonal matrix $D_{j,k}$, since $g_{i,j,k}$ and $e_{i,j,k}$ are constants for fixed j and k.

The second level of symmetrization is to make $f_{i,j,k} = h_{i,j,k+1}$, so that the full matrix is symmetric. It is done by multiplying both sides of (3.52) by a sequence of elementary matrix operations $S_{j,k}$ resulting in overall matrix S. Equation (3.52) is transformed to:

$$S(R\ Q\ P) = S(R\ C) \tag{3.59}$$

where

$$S = S_{N-1}\ S_{N-2} \cdots S_k \cdots S_1 \tag{3.60}$$

For each $k = 1, 2, \cdots, N-1$

$$S_k = S_{M,k} S_{M-1,k} \cdots S_{j,k} \cdots S_{1,k} \tag{3.61}$$

For each $j = 1, 2, \cdots, M$

$$S_{j,k} = S_{L,j,k} S_{L-1,j,k} \cdots S_{i,j,k} \cdots S_{1,j,k} \tag{3.62}$$

where

$$S_{i,j,k} = I_{[LMN \text{ by } LMN]} + \frac{h_{i,j,k+1}}{f_{i,j,k}} \Phi_{\mathcal{I},\mathcal{J}} \tag{3.63}$$

In (3.63), all the elements of the LMN by LMN matrix $\Phi_{\mathcal{I},\mathcal{J}}$ are identically zero except

$$\phi_{\mathcal{I},\mathcal{J}} = 1 \tag{3.64}$$

with

$$\begin{aligned} \mathcal{I} &= (k-1)LM + (j-1)L + i \\ \mathcal{J} &= \mathcal{I} + LM = kLM + (j-1)L + i \end{aligned} \tag{3.65}$$

The operations do not affect the symmetry of the block tridiagonal matrix D_k, since $h_{i,j,k}$ and $f_{i,j,k}$ are constants for a fixed k.

The resulting matrix $(S\ R\ Q)$, denoted by Q', is then symmetric. The right hand side $(S\ R\ C)$ is correspondingly denoted by C'. Dropping the primes, the equation is now:

$$Q\ P = C \tag{3.66}$$

As Q is symmetric, all the sub-matrices also become symmetric. Q can be expressed as

$$Q = \begin{bmatrix} D_1 & H_1 & 0 & \cdots & 0 \\ H_1 & D_2 & H_2 & 0 & \cdots \\ \cdots & \cdots & \cdots & \cdots & \cdots \\ \cdots & 0 & H_{N-2} & D_{N-1} & H_{N-1} \\ 0 & \cdots & 0 & H_{N-1} & D_N \end{bmatrix}$$

This matrix is singular because of the natural boundary conditions in $r-$ and $z-$ directions, and periodic boundary condition in θ direction. The unknown vector for the pressure can be written as

$$
\begin{aligned}
P &= [P_1, P_2, P_3, \cdots, P_k, \cdots, P_N]^T \\
P_k &= [P_{1,k}, P_{2,k}, \cdots, P_{j,k}, \cdots, P_{M,k}]^T \\
P_{j,k} &= [p_{1,j,k}, p_{2,j,k}, \cdots, p_{i,j,k}, \cdots, p_{L,j,k}]^T
\end{aligned}
\tag{3.67}
$$

and the right hand side is

$$
\begin{aligned}
C &= [C_1, C_2, C_3, \cdots, C_k, \cdots, C_N]^T \\
C_k &= [C_{1,k}, C_{2,k}, \cdots, C_{j,k}, \cdots, C_{M,k}]^T \\
C_{j,k} &= [c_{1,j,k}, c_{2,j,k}, \cdots, c_{i,j,k}, \cdots, c_{L,j,k}]^T
\end{aligned}
\tag{3.68}
$$

The diagonal blocks D_k are themselves block tridiagonal matrices,

$$
D_k = \begin{bmatrix}
D_{1,k} & G_{1,k} & 0 & \cdots & 0 \\
G_{1,k} & D_{2,k} & G_{2,k} & 0 & \cdots \\
\cdots & \cdots & \cdots & \cdots & \cdots \\
\cdots & 0 & G_{M-2,k} & D_{M-1,k} & G_{M-1,k} \\
0 & \cdots & 0 & G_{M-1,k} & D_{M,k}
\end{bmatrix}
$$

where

$$
D_{j,k} = \begin{bmatrix}
d_{1,j,k} & a_{1,j,k} & 0 & \cdots & 0 & \alpha_{j,k} \\
a_{1,j,k} & d_{2,j,k} & a_{2,j,k} & 0 & \cdots & 0 \\
\cdots & \cdots & \cdots & \cdots & \cdots & \\
0 & \cdots & a_{L-2,j,k} & d_{L-1,j,k} & a_{L-1,j,k} & \\
\alpha_{j,k} & 0 & \cdots & 0 & a_{L-1,j,k} & d_{L,j,k}
\end{bmatrix}
$$

$$
G_{j,k} = \begin{bmatrix}
g_{1,j,k} & 0 & \cdots & \cdots & \cdots \\
0 & g_{2,j,k} & 0 & \cdots & \cdots \\
\cdots & \cdots & \cdots & \cdots & \cdots \\
\cdots & \cdots & 0 & g_{L-1,j,k} & 0 \\
0 & \cdots & \cdots & 0 & g_{L,j,k}
\end{bmatrix}
$$

The off-diagonal blocks H_k are (block) diagonal matrices,

$$H_k = \begin{bmatrix} H_{1,k} & 0 & \cdots & \cdots & 0 \\ 0 & H_{2,k} & 0 & \cdots & \cdots \\ \cdots & \cdots & \cdots & \cdots & \cdots \\ \cdots & \cdots & 0 & H_{M-1,k} & 0 \\ 0 & \cdots & \cdots & 0 & H_{M,k} \end{bmatrix}$$

where

$$H_{j,k} = \begin{bmatrix} h_{1,j,k} & 0 & \cdots & \cdots & 0 \\ 0 & h_{2,j,k} & 0 & \cdots & \cdots \\ \cdots & \cdots & \cdots & \cdots & \cdots \\ \cdots & \cdots & 0 & h_{L-1,j,k} & 0 \\ 0 & \cdots & \cdots & 0 & h_{L,j,k} \end{bmatrix}$$

In these equations, $d_{i,j,k}$, $a_{i,j,k}$, $g_{i,j,k}$, $h_{i,j,k}$ are the coefficients of $p_{i,j,k}$, $p_{i+1,j,k}$, $p_{i,j+1,k}$, and $p_{i,j,k+1}$ in the i-th equation for a fixed j and k. The coefficients of $p_{i-1,j,k}$, $p_{i,j-1,k}$ and $p_{i,j,k-1}$ for the equation are $a_{i-1,j,k}$, $g_{i,j-1,k}$ and $h_{i,j,k-1}$. The elements $\alpha_{j,k}$ on the corners of the matrix $D_{j,k}$ are the coefficients of $p_{L,j,k}$ in the first equation and $p_{1,j,k}$ in the last equation for the same j and k. Because of the periodic boundary conditions on θ, the usual banded structure for three-dimensional Cartesian coordinates is destroyed. However, the extra elements from the periodic boundary conditions are limited to the innermost block matrices if the discretization on θ-direction is done on the innermost level.

First level decomposition

It can be proved that all the sub-matrices $D_{j,k}$ of Q have the same generalized eigenvectors. Using the central matrix ($j = M/2+1, k = N/2+1$) as the reference matrix, this means that

$$D_{M/2+1,N/2+1}\mathbf{e} = \lambda H_{M/2+1,N/2+1}\mathbf{e} \tag{3.69}$$

Let E be the matrix of eigenvectors and Λ be the diagonal matrix of eigenvalues of the above generalized eigenvalue problem. The simultaneous diagonalization gives:

$$E^T D_{M/2+1,N/2+1} e = \Lambda \qquad E^T G_{M/2+1,N/2+1} E = I \tag{3.70}$$

Sub-matrices for other values of j and k are found to be related by:

$$D_{j,k} = \mu_{j,k} D_{M/2+1,N/2+1} + \nu_{j,k} G_{M/2+1,N/2+1} \tag{3.71}$$

$$G_{j,k} = \gamma_{j,k} G_{M/2+1,N/2+1} \tag{3.72}$$

and

$$H_{j,k} = \omega_{j,k} G_{M/2+1,N/2+1} \tag{3.73}$$

This leads to the first level diagonalization, resulting in the separation of $\theta-$direction and yielding a two-dimensional problem involving the $z-$ and $r-$ coordinates for each θ grid plane. Equation (3.66) can now be written, for each i $(1 \leq i \leq L)$, as

$$\begin{aligned} \bar{D}_{i,1}\bar{P}_{i,1} + \bar{H}_{i,1}\bar{P}_{i,2} &= \bar{\mathbf{C}}_{i,1} \\ \bar{H}_{i,k-1}\bar{P}_{i,k-1} + \bar{D}_{i,k}\bar{P}_{i,k} + \bar{H}_{i,k}\bar{P}_{i,k+1} &= \bar{C}_{i,k}, \quad 2 \leq k \leq N-1 \\ \bar{H}_{i,N-1}\bar{P}_{i,N-1} + \bar{D}_{i,N}\bar{P}_{i,N} &= \bar{C}_{i,N} \end{aligned} \tag{3.74}$$

where $\bar{P}_{i,k}$ and $\bar{C}_{i,k}$ are obtained from the re-ordering. They are given by

$$\bar{P}_{j,k} = \begin{bmatrix} \bar{p}_{1,j,k} \\ \bar{p}_{2,j,k} \\ \vdots \\ \bar{p}_{L,j,k} \end{bmatrix} = E^{-1} P_{j,k} = E^{-1} \begin{bmatrix} p_{1,j,k} \\ p_{2,j,k} \\ \vdots \\ p_{L,j,k} \end{bmatrix}$$

(3.75)

$$\bar{C}_{j,k} = \begin{bmatrix} \bar{c}_{1,j,k} \\ \bar{c}_{2,j,k} \\ \vdots \\ \bar{c}_{L,j,k} \end{bmatrix} = E^T \mathbf{C}_{j,k} = E^T \begin{bmatrix} c_{1,j,k} \\ c_{2,j,k} \\ \vdots \\ c_{L,j,k} \end{bmatrix}$$

(3.76)

and

$$\bar{D}_{i,k} = \begin{bmatrix} \tilde{\lambda}_{i,1,k} & \gamma_{i,1,k} & 0 & \cdots & 0 \\ \gamma_{i,1,k} & \tilde{\lambda}_{i,2,k} & \gamma_{i,2,k} & 0 & \cdots \\ \cdots & \cdots\cdots & \cdots & \cdots & \cdots \\ \cdots & 0 & \gamma_{i,M-2,k} & \tilde{\lambda}_{i,M-1,k} & \gamma_{i,M-1,k} \\ 0 & \cdots & 0 & \gamma_{i,M-1,k} & \tilde{\lambda}_{i,M,k} \end{bmatrix}$$

(3.77)

where

$$\tilde{\lambda}_{i,j,k} = \mu_{j,k}\lambda_{i,j,k} + \nu_{j,k}\gamma_{i,j,k} \tag{3.78}$$

The matrix $\bar{H}$ is given by

$$\bar{H}_{i,k} = \begin{bmatrix} \omega_{i,1,k} & 0 & \cdots & \cdots & 0 \\ 0 & \omega_{i,2,k} & 0 & \cdots & \cdots \\ \cdots & \cdots & \cdots & \cdots & \cdots \\ \cdots & \cdots & 0 & \omega_{i,M-1,k} & 0 \\ 0 & \cdot & \cdots & 0 & \omega_{i,M,k} \end{bmatrix}$$

(3.79)

Second level decomposition

For the arrangement of the coordinates as $\theta - z - r$, the sub-matrices $\bar{D}_{i,k}$ again follow the relationship

$$\bar{D}_{i,k} = \bar{\mu}_{i,k}\bar{D}_{L/2+1,N/2+1} + \bar{\nu}_{i,k}\bar{H}_{L/2+1,N/2+1} \tag{3.80}$$

and

$$\bar{H}_{i,k} = \bar{\omega}_{i,k}\bar{H}_{L/2+1,N/2+1} \tag{3.81}$$

Solution of the generalized eigenvalue problem

$$\bar{D}_{L/2+1,N/2+1}\mathbf{f} = \bar{\lambda}\bar{H}_{L/2+1,N/2+1}\mathbf{r} \tag{3.82}$$

results in the second level simultaneous diagonalization:

$$F^T\bar{D}_{L/2+1,N/2+1}F = \bar{\Lambda}_{i,k}, \qquad F^T\bar{H}_{L/2+1,N/2+1}F = I \tag{3.83}$$

Here, F is the matrix of eigenvectors and $\bar{\Lambda}$ is the diagonal matrix of eigenvalues of the general eigenvalue problem (3.82).

This diagonalization results in the separation of the z-coordinate and yields a one-dimensional problem involving the r-coordinate on each grid line parallel to the r-axis. These sub-matrices again have the same eigen-base.

Equation (3.74) can now be written, for each i,j $(1 \leq i \leq L, 1 \leq j \leq M)$, as

$$
\begin{aligned}
(\bar{\mu}_{i,j,1}\bar{\lambda}_j + \bar{\nu}_{i,j,1})\bar{\bar{p}}_{i,j,1} + \bar{\omega}_{i,j,1}\bar{\bar{p}}_{i,j,2} &= \bar{\bar{c}}_{i,j,1} \\
\bar{\omega}_{i,j,k-1}\bar{\bar{p}}_{i,j,k-1} + (\bar{\mu}_{i,j,k}\bar{\lambda}_j + \bar{\nu}_{i,j,k})\bar{\bar{p}}_{i,j,k} + \bar{\omega}_{i,j,k}\bar{\bar{p}}_{i,j,k+1} &= \bar{\bar{c}}_{i,j,k} \\
2 \le k \le N-1 & \\
\bar{\omega}_{i,j,N-1}\bar{\bar{p}}_{i,j,N-1} + (\bar{\mu}_{i,j,N}\bar{\lambda}_j + \bar{\nu}_{i,j,N})\bar{\bar{p}}_{i,j,N} &= \bar{\bar{c}}_{i,j,N}
\end{aligned}
\tag{3.84}
$$

where

$$
\bar{\bar{P}}_{i,k} = \begin{bmatrix} \bar{\bar{p}}_{i,1,k} \\ \bar{\bar{p}}_{i,2,k} \\ \vdots \\ \bar{\bar{p}}_{i,M,k} \end{bmatrix} = F^{-1}\bar{P}_{i,k} = F^{-1} \begin{bmatrix} \bar{p}_{i,1,k} \\ \bar{p}_{i,2,k} \\ \vdots \\ \bar{p}_{i,M,k} \end{bmatrix}
\tag{3.85}
$$

and

$$
\bar{\bar{C}}_{i,k} = \begin{bmatrix} \bar{\bar{c}}_{i,1,k} \\ \bar{\bar{c}}_{i,2,k} \\ \vdots \\ \bar{\bar{c}}_{i,M,k} \end{bmatrix} = F^{T}\bar{C}_{i,k} = F^{T} \begin{bmatrix} \bar{c}_{i,1,k} \\ \bar{c}_{i,2,k} \\ \vdots \\ \bar{c}_{i,M,k} \end{bmatrix}
\tag{3.86}
$$

The matrices of the equations are now all scalar tridiagonal matrices, and can be solved by the Thomas algorithm [6].

Matrix inversion

The pressure $p_{i,j,k}$ can be solved by two matrix inversions. From (3.85), we obtain

$$
\bar{P}_{i,k} = F\bar{\bar{P}}_{i,k}
\tag{3.87}
$$

for each i and k, and from (3.75), we obtain finally

$$P_{j,k} = E\bar{P}_{j,k} \tag{3.88}$$

for each j, k.

At this point, the pressure values are available for next iteration (time step t^{n+1}) to solve for the remaining variables u, v, w, and T.

3.4 Finite difference method to solve for velocities and temperature

After the pressure is solved the momentum and energy equations are simplified, for only four variables (u, v, w and T) are unknown. We employ Crank-Nicholson implicit scheme to discretize the equations for the reason of numerical stability. Alternate Direction Implicit (ADI) method is then used to solve the difference equations.

3.4.1 Crank-Nicholson scheme

The non-linear Navier-Stokes equations and the energy equation can be written in the general form:

$$\frac{\partial\phi}{\partial t} + u\frac{\partial\phi}{\partial r} + \frac{v}{r}\frac{\partial\phi}{\partial\theta} + w\frac{\partial\phi}{\partial z} = Y + \epsilon_i\left(\frac{\partial^2\phi}{\partial r^2} + \frac{1}{r}\frac{\partial\phi}{\partial r} + \frac{1}{r^2}\frac{\partial^2\phi}{\partial\theta^2} + \frac{\partial^2\phi}{\partial z^2}\right) \tag{3.89}$$

where ϕ is a vector of dependent variables

$$\phi = \begin{bmatrix} u \\ v \\ w \\ T \end{bmatrix}$$

and ϵ_i is i-th element of vector ϵ, corresponding the i-th variable

$$\epsilon = \left(\frac{1}{Re}, \quad \frac{1}{Re}, \quad \frac{1}{Re}, \quad \frac{1}{Re\ Pr}\right) \tag{3.90}$$

Y is a function of ϕ and p, and is given by

$$Y = \begin{bmatrix} \frac{v^2}{r} - \frac{1}{Re}(\frac{u}{r^2} + \frac{2}{r^2}\frac{\partial v}{\partial \theta}) \\ -\frac{uv}{r} - \frac{1}{Re}(\frac{v}{r^2} - \frac{2}{r^2}\frac{\partial u}{\partial \theta}) \\ \frac{Gr}{Re^2}T \\ 0 \end{bmatrix} + \begin{bmatrix} -\frac{\partial p}{\partial r} \\ -\frac{1}{r}\frac{\partial p}{\partial \theta} \\ -\frac{\partial p}{\partial z} \\ 0 \end{bmatrix} \tag{3.91}$$

We can rewrite this equation as

$$\frac{\partial \phi}{\partial t} + \mathcal{D}_i \phi = Y \tag{3.92}$$

where

$$\mathcal{D}_i = u\frac{\partial}{\partial r} + \frac{v}{r}\frac{\partial}{\partial \theta} + \frac{\partial}{\partial z} - \epsilon_i(\frac{\partial^2}{\partial r^2} + \frac{1}{r}\frac{\partial}{\partial r} + \frac{1}{r^2}\frac{\partial^2}{\partial \theta^2} + \frac{\partial^2}{\partial z^2}) \tag{3.93}$$

Using Crank-Nicholson scheme [47], the equation is discretized to the following form

$$\frac{\phi^{n+1} - \phi^n}{\Delta t} + \frac{1}{2}\mathcal{D}_i(\phi^{n+1} + \phi^n) = Y \tag{3.94}$$

The term Y in the above equation is known, evaluated at time t^n. Eq. (3.94) is rewritten as,

$$(1 + \frac{\Delta t}{2}\mathcal{D}_i)\phi^{n+1} = (1 - \frac{\Delta t}{2}\mathcal{D}_i)\phi^n + \Delta t\ Y \tag{3.95}$$

Certain terms containing the velocity variables in Y such as $\frac{1}{Re}\frac{u}{r^2}$ and $\frac{1}{Re}\frac{v}{r^2}$ can be put in the implicit form to increase the diagonal dominance of the matrix thus improve the convergence as Ferziger recommends [25]. Only the v in the $\frac{uv}{r}$ term should be in the implicit form, while the u is evaluated explicitly.

3.4.2 ADI scheme

Solution of (3.95) is accomplished by application of an alternating-direction implicit (ADI) technique. Following Briley and McDonald [12], we write $\mathcal{D}_i$ in the following form,

$$\mathcal{D}_i = \mathcal{D}_i^r + \mathcal{D}_i^\theta + \mathcal{D}_i^z \tag{3.96}$$

where

$$\mathcal{D}_i^r = u^n \frac{\partial}{\partial r} - \epsilon_i \left(\frac{\partial^2}{\partial r^2} + \frac{1}{r}\frac{\partial}{\partial r}\right) \tag{3.97}$$

$$\mathcal{D}_i^\theta = \frac{v^n}{r}\frac{\partial}{\partial \theta} - \epsilon_i \frac{1}{r^2}\frac{\partial^2}{\partial \theta^2} \tag{3.98}$$

$$\mathcal{D}_i^z = w^n \frac{\partial}{\partial z} - \epsilon_i \frac{\partial^2}{\partial z^2} \tag{3.99}$$

where the coefficients u, v, and w of the non-linear terms on the left hand side of (3.95) were lagged one time level for the purpose of linearization of the equation. It has no significant effect on the accuracy for the first order time discretization. Equation (3.95) is expressed as:

$$\left[1+\frac{\Delta t}{2}(\mathcal{D}_i^r+\mathcal{D}_i^\theta+\mathcal{D}_i^z)\right]\phi^{n+1}=(1-\frac{\Delta t}{2}\mathcal{D}_i)\phi^n+\Delta t\ Y \tag{3.100}$$

The left hand side can be factorized as,

$$\begin{aligned}1+\frac{\Delta t}{2}(\mathcal{D}_i^r+\mathcal{D}_i^\theta+\mathcal{D}_i^z)&=(1+\frac{\Delta t}{2}\mathcal{D}_i^r)(1+\frac{\Delta t}{2}\mathcal{D}_i^\theta)(1+\frac{\Delta t}{2}\mathcal{D}_i^z)\\&-\frac{(\Delta t^2)}{4}(\mathcal{D}_i^r\mathcal{D}_i^\theta+\mathcal{D}_i^r\mathcal{D}_i^z+\mathcal{D}_i^\theta\mathcal{D}_i^z)+\frac{(\Delta t)^3}{8}\mathcal{D}_i^r\mathcal{D}_i^\theta\mathcal{D}_i^z\end{aligned} \tag{3.101}$$

Omitting the (Δt^2) and higher order terms, (3.100) is approximated as

$$(1+\frac{\Delta t}{2}\mathcal{D}_i^r)(1+\frac{\Delta t}{2}\mathcal{D}_i^z)(1+\frac{\Delta t}{2}\mathcal{D}_i^\theta)\phi^{n+1}=(1-\frac{\Delta t}{2}\mathcal{D}_i)\phi^n+\Delta t\ Y \tag{3.102}$$

Although the approximation is second order in time, the overall scheme on time is still first order, since the terms in Y and velocity terms in (3.97 - 3.99) are evaluated at t^n. The Douglas-Gunn representation of (3.102) can be written as following three-step solution procedure,

$$\begin{aligned}(1+\frac{\Delta t}{2}\mathcal{D}_i^r)\phi^{n+1/3}&=(1-\frac{\Delta t}{2}\mathcal{D}_i)\phi^n+\Delta t\ Y\\(1+\frac{\Delta t}{2}\mathcal{D}_i^z)\phi^{n+2/3}&=\phi^{n+1/3}\\(1+\frac{\Delta t}{2}\mathcal{D}_i^\theta)\phi^{n+1}&=\phi^{n+2/3}\end{aligned} \tag{3.103}$$

where $\phi^{n+1/3}$ and $\phi^{n+2/3}$ are intermediate solutions. Each equation in the set (3.103) is a one-dimensional problem. For $r-$ and $z-$ directions, the boundary conditions are Dirichlet or Neumann type, and the matrices of the equations are tridiagonal. Thus Thomas algorithm can be employed. For the θ-direction, the boundary conditions are periodic, two additional elements appear on the right-top and left-bottom corners.

Thus LU decomposition method can be used to solve this equation. By this three level solution, all the variables u, v, w, and T are obtained.

3.5 Summary of the algorithm

One advantage of the algorithm is that the pressure solution is obtained by simple multiplications of the eigenvalues and eigenvectors, which were solved only once, and the source term, which can be calculated for each time step. The temperature field and velocity field have to be solved for each time step. As a result, from the computational effort point of view, for each time step only four equations - three momentum equations and one energy equation are required to solve for the four variables - three velocity components and one temperature. The pressure is updated from the direct inversion by solving the pressure Poisson equation using updated velocities and temperature and the eigenvalues and eigenvectors solved prior to time marching. The advantage is clear when compared to the vorticity - vector potential method and velocity - vector potential method, in which six variables and six equations are required.

The algorithm can be summarized to the following steps.

1) Generate grids: option of uniform or non-uniform grids on either side or both sides of the r and z coordinates.

2) Solve for the generalized eigenvalues and eigenvectors for the pressure Poisson equation. Modify the zero eigenvalue to be unity (non-zero value). This makes the

non-unique pressure solution unique.

3) Apply initial conditions on the velocities and temperatures to all the grids. For a new problem, the velocities are all set to zero, and temperature is assumed to vary linearly across the cavity. For continuing iterations from the earlier solution, the velocities and temperature are read from the data files saved from the last time step.

4) Apply proper velocity and temperature boundary conditions.

5) Start time marching solution.

6) After calculating the source term of the pressure Poisson equation, solve for pressure field using the eigenvalues and eigenvectors solved in Step 2. The divergence constraint at the new time step is enforced here.

7) Solve for temperature field using the velocity from the previous time step.

8) Solve for velocity field using ADI method with updated temperature and pressure.

9) Repeat steps 6) to 8) until the specified time steps are reached or until desired convergence.

CHAPTER 4

CODE VALIDATION

4.1 Introduction

In this study, the governing equations, including Navier-Stokes equations, energy equation, and the Poisson equation, have been coded based on the method presented in the previous chapter. The code for solving the pressure Poisson equation is tested with known analytical solution, and the code for solving the governing equations is tested and compared with known analytical solutions (flow in an tall annulus with a rotating cylinder and natural convection in a tall annulus with heated inner cylinder) and established numerical solutions (flow in a lid-driven cavity). In the later chapters, the code will be used to study different flow problems, including thermocapillary convection in an annulus, natural convection in a shallow cavity heated from below (Rayleigh-Bénard convection), and flow in an annulus with rotating inner cylinder (Taylor-Couette flow).

4.2 Solutions of Poisson equations

The algorithm for fast direct inversion has been coded and tested in three-dimensional cylindrical coordinates. An known analytical solution was used to verify the program.

In the test case, the analytical solution and the partial differential equation with the simple force term are

$$p = r^2 \sin(2\theta) + (z - 0.5)^2 \qquad \nabla^2 p = 2$$

The code was run with a $32(r) \times 32(z) \times 36(\theta)$ uniform grid with the known force term and the boundary conditions, and the pressure solution is obtained with single step without iteration needed. In Figure 4.1 the pressure is plotted along θ coordinate on $z = 0$, 0.5, and 1, and in Figure 4.2 the pressure is plotted along z coordinate on $r = 0.1$, 0.55, and 1 in the middle height plane ($z = 0.5$). In Figure 4.3 the pressure is plotted along r coordinate on $\theta = 0$, $\pi/6$, and $\pi/3$ and in the middle of the radius gap ($r = 0.55$). The analytical solutions are also plotted for comparison. The numerical solution is the same as the analytical solution, subject to disrectization error.

4.3 Couette flow in a tall annulus with a rotating inner cylinder

The computer code was tested with a flow in a tall annulus ($r_i = 0.84$, $r_o = 1.0$, $H = 1$) with a rotating inner cylinder with $Re = 64$ based on the gap L. The reference velocity defining the Reynolds number is the azimuthal velocity of the inner surface $V = 1$. The computations were done on a $32(r) \times 128(z) \times 72(\theta)$ uniform grid. The flow is subject to instability but when the inner cylinder velocity is below a certain level at which the instability starts to occur, the flow is called circular Couette flow. For a tall annulus away from the two ends, the resultant flow is two-dimensional axisymmetric with azimuthal and radial velocities only. The azimuthal velocity has a simple analytical form:

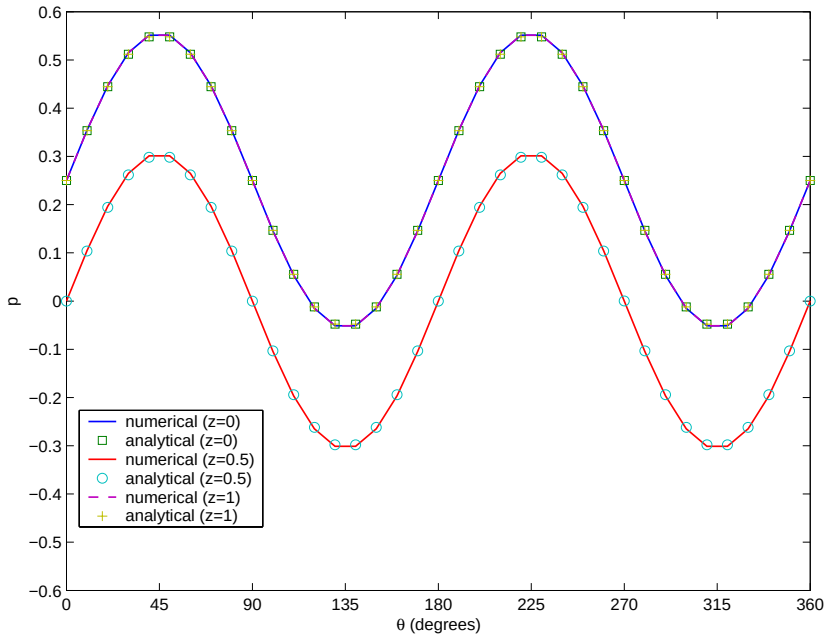

Figure 4.1: Numerical solution of pressure Poisson equation in comparison to the analytical solution on $z = 0$, 0.5 and 1.

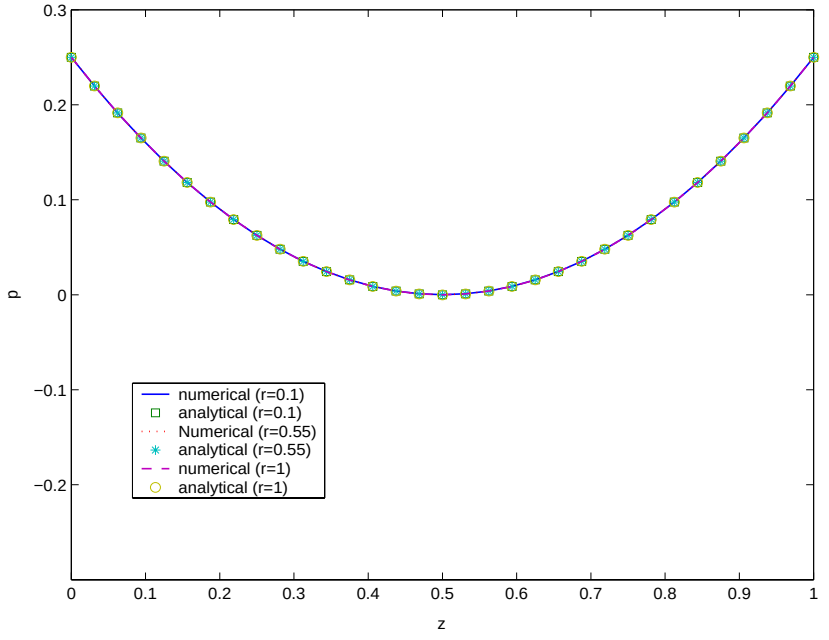

Figure 4.2: Numerical solution of pressure Poisson equation in comparison to the analytical solution on $r = 0.1$, 0.55 and 1 and $z = 0.5$.

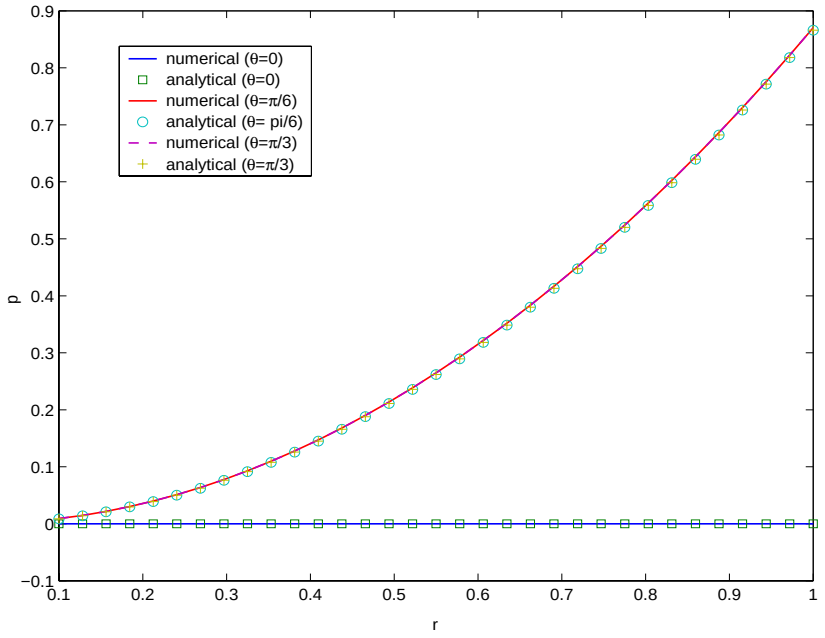

Figure 4.3: Numerical solution of pressure Poisson equation in comparison to the analytical solution on $\theta = 0$, $\pi/6$ and $\pi/3$ and $r = 0.55$.

$$\frac{v(r)}{V} = \frac{\eta}{1-\eta^2}\left(\frac{r_o}{r} - \frac{r}{r_o}\right) \tag{4.1}$$

where $\eta = r_i/r_o$ is the ratio of inner to outer radius and $V = \Omega r_i$ is the velocity of the inner cylinder.

Figure 4.4 (a) is the contour plot of the azimuthal velocity in a $r - z$ plane, in which the blue (darkest) line represents the minimum velocity of 0 on the outer cylinder and the red (brightest) line represents the maximum non-dimensional velocity 1 on the inner surface. The plot shows the size of the regions near the top and bottom surfaces where end effects are important, but in the central regions the flow is circular and depends on the radius only. Figure 4.4 (b) shows the azimuthal velocity along

the radius in comparison to the analytical solution. They are the same subject to discretization error.

Additional discussions including flow at higher Reynolds numbers when instability occurs will be presented in a later chapter.

4.4 Natural convection in a tall annulus with a heated inner wall

The computer code was tested for natural convection in a tall enclosed annulus where the inner cylinder is heated and outer cylinder is cooled. The analytical solution is known for the region away from the ends [37]:

$$\frac{w}{U} = \frac{1}{16(1-\eta)^2}\left\{\left[\frac{(1-\eta^2)(1-3\eta^2)-4\eta^4\ln\eta}{(1-\eta^2)^2+(1-\eta^4)\ln\eta}\right]\right.$$
$$\left[(1-\eta)^2\left(\frac{r}{L}\right)^2-1+(1-\eta^2)\frac{\ln((1-\eta)(r/L))}{\ln\eta}\right]$$
$$\left.-4\left[\left(\frac{r}{L}\right)^2(1-\eta)^2-\eta^2\right]\frac{\ln((1-\eta)(r/L))}{\ln\eta}\right\} \tag{4.2}$$

$$\frac{T}{\Delta T} = \frac{\ln((1-\eta)(r/L))}{\ln\eta} \tag{4.3}$$

Where $L = r_o - r_i$ is the width of the annular gap, $\eta = r_i/r_o$ is the ratio of inner to outer radius. $\Delta T = T_1 - T_2$ is the temperature difference between the inner and outer walls, and $U = g\beta L^3\Delta T/\nu$. The temperature T is the value of actual temperature minus that of the outer wall.

The Grashof number in this numerical study is 21.6 based on the gap L. The Prandtl number is 0.1. It was run on a $32(r) \times 128(z) \times 72(\theta)$ uniform grid. Figure 4.5 (a)

(a)

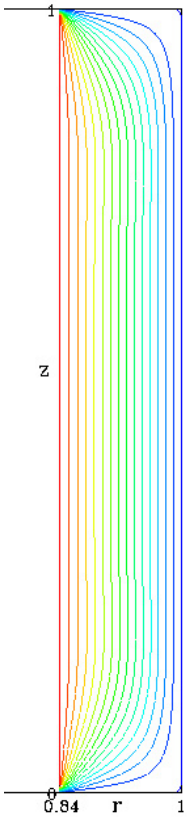

(b)

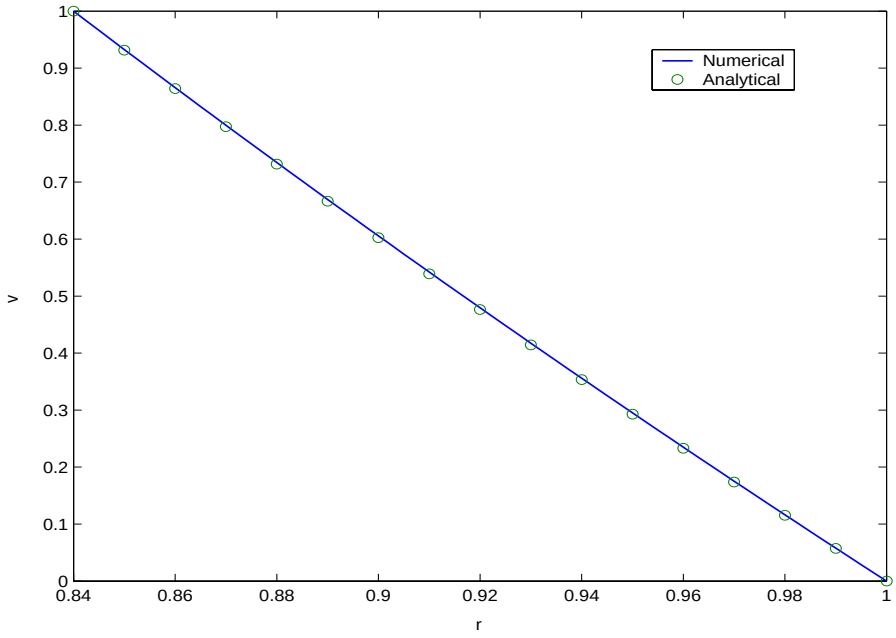

Figure 4.4: Numerical solution of Couette flow. $Ta = 28$, $r_i/r_o = 0.84$, $r_o/H = 1.0$. (a) Azimuthal velocity contours (blue/darkest = 0, red/brightest = 1), (b) Azimuthal velocity plot along the radial gap.

is the contour plot of the temperature in the bottom half of the annulus, in which the blue (darkest) line represents the minimum temperature of -0.5 on the outer surface the red (brightest) line represents the maximum temperature of 0.5 on the inner surface. The temperature result is essentially a conduction solution. Figure 4.5 (b) is the contour plot of vertical (axial) velocity, in which the blue (brightest) line represents the maximum downward flow velocity of -2.793×10^{-5} in the outer half of the gap and the red (brightest) line represents the maximum upward flow velocity of 2.874×10^{-5} in the inner half of the gap. With the exception of the two ends, the axial velocity depends on the radial coordinate only.

Figures 4.6 (a) and (b) plot the solutions along the radius in comparison to the analytical solutions. They are the same subjection to discretization error.

Natural convection with heated from bottom (Rayleigh-Bénard convection) will be discussed in a later chapter.

4.5 Flow in a lid-driven annulus

Flow in a lid-driven cavity is a classic flow problem and an excellent test case to validate new numerical techniques which solve the incompressible Navier-Stokes equations. The incompressible viscous flow in the cavity is driven by the uniform translation of the upper surface (lid). A standard test condition of $Re_L = 100$ is frequently chosen, where

$$Re_L = \frac{UL}{\nu} \tag{4.4}$$

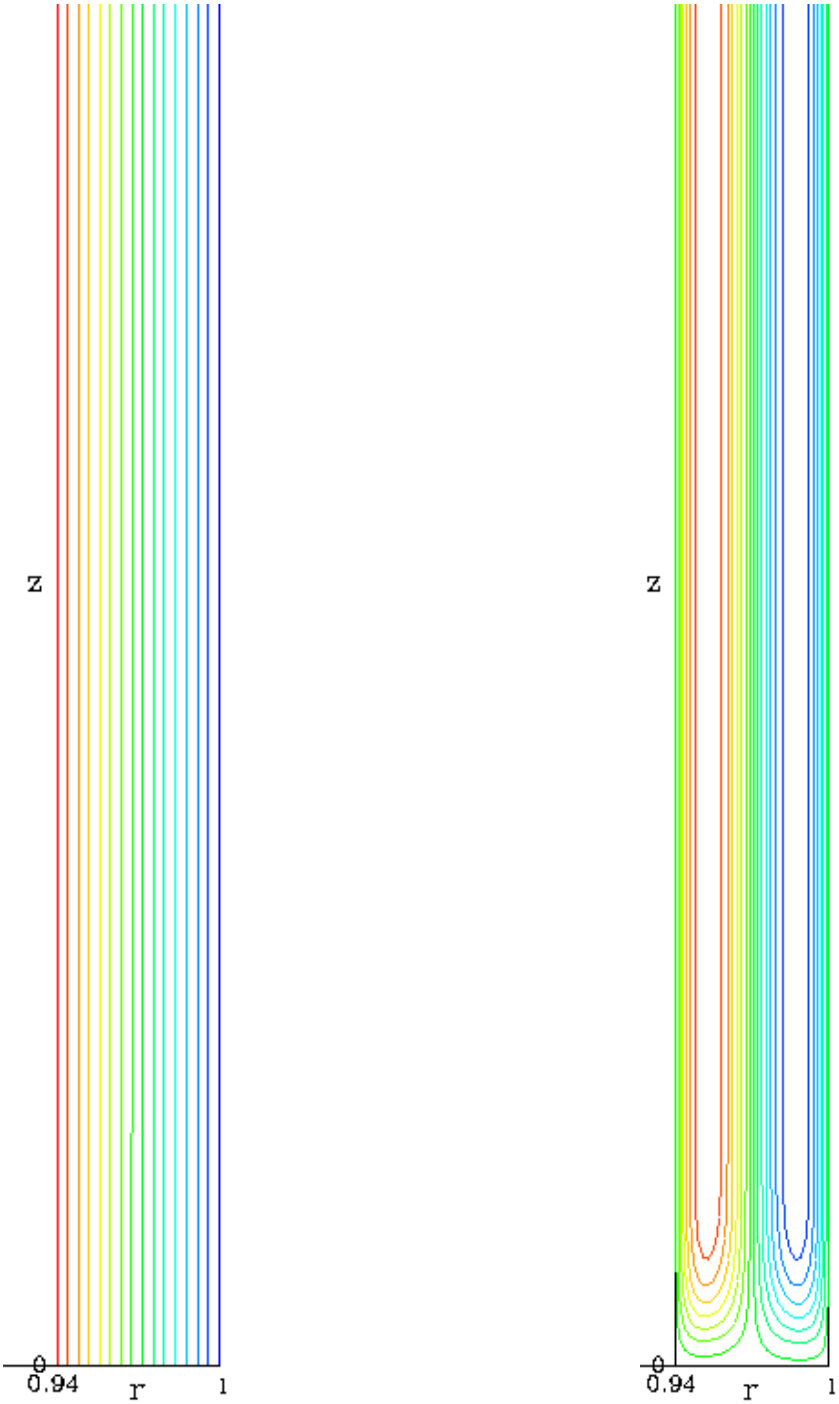

Figure 4.5: Temperature and velocity contours of natural convection in a tall annulus. $Gr = 21.6$, $Pr = 0.1$. (a) Temperature (blue/darkest $= -0.5$, red/brightest $= 0.5$), (b) Vertical (axial) velocity (blue/darkest $= -2.793 \times 10^{-5}$, red/brightest $= 2.874 \times 10^{-5}$)

(a)

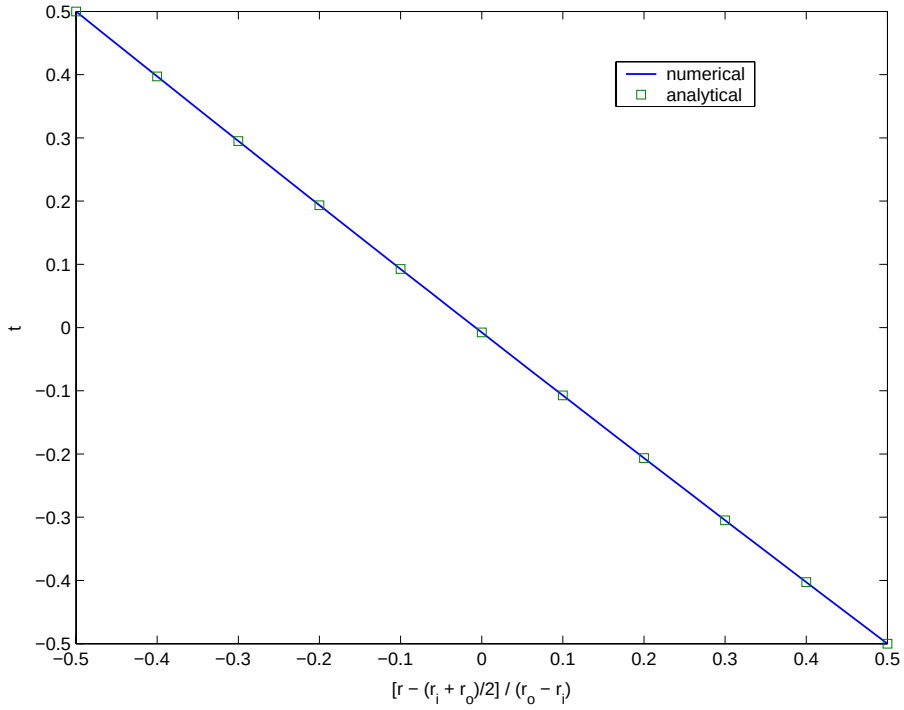

(b)

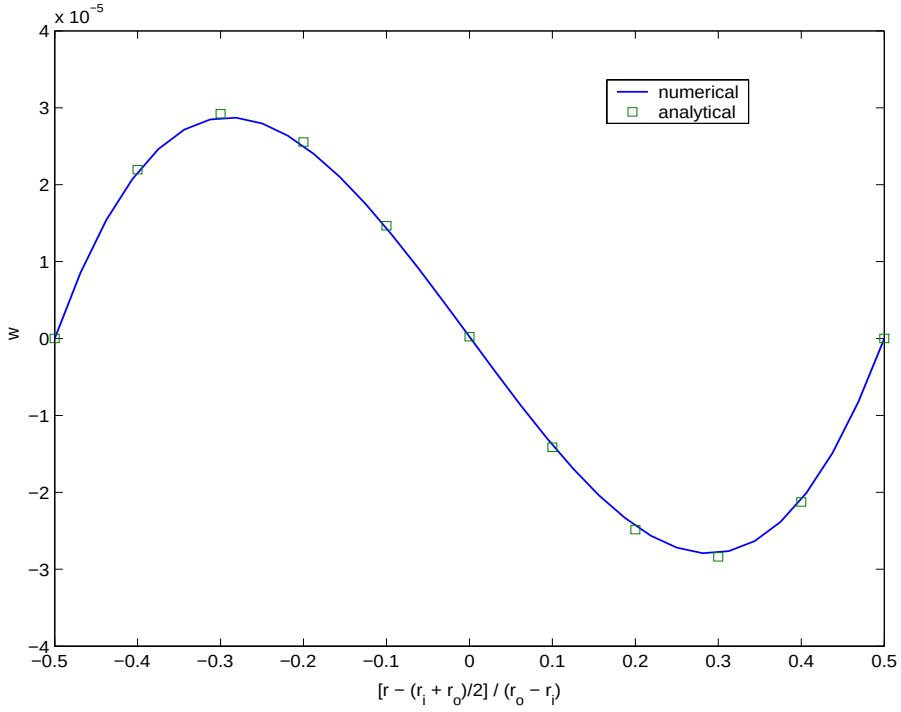

Figure 4.6: Temperature and velocity plot along the radial gap in comparison to the analytical solutions. Natural convection in a tall annulus. $Gr = 21.6$, $Pr = 0.1$. (a) Temperature, (b) Axial velocity.

and L is the width of the cavity. The lid-driven problem is also used to test the three-dimensional cylindrical code in this dissertation.

The computer code was tested with an annular cavity of $r_i = 9$, $r_o = 10$, $H = 1$ with $Re = 100$, $U = 1$ on the top surface to approximate flow in a two-dimensional square cavity, as the radius 9 to 10 is significantly greater than the gap width 1, and the effective flow cross section area is a square. A uniform grid of $64(r) \times 64(z) \times 72(\theta)$ is used in the computations. The resulting flow field is two-dimensional axisymmetric in the $r - z$ plane. All the flow variables are identical in each $r - z$ plane, and there is no flow in the θ direction. Figure 4.7 (a) plots the velocity vectors in a $r - z$ plane. (The grid density in the plot was reduced for clarity.) The flow is pulled outward from the top surface but is forced to change direction near the outer wall, resulting a single vortex near the top surface and the outer wall. Figure 4.7 (b) is the contour plot of the radial velocity, in which the blue(darkest) color represents the maximum inward velocity -0.211 near the center of the cavity and the red (brightest) line represents the maximum outward velocity of 1 on the inner cylinder. The radial velocity, as shown in Figure 4.7 (b), decelerates quickly from 1 on the top boundary till the center of the vortex. Below the vortex, it slowly accelerates again but the velocity is in the opposite direction. It reaches a peak to -0.211 near the center of the cavity, after which it reduces gradually to zero on the bottom surface. Figure 4.7 (c) is the contour plot of the axial velocity, in which the blue (darkest) color represents the maximum downward flow velocity of -0.445 near the upper outer corner and the red color (darkest) color represents the maximum upward flow velocity of 0.217 near the upper inner corner. The velocity magnitude (-0.455) in the downward flow near

the outer wall is about twice of the upward flow (0.217) near the inner wall, since the vortex is closer to the outer wall than the inner wall. Figure 4.7 (d) plots the streamlines in the same plane. They are denser near the top surface and the outer wall, but the density reduces toward the bottom and the inner walls.

Figures 4.8 (a) and (b) compare the results with some $2-D$ results published in the literatures [28](see [8]) and [8]. They are in a good agreement.

4.6 Computer performance

The numerical algorithm was coded and compiled with Fortran-77 or Fortran-90 compiler. Most of the numerical studies were performed on Cray T932 where the code was compiled with default 64-bit option. Fieldview by Intelligent Light has been used for postprocessing. Lid-driven flow in an annulus with radius of 0.1 to 1 and height of 1 was used as a model program for performance study. The tests were done with two grid structures, one with three-dimensional grids of $32(r) \times 32(z) \times 72(\theta)$, and another with doubling the density in each coordinate. A total of 100 time steps were iterated.

Table 4.1 lists the CPU time to solve the three-dimensional pressure Poisson equation for the generalized eigenvalues and eigenvectors and the CPU time for solving for the five variables u, v, w, t, and p from the governing equations. The CPU time for 100 time steps is listed and the CPU time for each time step (excluding the read and write operations) is also given. The CPU time for the two-dimensional axisymmetric

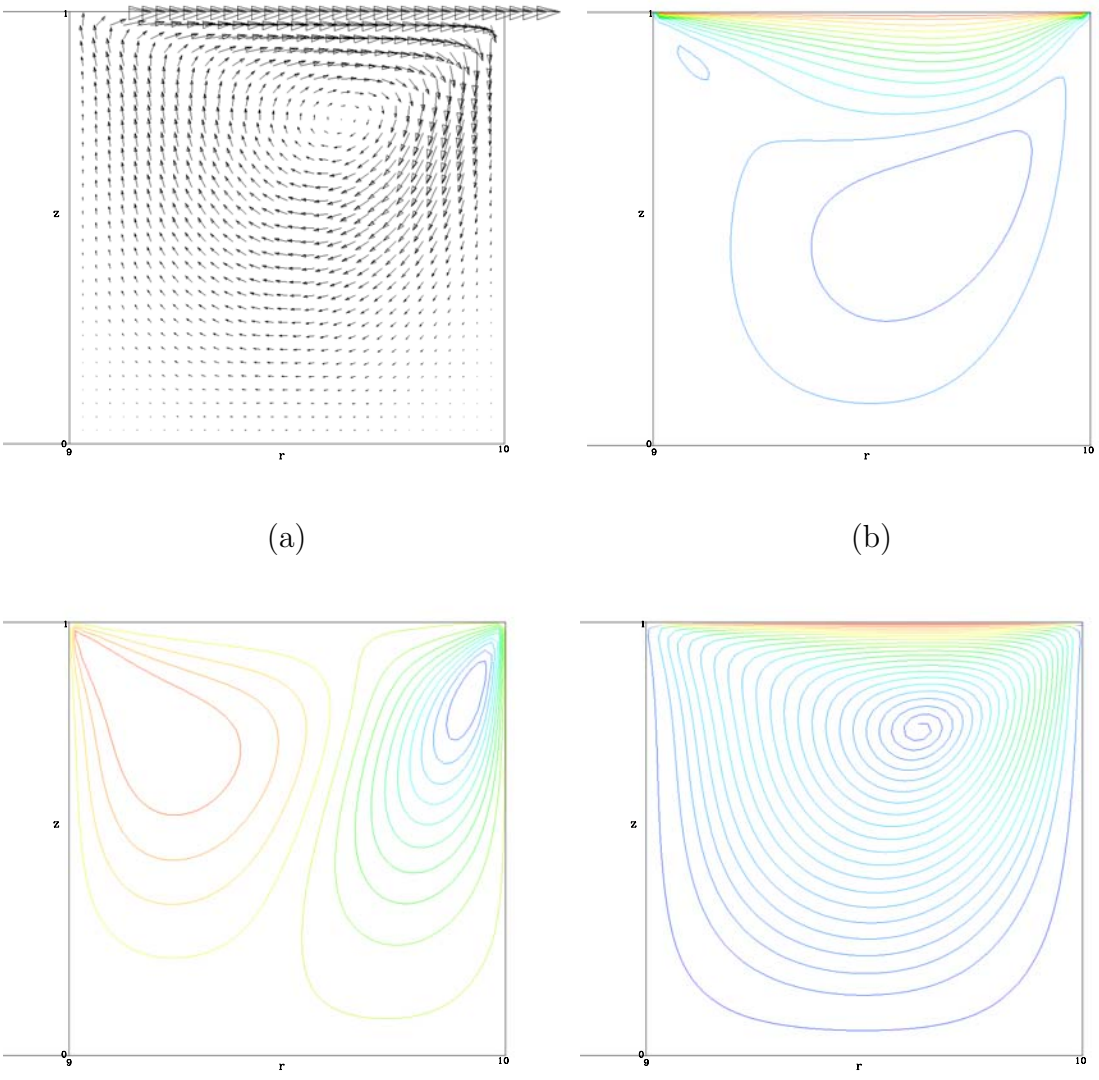

Figure 4.7: Numerical solution for a flow in a lid driven annulus, $Re = 100$. (a) Vector plot, (b) Radial velocity contours (blue/darkest $= -0.211$, red/brightest $= 1$); (c) Vertical velocity contours (blue/darkest $= -0.455$, red/brightest $= 0.217$), (d) Stream function in a $r-z$ plane (The sprial form of the streamline here and elsewhere is a result of the way in which the postprocessing software calculates it. Clearly the streamlines should form closed loops.)

(a)

(b)

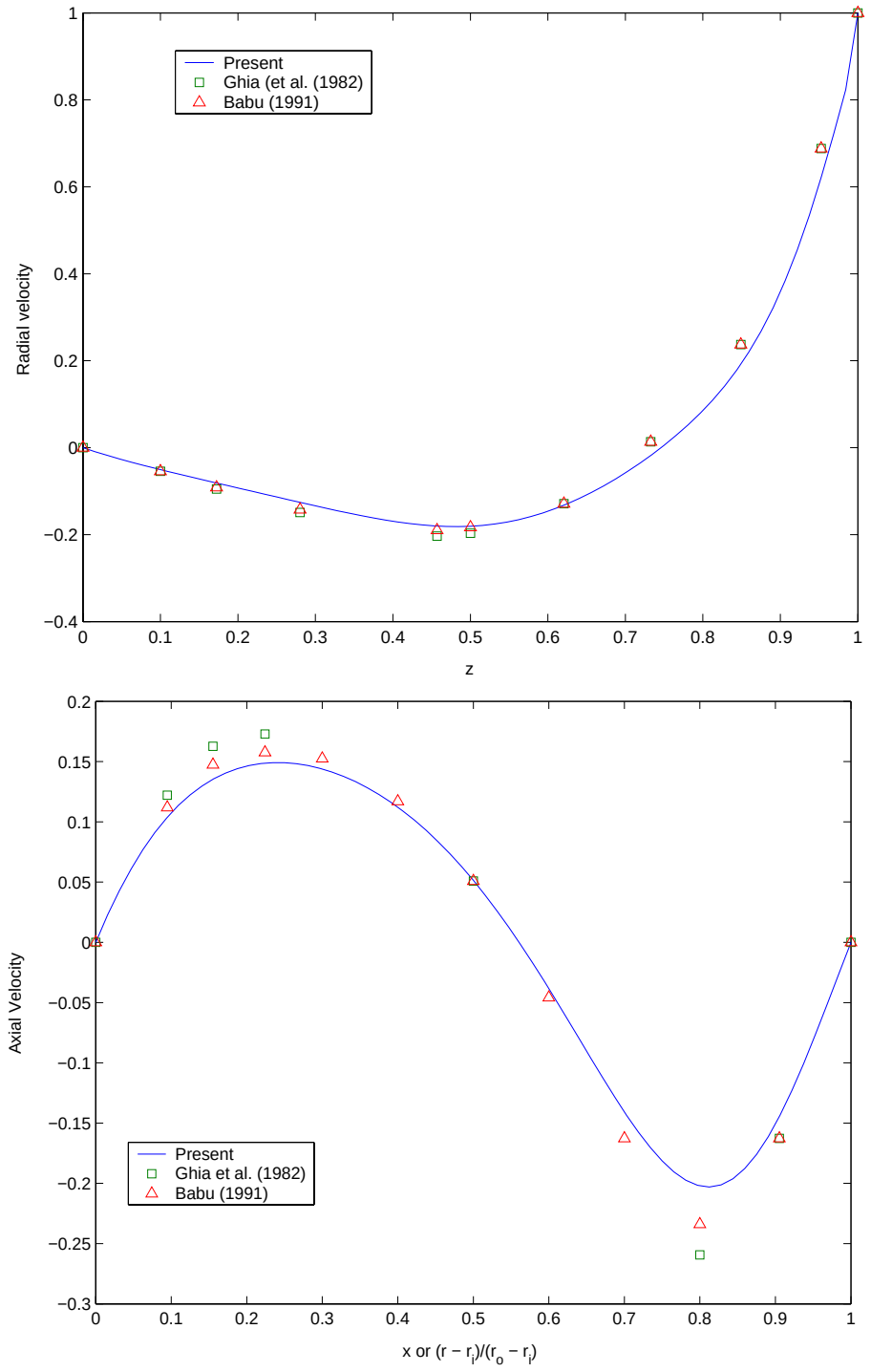

Figure 4.8: Comparison of numerical solution with literature data for flows a lid driven cavity for $Re = 100$. (a) Radial velocity on $r = (r_i + r_o)/2$. (b) Axial velocity on $z = 0.5$)

grid	$32 \times 72(\theta)$	$64 \times 64(z) \times 144(\theta)$
pressure Poisson equation solver	1.172 seconds	9.111 seconds
100 time steps for u, v, w, t, p	552.093 seconds	4906.438 seconds
each time step for u, v, w, t, p	5.507 seconds	46.829 seconds

Table 4.1: CPU time to run the three-dimensional code

grid	$32(r) \times 32(z)$	$64(r) \times 64(z)$
pressure Poisson equation solver	0.072 seconds	0.479 seconds
100 time steps for u, v, w, t, p	3.879 seconds	16.922 seconds
each time step for u, v, w, t, p	0.039 seconds	0.169 seconds

Table 4.2: CPU time to run the axisymmetric code

code to solve the pressure Poisson equation and the governing equations is given in Table 4.2.

CHAPTER 5

THERMOCAPILLARY CONVECTION

5.1 Introduction

Thermocapillary convection is a fluid motion driven by surface tension variation at the free surface resulting from thermal gradients along the surface. It is a special case of Marangoni convection, which is a general term for tension-driven fluid motions. Variation in surface tension can occur for other reasons as well. Examples include variations in the surface tension caused by electric charge, and changes in concentration of surface active species. If the temperature variation is the only contribution to the surface tension gradient, the term thermocapillary convection is commonly used. When a surface tension exists on a free surface, the fluid particles on the surface will be pulled from regions of low surface tension to regions of higher surface tension. The resulting surface motion induces shear stresses in the fluid interior, and the shear stresses in turn cause the fluid to flow. Thermocapillary convection is of interest in a reduced gravity environment of material processing such as zone refining and crystal growth from melts. Owing to reduced gravity in space, natural convection is greatly

reduced there and the transport phenomena associated with thermocapillarity convection can become prominent in space.

The code in this dissertation is primarily developed to solve for thermocapillary convection. The major difference from the fixed boundary problems (lid driven flow, natural convection, and Couette-Taylor flow) is that the radial and azimuthal velocities on the top surface are free instead of prescribed for the lid-driven flow or fixed for the pure natural convection. For thermocapillary flow, it is optional to include the gravity term as well. However, in this study, the gravity term is ignored by setting Gr to be zero.

5.2 Thermocapillary convection with uniform thermal boundary condition

The code was run to solve a thermocapillary convection in an annular cavity of $r_i = 0.1$, $r_o = 1$, and $H = 1$ with a $64(r) \times 64(z) \times 72(\theta)$ uniform grid. The temperatures on the inner and outer surfaces are 0.5 and -0.5 respectively. The Reynolds number and Prandtl number are 100.0 and 1.0. Figure 5.1 (a) is the velocity vector plot. The resulting flow at steady state is two-dimensional without azimuthal velocity component. The flow field is similar to the lid-driven cavity flow, except the velocity on the free surface is no longer constant. The flow is pulled from hot region near the inner surface to the cold region near the outer surface. Figure 5.1 (b) is the contour plot of the temperature in a $r - z$ plane, in which the blue (darkest) color represents the minimum temperature of -0.5 on the outer surface and the red (brightest) color represents the maximum temperature of 0.5 on the inner surface. The temperature

near the bottom surface is primarily a conduction solution since the flow is very weak there. The isotherms near the free surface shift outward as a result of thermocapillary convection. Figure 5.1 (c) is the contour plot of the radial velocity, in which the blue (darkest) color represents the maximum inward flow velocity of -0.018 and the red (brightest) color represents the maximum outward flow velocity of 0.106. The high velocity on the free surface becomes the driving force for the flow in the cavity. The velocity on the free surface and immediately below it accelerates outward till the central region $r = 0.48$, where it reaches the peak value (0.106). It then loses its momentum as the flow approaches the outer wall, where the flow changes its direction. The return inward flow, which occupies most of the space, is much slower than the driving outward flow, primarily to satisfy the continuity constraint. Figure 5.1 (d) is the contour plot of the axial velocity, in which the blue (darkest) color represents the maximum downward flow velocity of -0.0265 and the red (brightest) color represents the maximum upward flow velocity of 0.0459. Similar to the lid driven flow, the axial flow in the thermocapillary convection is upward near the inner wall and downward near the outer wall. The flow is faster at the upper inner corner and upper outer corner, and slower near the bottom surface and in the center region.

The velocity variations along the r and z coordinates can be seen quantitatively from the plots (a) to (d) in Figure 5.2. Figure 5.2 (a) is the plot of the radial velocity on the free surface, which shows the sharp gradient near the inner surface, and the peak value 0.106 at $r = 0.48$. Figure 5.2 (b) is the plot of the radial velocity in the middle surface ($r = 0.55$), where it shows the maximum velocity of inward flow ($u = -0.018$) around $z = 0.625$. The inward flow velocity on the free surface

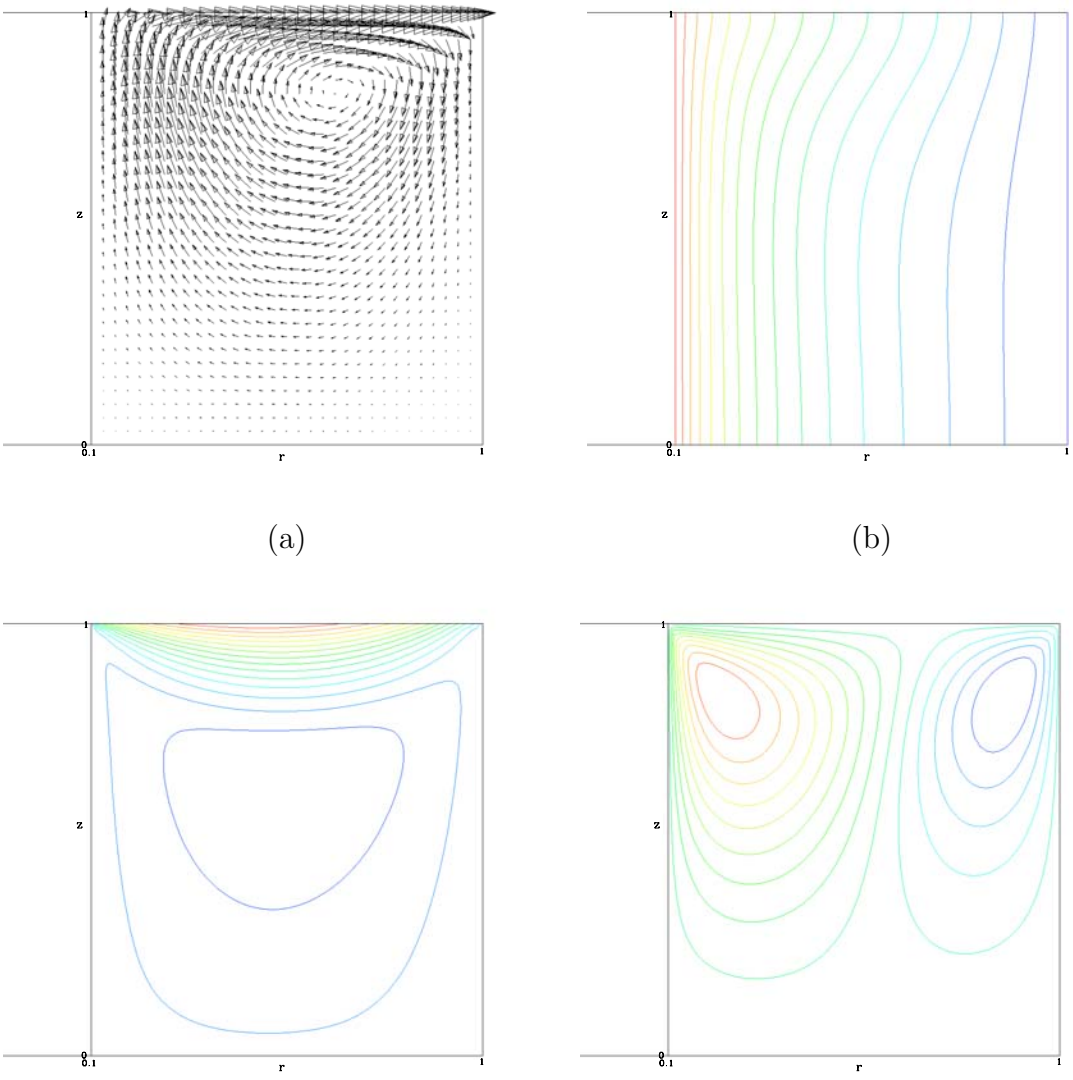

Figure 5.1: Numerical solution of thermocapillary convection. $Re_H = 100$, $Pr = 1$, $r_i = 0.1$, $r_o = 1$. (a) Velocity vector plot; (b) Temperature (blue/darkest $= -0.5$, red/brightest $= 0.5$) contours; (c) Radial velocity contours (blue/darkest $= -0.018$, red/brightest $= 0.106$); (d) Axial velocity contours (blue/darkest $= -0.0265$, red/brightest $= 0.0459$) in a $r - z$ plane.

(0.104) is very close to the maximum value (0.106) at $r = 0.48$. Figure 5.2 (c) is the plot of axial velocity on $z = 0.828$ which corresponds to the locations of maximum upward and downward flows, and $z = 0.5$ the middle height location. Figure 5.2 (d) is the plot of axial velocity on $r = 0.2266$, 0.5, and 0.8875, which correspond to the locations of maximum upward flow, middle height, and maximum downward flow.

5.3 Thermocapillary convection with non-uniform thermal boundary condition

To introduce three-dimensionality into the flow field, a non-uniform thermal boundary condition was introduced on the inner surface.

$$T_1(r_i, \theta, z) = \bar{T}_1(1 + \varepsilon \sin n\theta) \tag{5.1}$$

The value $\varepsilon = 0.3$ and $n = 1$ are used in this problem. T_1 and $\bar{T}_1$ here are non-dimensional temperatures on the inner surface. A non-uniform grid of $64(r) \times 32(z) \times \theta(72)$ was used with the streching factor $\alpha = 1.2$ so that the grid is denser toward both ends of the r coordinate and the upper side of the z coordinate (α is defined in 3.24). The velocity vector, temperature, radial velocity, and the axial velocity distribution in each $r - z$ plane is similar to the case for the uniform boundary condition with slightly different magnitude and thus are not plotted here. However, because there is a temperature gradient in the circumferential direction on the inner surface, there is a tangential flow starting from the free surface near the inner surface, as shown in Figure 5.3 (a), which plots the azimuthal velocity contours on $\theta = 0$ section, and (b), which plots the azimuthal velocity contours on the free surface. The blue (darkest)

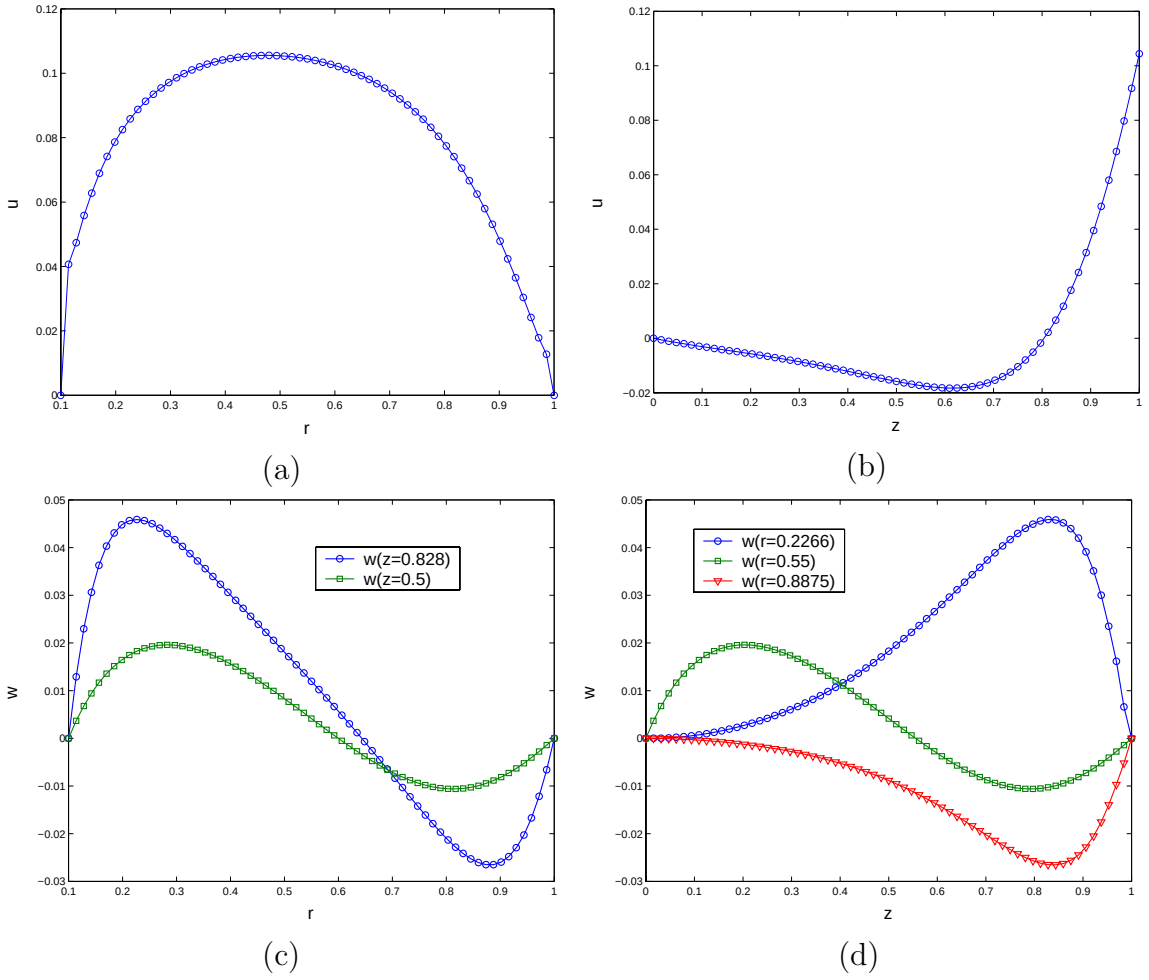

Figure 5.2: Plots of velocity variation along r and z coordinates in thermocapillary convection. (a) Radial velocity on the free surface, (b) Radial velocity on $r = 0.55$, (c) Axial velocity on $z = 0.828$ and 0.5, (d) Axial velocity on $r = 0.2266$, 0.5, and 0.8875.

color in 5.3 (a) and (b) represents the maximum radial velocity of -5.025×10^{-3} in the counter-clockwise direction and the red (brightest) color represents the maximum radial velocity of 5.025×10^{-3} in the clockwise direction. Figure 5.3 (c) is the contour plot of the radial velocity, in which the blue (darkest) color represents the maximum inward flow velocity of -0.0233 in the central region of the cavity and the red (brightest) color represents the maximum outward flow velocity of 0.1205 on the free surface. Figure 5.3 (d) is the contour plot of the temperature on the free surface, with the blue (darkest) color representing the minimum temperature of -0.5 on the outer radius the red (brightest) color representing the maximum temperature of 0.65 at $\theta = \pi/2$ on the inner radius. As expected, most of the three-dimensionality occurs near the inner surface where the non-uniform thermal boundary is imposed. Although the influence of the sinusoidal disturbance from the inner boundary temperature is carried to every point in the flow, the three-dimensionality reduces for the flow far away from the inner surface.

The influence of the sinusoidal inner thermal boundary condition to the flow field can be seen from Figures 5.4 (a), (b), and (c) which plot the radial velocity, azimuthal velocity, and temperature on the free surface varying with the θ coordinate at different radii r, and Figure 5.4 (d) which plots the axial velocity in the middle height plane ($z = 0.5$) varying with θ coordinate at different radii (r).

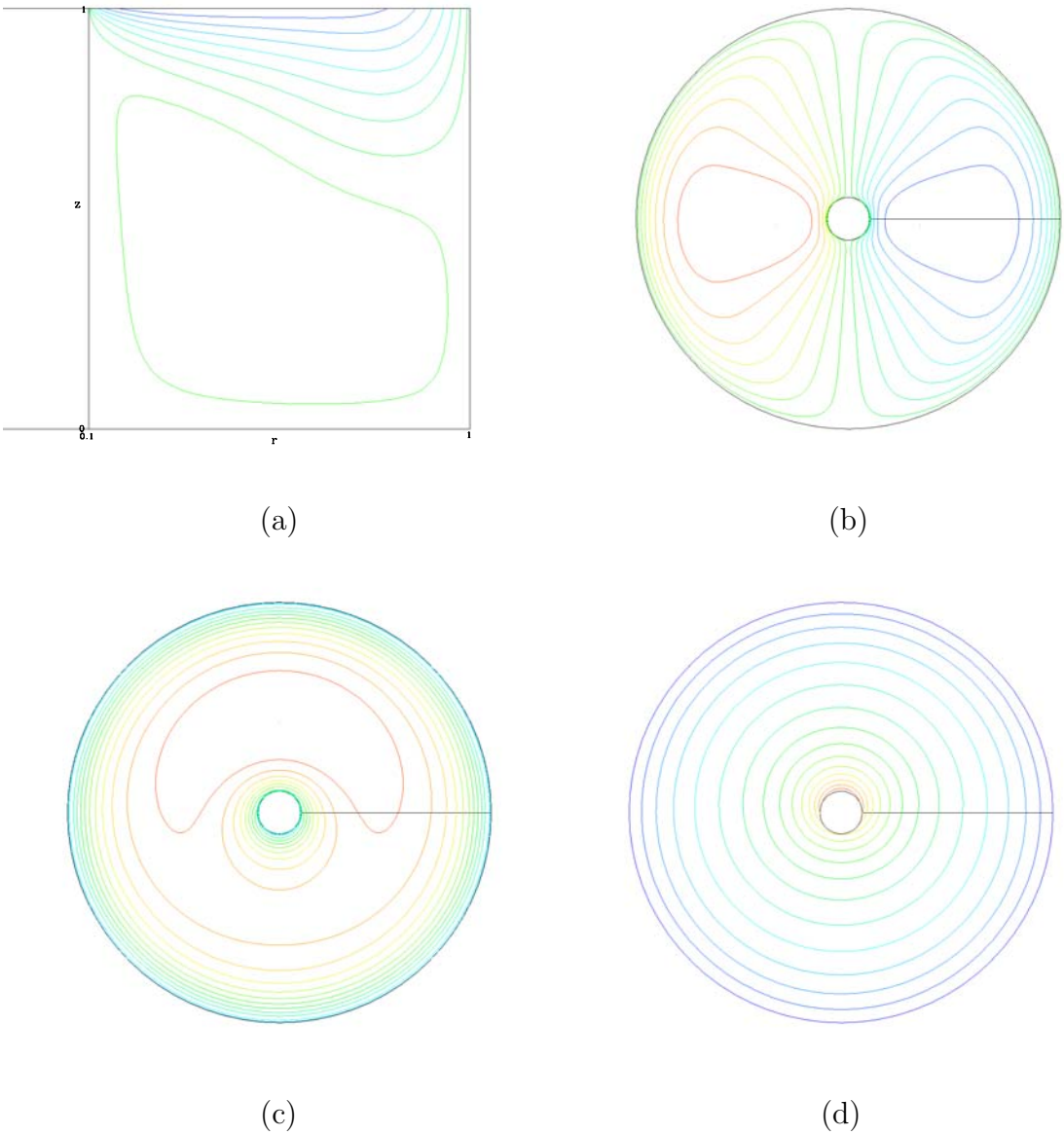

(a) (b)

(c) (d)

Figure 5.3: Velocity and temperature contours of thermocapillary convection with non-uniform thermal boundary condition on the inner cylinder. $Re = 100$, $Pr = 1$. (a) Azimuthal velocity contours on $\theta = 0$ (blue/darkest $= -5.025 \times 10^{-3}$, red/brightest $= 5.025 \times 10^{-3}$); (b) Azimuthal velocity contours on the free surface (blue/darkest $= -5.025 \times 10^{-3}$, red/brightest $= 5.025 \times 10^{-3}$); (c) Radial velocity contours on the free surface (blue/darkest $= -0.0233$, red/brightest $= 0.1205$); (d) Temperature contours on the free surface (blue/darkest $= -0.5$, red/darkest $= 0.65$).

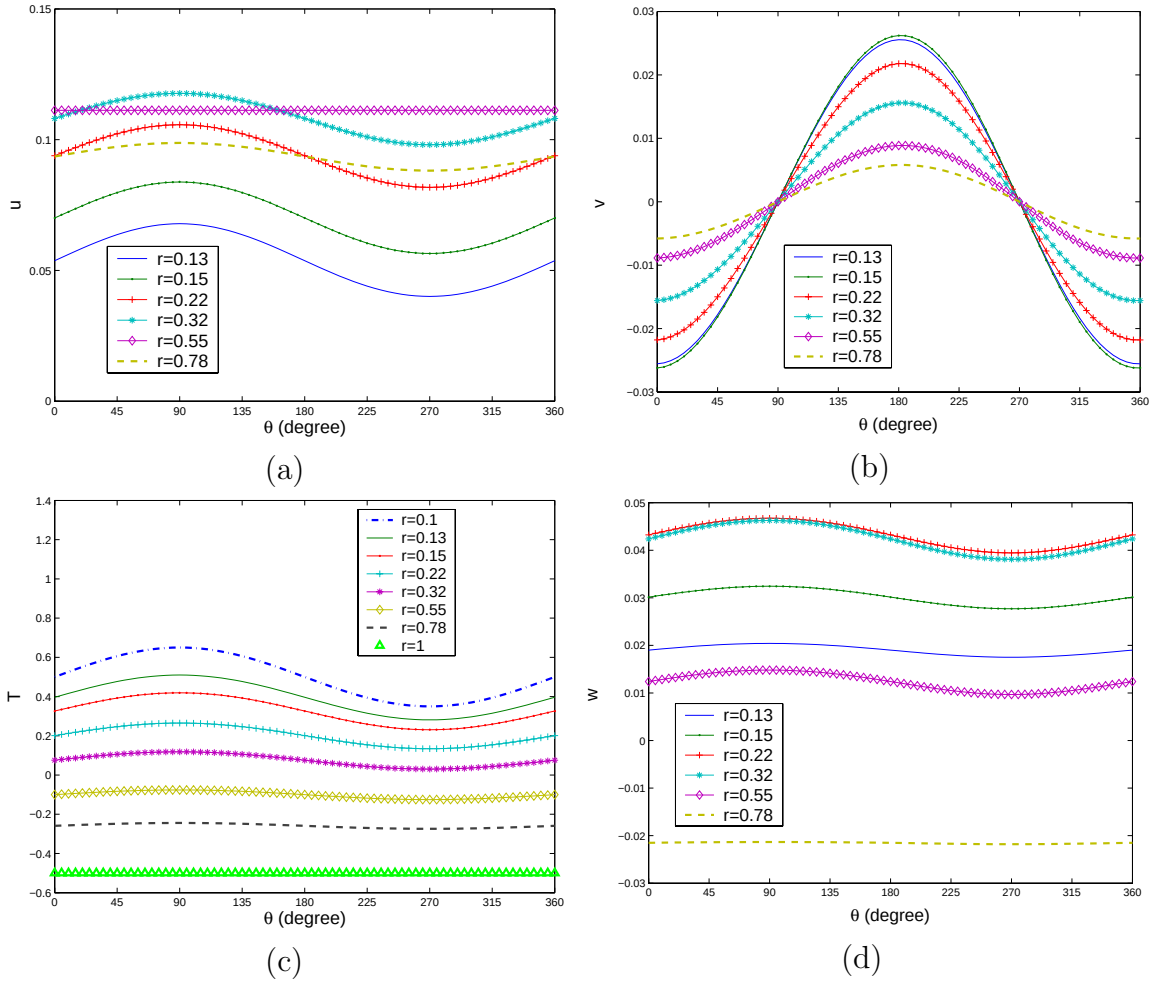

Figure 5.4: Velocities and temperature vary with θ at different radii in thermocapillary convection with non-uniform boundary thermal condtition. (a) Free surface radial velocity, (b) Free surface azimuthal velocity, (c) Free surface temperature, (d) Axial velocity on $z = 0.5$.

CHAPTER 6

THERMAL CONVECTION IN A SHALLOW CAVITY HEATED FROM BELOW (RAYLEIGH-BÉNARD CONVECTION)

6.1 Introduction

The problem of thermal instability in a horizontal layer of fluid heated from below has been the subject for study of hydrodynamic stability, since Bénard's experiment in 1900 (see [16], [39]). Consider a thin layer of fluid, in which the bottom is kept at higher temperature than the top. Owing to the adverse temperature gradient, the fluid at the bottom is lighter than the fluid at the top. This top-heavy arrangement is potentially unstable, so there will be a tendency for the fluid to redistribute itself. However, this natural tendency will be inhibited by its own viscosity. Therefore, the adverse temperature gradient must exceed a certain value before the instability can take place [38].

In 1900 Bénard investigated the motion in a fluid layer, with a free surface and heated from below. He noticed a regular cellular pattern of hexagonal convection cells. Based on the stability of normal modes of the equations, Rayleigh explained this in 1916 [57] (see [39]) by investigating the stability of disturbance. He assumed the fluid to

be fully confined between the two horizontal rigid plates instead of the free surface in the original Bénard experiment. It was later understood that in buoyancy driven convection the expected pattern would be a stripe pattern of convection rolls, rather than the cellular pattern observed by Bénard. The convection observed by Bénard is now understood to be driven by temperature dependent surface tension forces rather than by buoyancy. Nevertheless, the stripe or roll state formed in buoyancy driven convection is today referred to as Rayleigh-Bénard convection. Surface tension induced convection is known as Marangoni convection (or thermocapillary convection for temperature dependent surface tension gradient).

The related problem has attracted many experimental and analytical studies. Chandrasekhar [16] summarized these studies presented recalculations for the solutions for the critical Rayleigh number and the cellular patterns, as well as the associated wave numbers and wave length. He showed that the critical Rayleigh number and the wave length (the total cell width normalized to the gap height) are 1707.8 and 2.016 for the case in which both top and bottom surfaces are fixed, and 1100.7 and 2.342 if the top surface is free while the bottom surface is fixed.

Numerical studies on the problem with primitive variables have been limited in the past owing to limitation in computer power. One reason is that it still requires a large number of time steps before a steady solution is reached. Polezhaev and Yaremchuk, using vorticity-stream function approach from a Russian commercial package called COMGA, studied the cell formation in a two-dimension thin slot [54]. Recent studies include Paul and et al. [53], who using a parallel spectral element algorithm,

performed numerical simulations of Rayleigh-Bénard convection in cylindrical and rectangular domains for a range of aspect ratios from 5 to 60 and compared the numerical results to theory and experiment. More recently, Paul and Catton [52], using a pseudospectral method and a Fourier integral method, studied two-dimensional roll relaxation in Rayleigh-Bénard convection.

In this dissertation, both the full three-dimensional code and two-dimensional axisymmetric code were used to solve the governing equations. All the studies were done in an annular geometry with aspect ratio (gap to height) ranging from 4 to 7.2. The Rayleigh number ranged from $2,800$ to $280,000$, all exceeding the critical value. The initial condition is a fluid at rest, but the thermal field varies linearly along the vertical gap. In most cases a single disturbance on temperature at the center grid was used for initiation of the thermal instability.

6.2 Rayleigh-Bénard convection study with the two-dimensional axisymmetric code

Rayleigh-Bénard convection was studied with the two-dimensional axisymmetric code, simplified from the full three-dimensional code. The gap to height ratio is 7.2 - inner radius of 0.8 and the outer radius 8 while height being unity. The Reyleigh number is 2800, 1.64 times the critical number of 1708. The Rayleigh number of 2800 can be the result of either case with Grashof number of 400 and Prandtl number of 7, or Grashof number of 4000 and Prandtl number of 0.7. A uniform grid of $32(r) \times (z)128$ was used in the study. The same flow pattern was obtained for both cases. Figure 6.1 (a) is the contour plot of the radial velocity, in which the red (brightest) color

represents the maximum outward velocity of 3.427×10^{-3}, and the blue (darkest) color represents the maximum inward velocity of -3.411×10^{-3}. Figure 6.1 (b) is the contour plot of the vertical (axial) velocity, in which the red (brightest) color represents the maximum upward velocity of 3.535×10^{-3} and the blue (darkest) color represents the maximum downward velocity of -3.535×10^{-3}. Figure 6.1 (c) is the plot of the streamlines. There are eight stationary cells of identical height and width (width to height ratio is 0.9), with the axis in θ direction. Each cell rotates in the opposite direction with the neighboring cells. Figure 6.1 (d) is the contour plot of temperature, in which the red (brightest) color represents the maximum velocity of 0.5 and the blue (darkest) color represents the minimum velocity of -0.5. The plot shows the temperature gradient varying with the vertical velocity, and the gradient is higher near the bottom for the downward flow and is higher near the top for the upward flow.

6.2.1 Effect of aspect ratio

In addition to aspect ratio of 7.2, in which the flow consists of 8 stable cells and have a wave length of 1.8, cases with different aspect ratios ($L/H = 6$ and 4) were run for Rayleigh number of 2800. In the case of aspect ratio of 6, the number of the cells are also changed to 6 with the wave length of 2.0 and the same size and intensity among the cells. In the case of aspect ratio aspect ratio 4, the number of the cells are 4 with the wave length of 2.0 and the same size and the intensity among the cells.

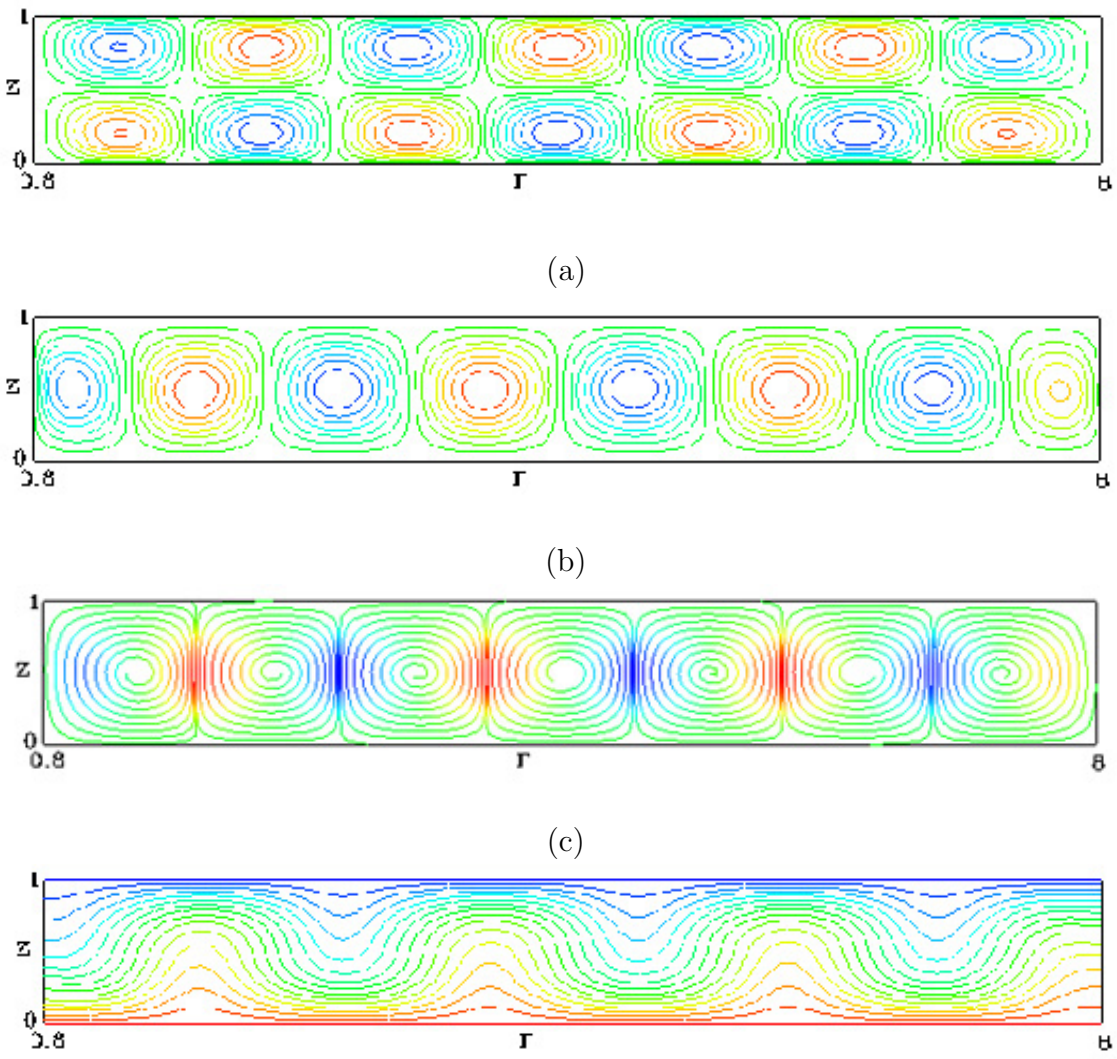

Figure 6.1: Contour plots and streamlines of Rayleigh-Bénard convection in a shallow annulus. $Gr = 400$, $Pr = 7$. $r_i/r_o = 0.1$, $r_o/H = 8$. (a) Radial velocity contours (blue/darkest $= -3.411 \times 10^{-3}$, red/brightest $= 3.427 \times 10^{-3}$), (b) Vertical velocity contours (blue/darkest $= -3.535 \times 10^{-3}$, red/brightest $= 3.535 \times 10^{-3}$), (c) Streamlines, (d) Temperature contours (blue/darkest $= -0.5$, red/brightest $= 0.5$.)

6.2.2 Effect of Rayleigh number

The flow pattern changes for higher Rayleigh numbers. For Grashof number of $4,000$ and a Prandtl number of 7, the resulting Rayleigh number is about 16 times the critical value. Convection of this type is considered supercritical and the resulting flow is time-dependent [39]. Figures 6.2 (a), (b), (c), (d) and (e) are examples of the flow patterns at different time steps. The code was run with the same geometry and grid used in the case of Figure 6.1. It starts with 10 cells in the slot after the flow is fully developed around (non-dimensional) time $2,000$. The innermost cell has collapsed to a half cell at time $9,000$, and completely disappears at time $15,000$. The cells continue to adjust and reduce in number with gradual collapsing of the innermost cell. At time $100,000$, the number of the cells is reduced to 5. After many more time steps, the flow eventually reaches steady state with four full size cells and one reduced cell next to the inner wall ($time = 200,000$ to $400,000$).

Figures 6.3 (a) and (b) plot the temperature and the vertical (axial) velocity change with time on the middle height ($z = 1/2$) and three grid points along the radius $r = 4.4$, 2.6, and 6.2, corresponsing to $(r - r_i)/(r_o - r_i) = 1/4, 1/2$, and $3/4$, respectively. The velocity shifts between upward flow and downward flow during the cell adjustments, and then become monotonic and eventually constant.

According to linear stability theory, a continuum of unstable flow exists for supercritical Rayleigh number [39]. It is possible that there exists a number of wave lengths, some larger and some smaller than the theoretical wave length of 3.117. Koschmieder

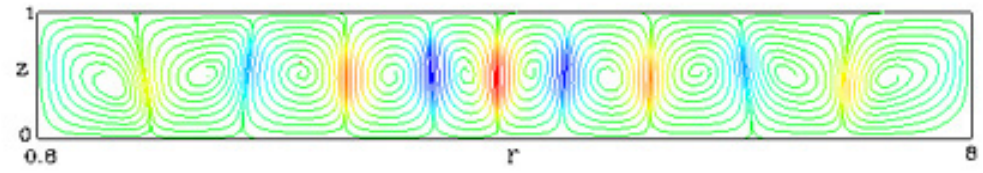

(a)

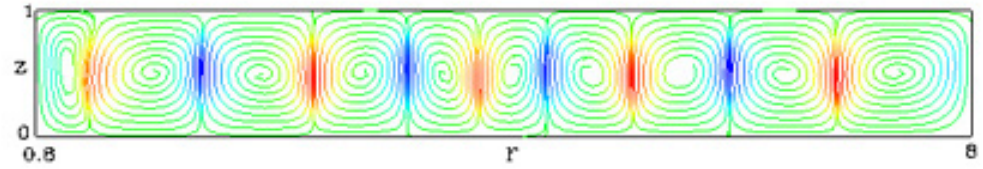

(b)

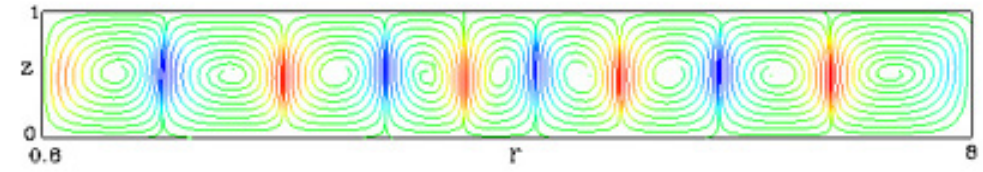

(c)

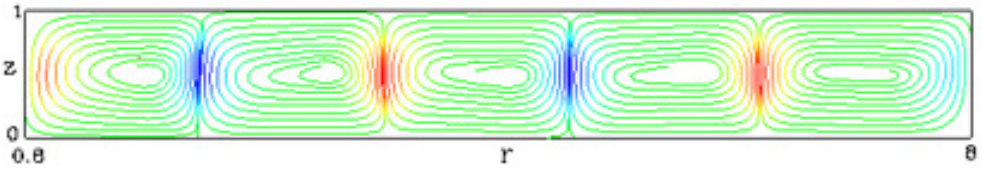

(d)

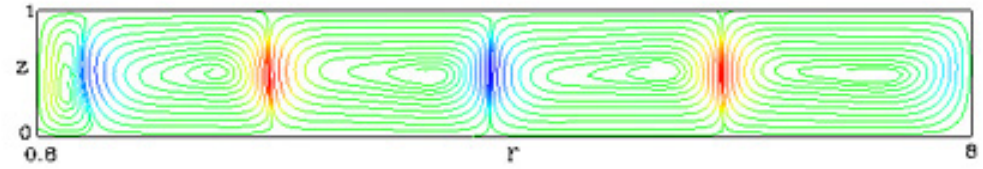

(e)

Figure 6.2: Streamline plots at different time steps. $Gr = 4000$, $Pr = 7$. (a) (non-dimensional) $time = 2,000$. (b) $time = 9,000$. (c) $time = 15,000$. (d) $time = 100,000$. (e) $time = 200,000$ - $400,000$ (steady state solution).

(a)

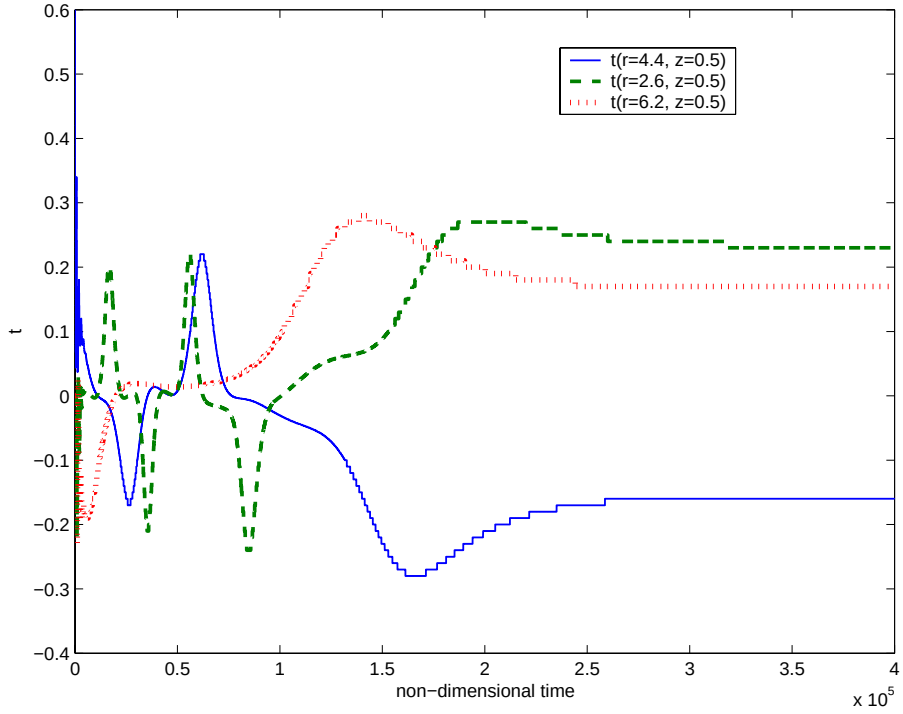

(b)

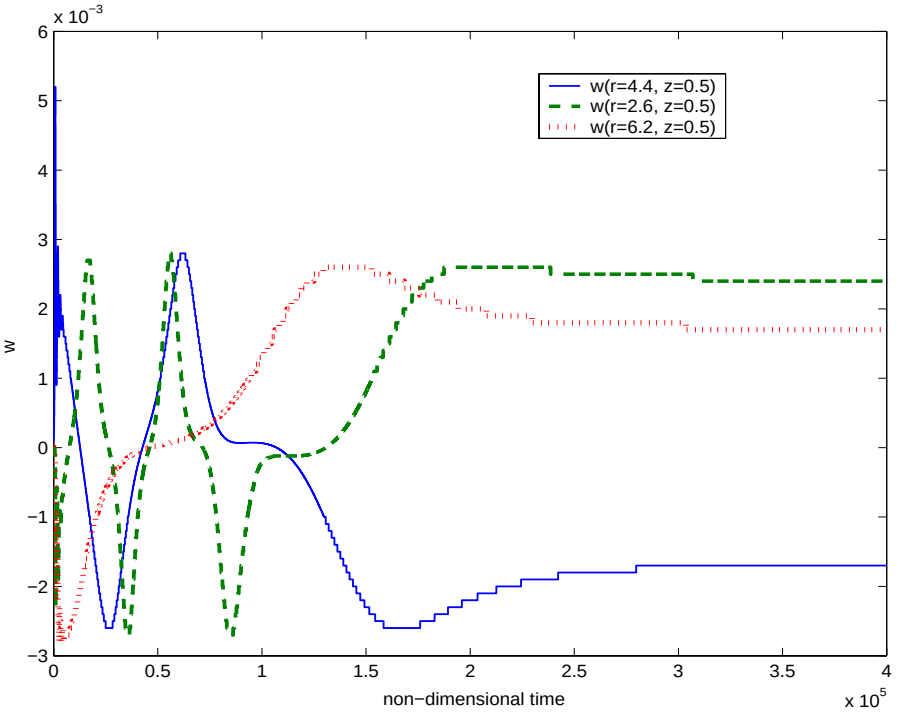

Figure 6.3: Temperature and velocity varying with time on the middle height ($z = 1/2$) and three radii: $r = 4.4$, 2.6 and 6.2. (a) Temperature, (b) Vertical (axial) velocity.

[39] discussed two theories whether the wave length of the cell pattern increases or decreases with the Rayleigh number. Based on the results in this numerical study with a series of solutions at different time steps, the wave length appears to be initially smaller than the critical value - more cells inside the slot (Fig. 6.2 (a)). However, as time progresses, the cells constantly merge and adjust themselves (Figures 6.2 (b) - (e)). The innermost cell typically reduces in size with time until it either becomes distorted to smaller size (e.g. $Ra = 28,000$ in Figure 6.2 (e)), or disappears completely (e.g. $Ra = 14,000$ - similar to Figures 6.2 (d)). The average wave length of the cells in the slot in the meantime increases with time, and eventually becomes smaller than the critical wave length. Therefore in steady state, it is possible to have several cells of same size (5 complete cells for $Ra = 14,000$ case - similar to Figure 6.2 (d)), or a smaller cell in addition to complete cells (4 complete cells and a smaller cell for $Ra = 28,000$ case as in Figure 6.2 (e)). The trend is in agreement with the stability diagram in Koschmieder [39].

6.3 Rayleigh-Bénard convection study with the three-dimensional code

With uniform thermal boundary condition, circular concentric rolls are expected with Rayleigh number exceeding the critical value. The numerical solution shows this is indeed to be true with initial zero velocity condition and initial linear temperature distribution. The three-dimensional code was run with a uniform grid of $64(r) \times 16(z) \times 48(\theta)$ in a geometry of height 1, outer radius 6 and inner radius of 0.06 to simulate the Rayleigh-Bénard convection in a circular disk. The Grashof number is 400 and the Prandtl number is 7, resulting Rayleigh number of 2800, about 1.64

times the critical Rayleigh number for an infinite shallow slot. Figures 6.4 (a) is the contour plot of temperature in the middle z plane, with the blue (darkest) color representing the minimum (non-dimensional) temperature of -0.5 and the red (brightest) color representing the maximum temperature of 0.5. Figures 6.4 is the contour plot of vertical (axial) velocity in the middle z plane, with the blue (darkest) color representing the maximum downward flow velocity of -3.656×10^{-3} and the red (brightest) color representing the maximum upward flow velocity of 4.182×10^{-3}. The solution is two-dimensional axisymmetric flow without azimuthal component. The disk is filled with concentric stripes of four upward and warmer rolls (brighter color) and three downward and colder rolls (darker color). These stripes characterized by the changes of the vertical flow directions or temperatures are easily visualized in experiments [39].

Figures 6.5 (a) is the contour plot of temperature on $\theta = 0$ section. Figure 6.5 (b) is the contour plot of the vertical (axial) velocity on $\theta = 0$ section. The color representations in the contour plots are the same as explained in Figure 6.4. Figure 6.5 (c) is the contour plot of radial velocity, with blue (darkest) color representing the maximum inward velocity of -3.370×10^{-3} and the red (brightest) color representing the maximum outward velocity of 3.402×10^{-3}. The shape of the inner five cells is approximately square, but the widths of the two cells next to the inner and outer cylinders are reduced.

6.3.1 Rayleigh-Bénard convection with an initial temperature disturbance

The solution with axisymmetric flow and concentric rolls may be distorted by an initial disturbance. One case was run with an initial temperature disturbance at the

(a)

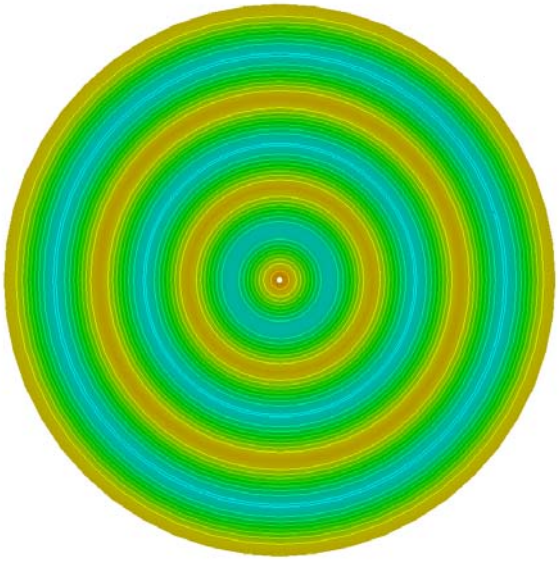

(b)

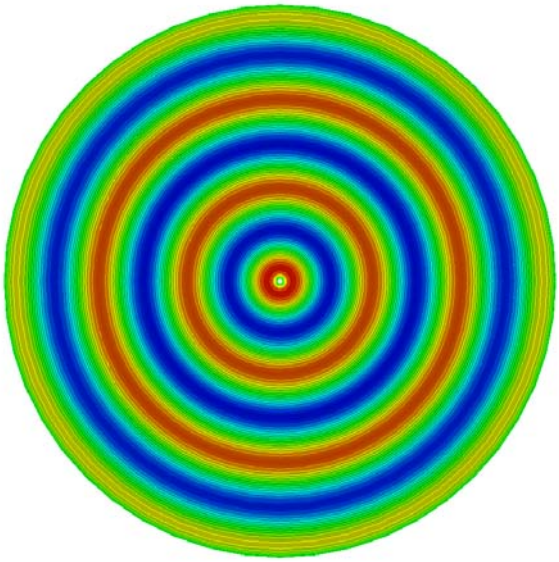

Figure 6.4: Temperature and velocity contours on $z = 0.5$. (a) Temperature (blue/darkest $= -0.5$, red/brightest $= 0.5$); (b) Vertical velocity (blue/darkest $= -3.656 \times 10^{-3}$, red/brightest $= 4.182 \times 10^{-3}$).

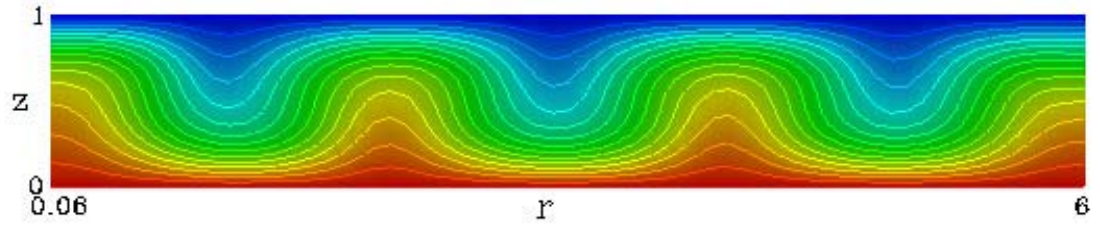

(a)

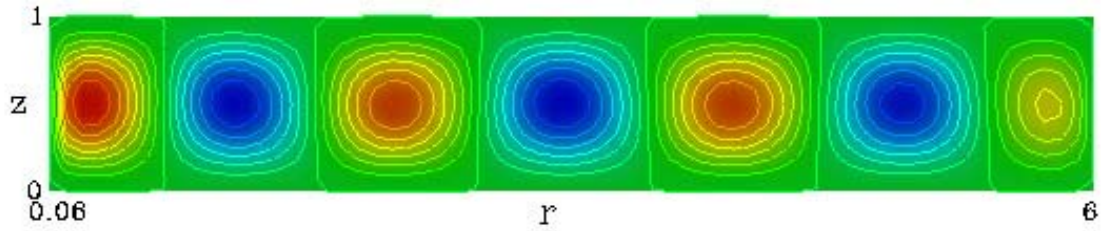

(b)

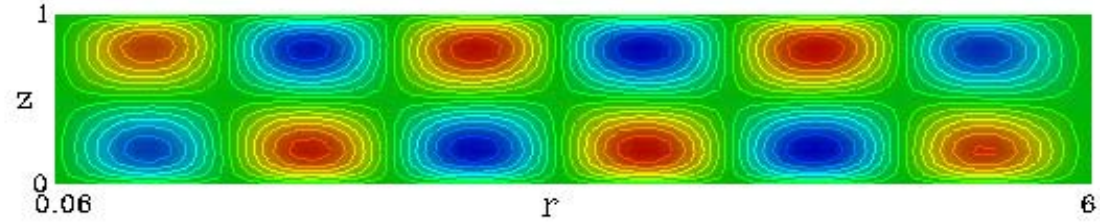

(c)

Figure 6.5: Temperature and velocity contours on $\theta = 0$. (a) Temperature (blue/darkest $= -0.5$,red/brightest $= 0.5$); (b) Vertical velocity (blue/darkest $= -3.656 \times 10^{-3}$, red/brightest $= 4.182 \times 10^{-3}$); (c) Radial velocity (blue/darkest $= -3.370 \times 10^{-3}$, red/brightest $= 3.402 \times 10^{-3}$).

center grid in $\theta = \pi$ section. In this case, the instability is initiated from the location of the disturbance, and it influences the solution in all the time steps. The same Rayleigh number and geometry ($Ra = 2800$) and geometry ($r_i = 0.06, r_o = 6$) were used as in case of Section 6.1, with a uniform grid of $64(r) \times 24(z) \times 72(\theta)$. Distorted rolls are formed instead of regular circular concentric rolls as one would expect, as shown in Figures 6.6 (a) and (b) which plot the contours of the temperature and vertical (axial) velocity in the middle z plane. The code with run with the same Rayleigh number (2800) and geometry as the above case. In Figure 6.6 (a) the blue (darkest) color represents the minimum temperature of -0.5 on the top surface and the red (brightest) color represents the maximum temperature of 0.5 on the bottom surface. In Figure 6.6 (b) the blue (darkest) color represents the maximum downward flow velocity of -4.4×10^{-3} and the red (brightest) color represents the maximum upward velocity of 5.0×10^{-3}. The concentricity and axisymmetricity of the convective rolls as seen in the previous case is destroyed by the initial disturbance. The location of the disturbance becomes a new center of the convection rolls, and the flow in the region away from the disturbance is adjusted accordingly.

Figures 6.7 (a), (b), (c), and (d) are the vertical velocity plots in several $\theta = 0$ sections. Figures 6.8 is the isometric view of the vertical velocity contour plot on three concentric surfaces along the radius with $r = 1.485$, 2.97 and 4.455, corresponding to $(r - r_i)/(r_o - r_i) = 1/4$, $1/2$ and $3/4$, respectively.

The solution with the distorted rolls instead of concentric rolls is difficult to explain theoretically as noted by Koschmieder [39]. Since the Rayleigh-Bénard is unstable

(a)

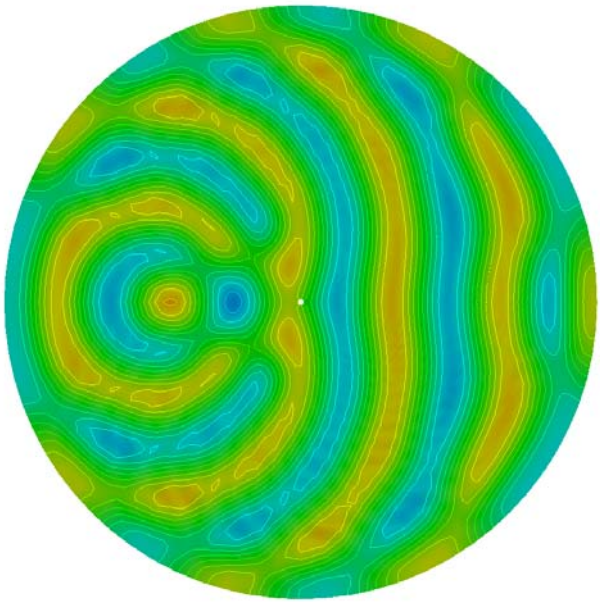

(b)

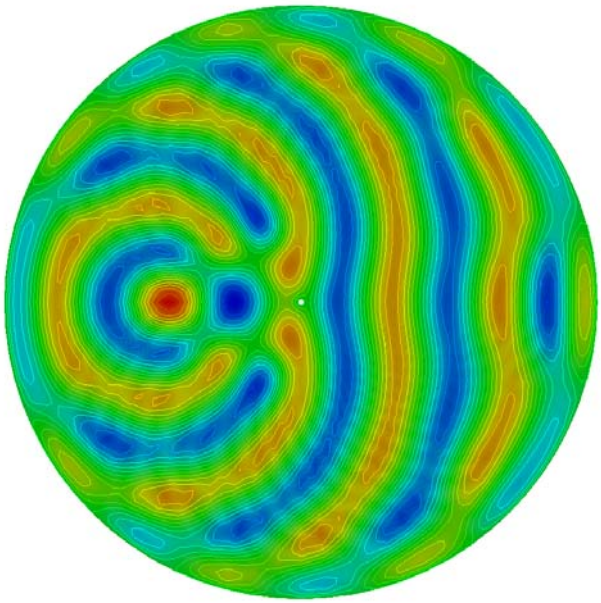

Figure 6.6: Temperature and velocity contours on $z = 0.5$. $Gr = 400$, $Pr = 7$, $r_o/H = 6$, $r_i/r_o = 0.01$. An initial temperature disturbance was applied at the center grid on $\theta = \pi$. (a) Temperature (blue/darkest $= -0.5$, red/brightest $= 0.5$); (b) Vertical (axial) velocity (blue/darkest $= -4.4 \times 10^{-3}$, red/brightest $= 5.0 \times 10^{-3}$).

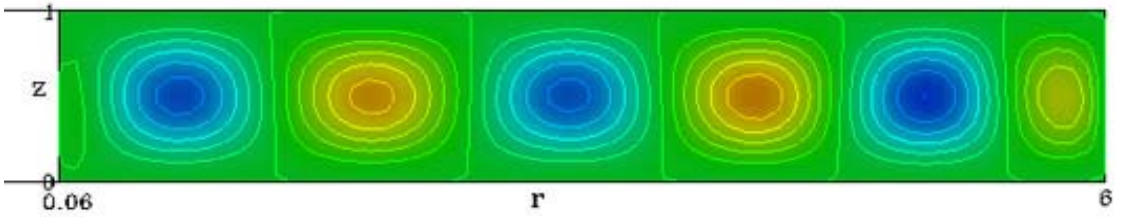

(a)

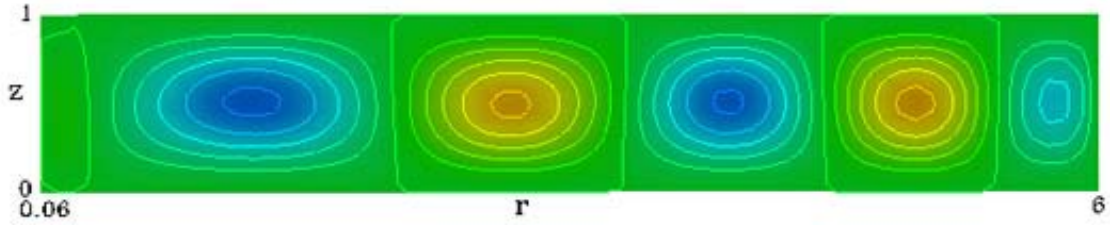

(b)

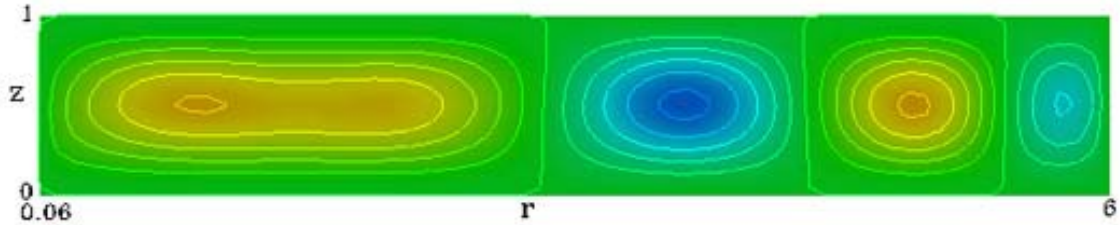

(c)

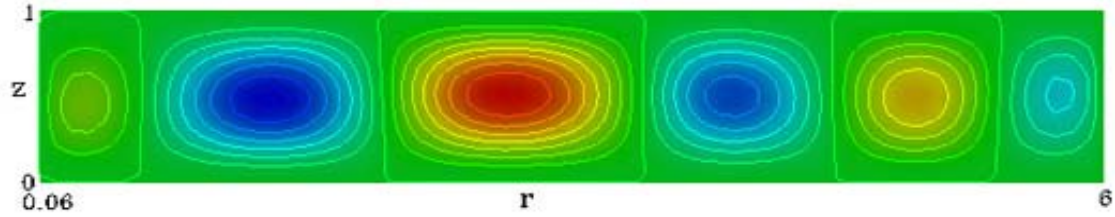

(d)

Figure 6.7: Vertical (axial) velocity contours on a several θ sections (blue/darkest $= -4.4 \times 10^{-3}$, red/brightest $= 5.0 \times 10^{-3}$). (a) $\theta = 0$, (a) $\theta = \pi/4$, (c) $\theta = \pi/2$, (d) $\theta = \pi$.

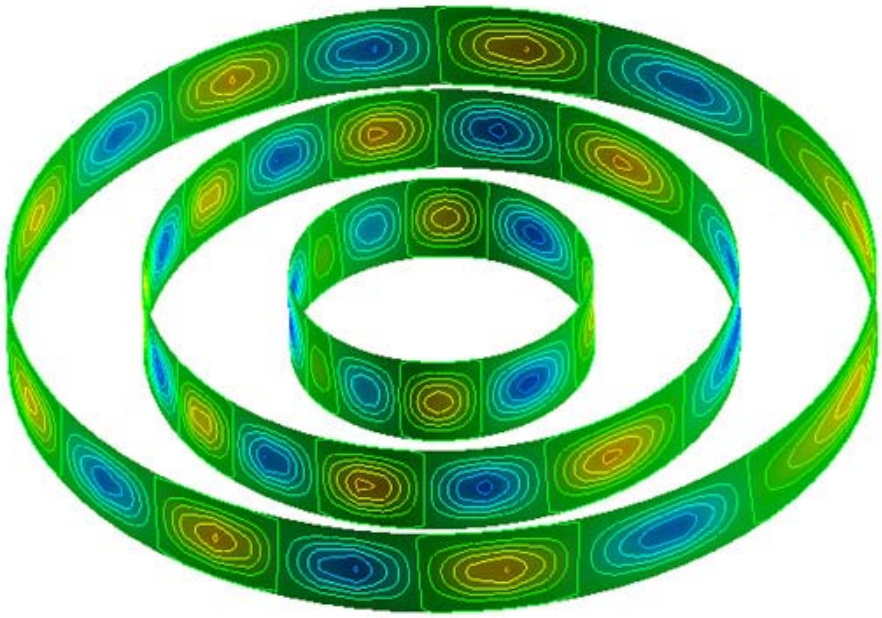

Figure 6.8: Vertical velocity contours on three surfaces along the radius: $r = 1.485$, 2.97 and 4.455 (blue/darkest $= -4.4 \times 10^{-3}$, red/brightest $= 5.0 \times 10^{-3}$). An initial temperature disturbance was applied at the center grid on $\theta = \pi$.

in nature, the flow is susceptible to imperfect bifurcation that leads solutions to different modes. In fact, similar patterns are also seen in experiments, contributed to non-uniformity of the device or in the temperature distribution. For the case of this study, the pattern is caused by the initial disturbance. As Ahlers et al. [4] and Koschmieder [39] noted, both the concentric rolls and distorted rolls are legitimate outcomes, and the pattern of parallel rolls is more an exception than a certainty, as commented by Croquette [22] [23] for the rectangular case. Actually, special cares are required to get concentric rolls, as Croquette [23] used a heating wire all the way along the inner cylinder to force concentric rolls. In a numerical solution, to prevent such distorted cells, disturbances at a single point have to be avoided. If initial disturbances are used, they have to be identical on the entire ring of 360 degrees.

6.3.2 Rayleigh-Bénard convection with non-uniform boundary condition

The axisymmetric rolls are also destroyed with non-uniform thermal boundary condition. To test this, the thermal boundary condition on the bottom plate was made to vary with θ as

$$T_0(r_i, \theta, z) = \bar{T}_0(1 + \varepsilon \sin n\theta) \tag{6.1}$$

The value $\varepsilon = 0.3$ and $n = 4$ are used in this problem. T_0 and $\bar{T}_0$ here are non-dimensional temperatures on the inner surface. Figures 6.9 (a) and (b) are the temperature and vertical (axial) velocity contours in the mid z plane. The same Rayleigh number ($Ra = 2800$) and geometry ($r_i = 0.06, r_o = 6$) were used as the case in Section 6.1 and 6.2 with a uniform grid of $64(r) \times 16(z) \times 48(\theta)$. The blue (darkest)

color represents the minimum temperature of -0.5 in Figure 6.9 (a) or the maximum downward flow velocity of -4.7×10^{-3} in Figure 6.9 (b), and the red (brightest) color represents the maximum temperature of 0.5 in Figure 6.9 (a) or the maximum upward flow velocity of 5.5×10^{-3} in Figure 6.9 (b). The circular stripes seen in the case with uniform boundary condition is destroyed owing to the non-uniform boundary condition. The widths of the four outer rolls vary with θ owing to the θ dependent boundary condition. The two rolls next to the innermost one are completely broken into two sets of cells, each set consisting of four cells. The outer four cells are for upward flow, and their shapes resemble triangles. The inner four cells are for downward flow, and their shapes are close to circles. The innermost roll is retained, but the shape changes to a square from the original circle.

Figures 6.10 (a) and (b) plot the contours of the temperature and vertical (axial) velocity in the $\theta = 0$ section. The representations of the colors are the same as these in Figure 6.9. The cell patterns are similar to those with the uniform boundary condition.

(a)

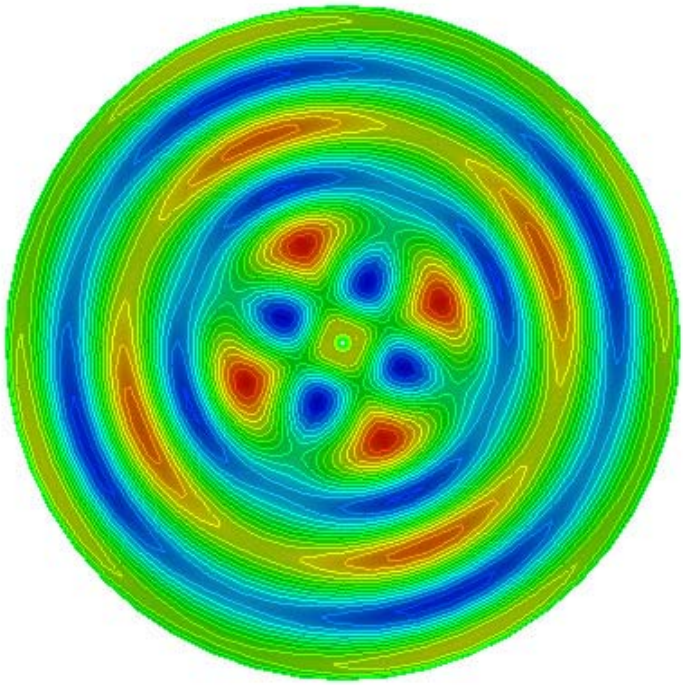

(b)

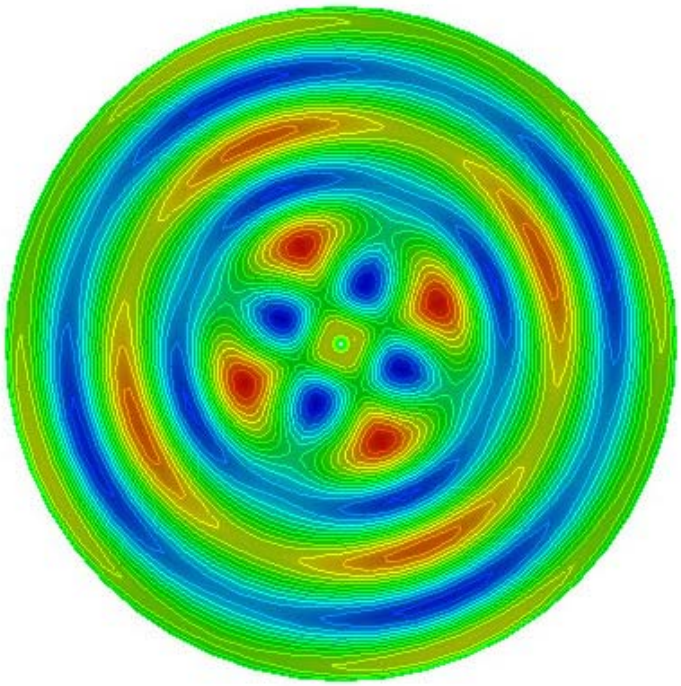

Figure 6.9: Temperature and velocity contours on $z = 0.5$. Non-uniform thermal boundary condition on the bottom surface. (a) Temperature (blue/darkest $= -0.5$, red/brightest $= 0.65$); (b) Vertical (axial) velocity (blue/darkest $= -4.7 \times 10^{-3}$, red/brightest $= -5.5 \times 10^{-3}$).

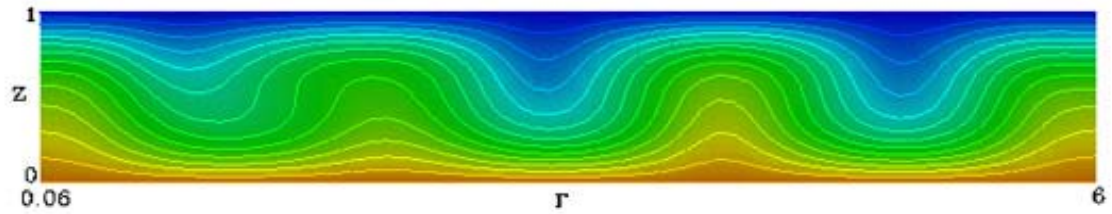

(a)

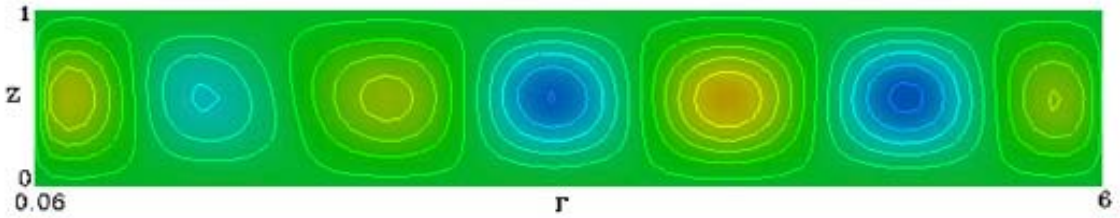

(b)

Figure 6.10: Temperature and velocity contours on $\theta = 0$. $Gr = 400$, $Pr = 7$, $r_i/H = 6$, $r_i/r_o = 0.01$. Non-uniform thermal boundary condition on the bottom surface. (a) Temperature (blue/darkest $= -0.5$, red/brightest $= 0.65$); (b) Vertical (axial) velocity (blue/darkest $= -4.7 \times 10^{-3}$, red/brightest $= -5.5 \times 10^{-3}$).

CHAPTER 7

TAYLOR-COUETTE FLOW

7.1 Introduction

Taylor-Couette flow is second most studied stability problem if Rayleigh-Bénard convection is the first. This problem was first investigated experimentally by Couette in 1890 and Mallock in 1896 (see [16], [39]). They observed that the torque needed to rotate the outer cylinder increased linearly with the rotation speed until a critical rotation speed is reached, after which the torque increased more rapidly. This change was due to a transition from stable to unstable flow at the critical rotation speed.

The stability of this type was first investigated by Lord Rayleigh in 1916 [58] (see [59]), who assumed that the fluid was non-viscous. He found that the flow becomes unstable when the azimuthal velocity v decreases with the radius, r, more strongly than $1/r$ [59].

The case of a viscous fluid was first investigated by Taylor in 1923 [65] (see [16], [39]), who made a direct comparison between a laboratory experiment and a prediction for the formation of a pattern at instability. He observed that the first disturbance

to arise was axisymmetric (independent of θ). The resultant Taylor vortices encircle the inner cylinder and are stacked in the axial direction. Taylor conducted careful experiments that agreed with his theory within a few percent for a wide range of parameters. He thus demonstrated that linear stability analysis can make quantitative predictions of patterns.

Chandrasekhar [16] summarized the early experimental and analytical work and gave detailed analytical formulation and solution. Since the 1960's the investigation of the nonlinear aspects of the Taylor vortex problem has dominated the field, and extensive experiments were performed to visualize different flow patterns using suspended aluminum particles. Among those, Coles [20] studied numerous states (each state defined by the number of Taylor cells and the number of azimuthal waves) and characterized the transitions into two distinct kinds - one called transition by spectral evolution when the inner cylinder has a larger rotation speed than the outer, and another called catastrophic transition when the outer cylinder spins faster than the inner. Based on Coles' observation that the flow states are path dependent, Andereck et al. [5] created a now widely quoted transition diagram of different flow regimes between independently rotating cylinders.

Numerical studies on the Taylor-Couette flow with primitive variables have been limited. One of the early numerical studies on Taylor-vortex flow was attributed to Meyer [43] (see [41]), who in 1966 carried out axisymmetric simulation, and then later extended it to three dimensional for Reynolds numbers just above the critical value for the wavy vortices [44], [45] (see [41]). Marcus in 1984 [41] developed

a pseudospectral initial-value method for calculating the equilibrium states and the transitions for non-axisymmetric time-dependent Taylor-Couette flows in a infinite long annulus with a narrow gap, and used the code to study the mechanisms that produce non-axisymmetric disturbances [42]. His studies led him to propose that the traveling azimuthal waves are a result of secondary instability caused by radial outflow motion among the Taylor vortices. The code was used in 1992 by Coughlin and Marcus [21] to demonstrate that periodic traveling waves become unstable to quasi-periodic modulated waves with increasing Reynolds numbers.

While most of the experimental and analytical studies focused on the flow with both cylinders rotating, either in the same direction or in the opposite directions, Koschmieder [39] commented that the instability can be studied clearly in the simple case of the inner cylinder rotating and the outer cylinder at rest. He stated that one can easily recognize four flow segments - axisymmetric Taylor vortex flow, wavy Taylor vortex flow, chaotic Taylor vortex flow, and turbulent vortex flow. Coles [20] observed as many as 20 or 25 different states at a given speed, and more than 70 transitions in the speed range up to 10 times the critical speed with the resting outer cylinder.

The stability of the Taylor-Couette flow is characterized by Taylor number (Ta), or Reynolds number (Re), both of which have been defined differently in the past. In this study, for the case with resting outer cylinder, the definition of Schlichting [59] is followed. It makes the Taylor number proportional to the Reynolds number (or

rotation speed Ω of the inner cylinder) rather than the square of the Reynolds number as defined by many others [16], [39],

$$Ta = \frac{\Omega r_i L}{\nu}\sqrt{\frac{L}{r_i}} \tag{7.1}$$

where $L = r_o - r_i$ is the gap width.

The critical Taylor number for flow to become unstable is 41.3 with this definition for an indefinitely tall narrow annulus. The length scale used to define Reynolds number is usually either the gap size [59], or the inner radius [20].

7.2 Taylor vortex flow

The Couette flow presented in the earlier chapter on code validation is a stable flow with $Ta = 28$, which is below the critical value ($Ta = 41.3$). Although there is a stable vortex near each of the two ends, those vortices do not propagate to the central region. The flow field in the central region remains axisymmetric and contains the azimuthal component only, without the radial or axial component.

If Taylor number exceeds the critical number of 41.3, the disturbances or the vortices from the ends propagate to the central region due to Taylor instability [20]. The numerical code developed in this dissertation was run with a $Ta = 56$ in an annulus of inner radius 0.84, outer radius 1 and height unity with a uniform grid $16()r \times 128(z) \times 144(\theta)$. Figures 7.1 (a), (b), and (c) are the contour plots of azimuthal, radial, and axial (vertical) velocities. The blue (darkest) color represents

the maximum inward flow velocity of -0.0574 in Figure 7.1 (a), the maximum downward flow velocity of -0.0808 in Figure 7.1 (b), or the minimum azimuthal velocity of 0 on the outer cylinder in Figure 7.1 (c). The red (brightest) color represents the maximum outward flow velocity of 0.0808 in Figure 7.1 (a), the maximum downward flow velocity of 0.0961 in Figure 7.1 (b), or the maximum azimuthal velocity of 1 on the inner cylinder in Figure 7.1 (c). A series of toroidal rolls are formed inside the gap encircling the inner cylinder. They are periodic in axial direction with the axes in azimuthal direction parallel to the base flow. At steady state, there are six stationary rolls of equal size and intensity inside the annulus, each roll rotating in the opposite direction with the adjacent rolls. The average wave length is 2.08, and this is very close to critical value of 2.016 obtained by theoretical modal analysis [16] for an infinite long narrow annulus.

Figure 7.2 plots the radial velocity on the middle surface, to show the isometric view of the ring structure. The colors representations are the same as these in Figure 7.1 (a). The outward and inward flows in the radial direction are easily visualized in the experiments [20], [5], [39].

Transient development of Taylor vortices

The transient development of axisymmetric Taylor vortex flow for $Ta = 56$ was studied by the two-dimensional axisymmetric code. The code was run on in an annulus of inner radius 0.84, outer radius 1 and height unity with a uniform grid $32(r) \times 128(z)$ and a time step 0.001. Figures 7.3 (a), (b), (c) and (d) plot the streamlines for selected solutions at different time steps. The colors represent the radial velocity with blue (darkest) color representing the maximum inward flow velocity and red (brightest)

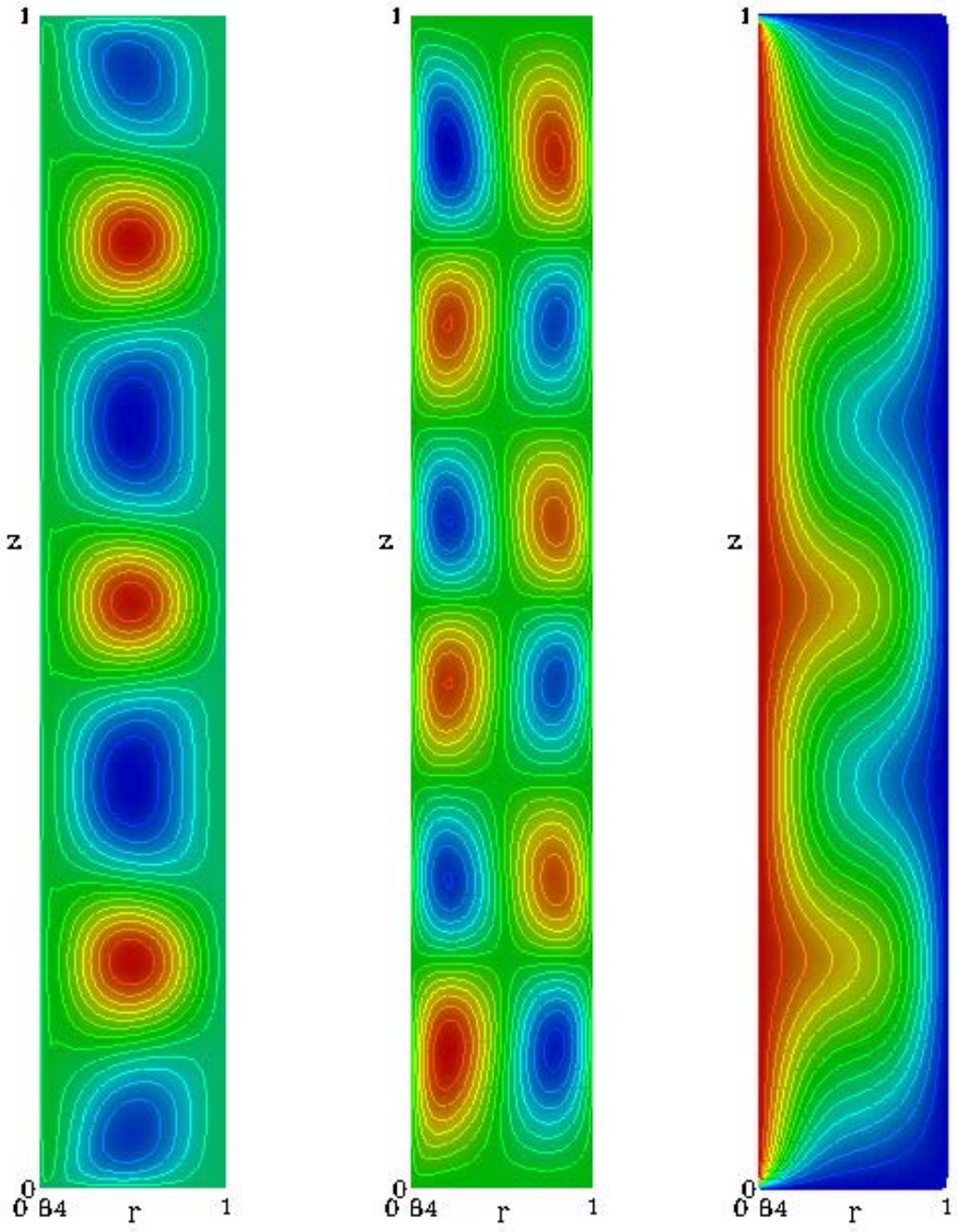

(a) (b) (c)

Figure 7.1: Velocity contours of Taylor vortex flow. $Ta = 56$, $r_i/r_o = 0.84$, $r_o/H = 1$. (a) Radial velocity (blue/darkest $= -0.0574$, red/brightest $= 0.0961$); (b) Axial (vertical) velocity (blue/darkest $= -0.0808$, red/brightest $= 0.0808$); (c) Azimuthal velocity (blue/darkest $= 0$, red/brightest $= 1$).

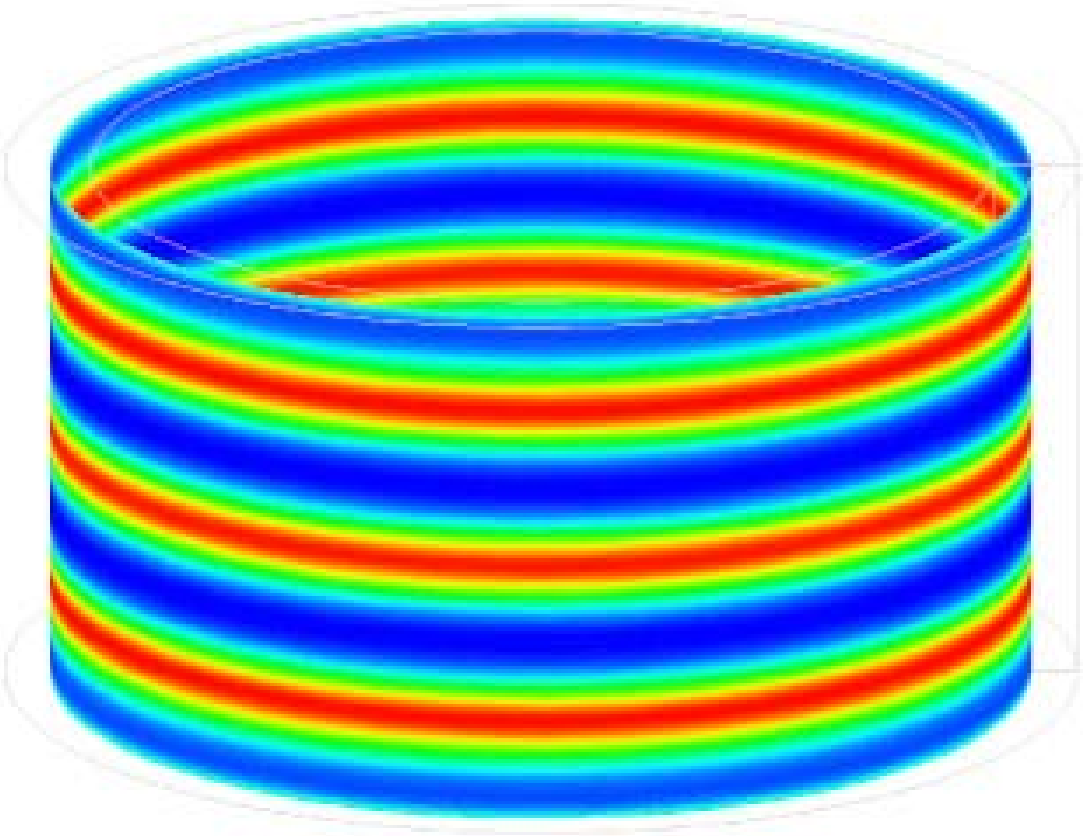

Figure 7.2: Isometric view of radial velocity contours in the middle of the gap. $Ta = 56$, $r_i/r_o = 0.84$, $r_o/H = 1$. (blue/darkest $= -0.0574$, red/brightest $= 0.0961$).

color representing the maximum outward flow. At first, the flow is quickly developed to circular Couette flow from rest, and a initial vortex cell is developed from each of the two ends due to the end effect (Fig. 7.3 (a)). After the cells grow to the full size and intensity, they propagate toward the central region and form the second pair of cells (Fig. 7.3 (b)). After they gain size and intensity, the third pair of the cells begins to form (Fig. 7.3 (c)). Eventually, the entire gap is filled with cells of equal size and intensity (Fig. 7.3 (d)).

The transient development of the velocity can also be demonstrated by the time history of the velocity components (Fig. 7.4) and their norms (Fig. 7.5). The flow in certain locations may reverse its direction during the development. The flow is fully developed abound non-dimensional time 25.

7.3 Wavy vortex flow

With a height to gap aspect ratio equal to 19.2 and $Ta = 121$ which is about 3 times of the critical Taylor number, flow becomes non-axisymmetric, and the flow pattern becomes a wavy vortex flow. The case was run in an annulus of inner radius 0.448, outer radius 0.5 and height unity with a uniform grid $16(r) \times 128(z) \times 76(\theta)$. Figure 7.6 is the contour plot of the radial velocity on the middle gap surface, in which the blue (darkest) color represents the maximum inward flow velocity of -0.171 and the red (brightest) color represents the maximum outward flow velocity of 0.184. Figures 7.7 (a) and (b) are the contour plots of vertical and azimuthal velocities on the middle gap surface, in which the blue (darkest) color represents the maximum inward radial velocity of -0.245 in Figure 7.7 (a) or the minimum azimuthal velocity of 0 on the

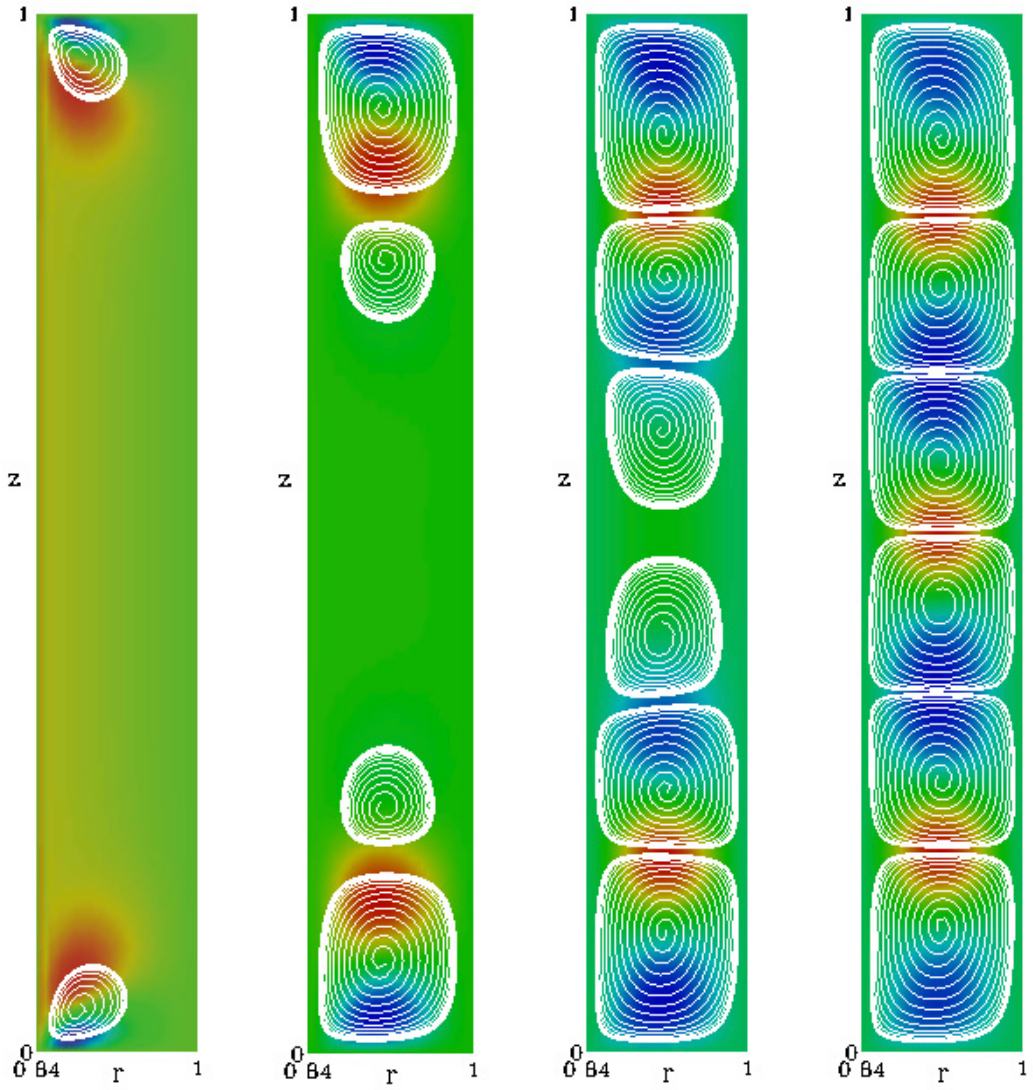

Figure 7.3: Streamlines at different time steps. (a) (non-dimensional) time = 1, cells start to form from the ends; (b) time = 5, second groups of cells starts to form; (c) time = 10, the inner cells start to form; (d) time = 20. close to fully developed cells.

(a)

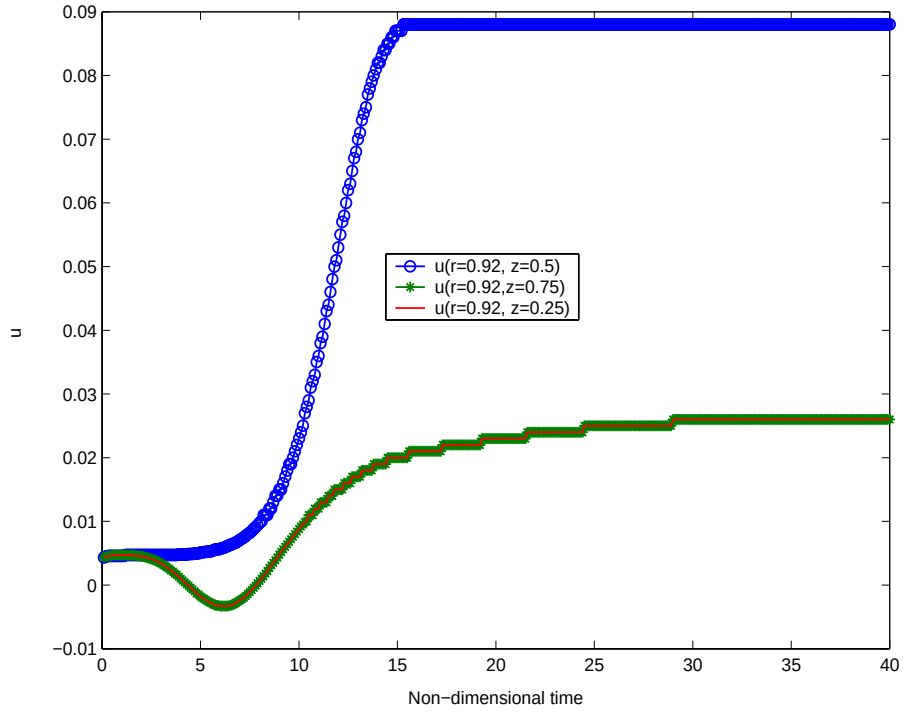

(b)

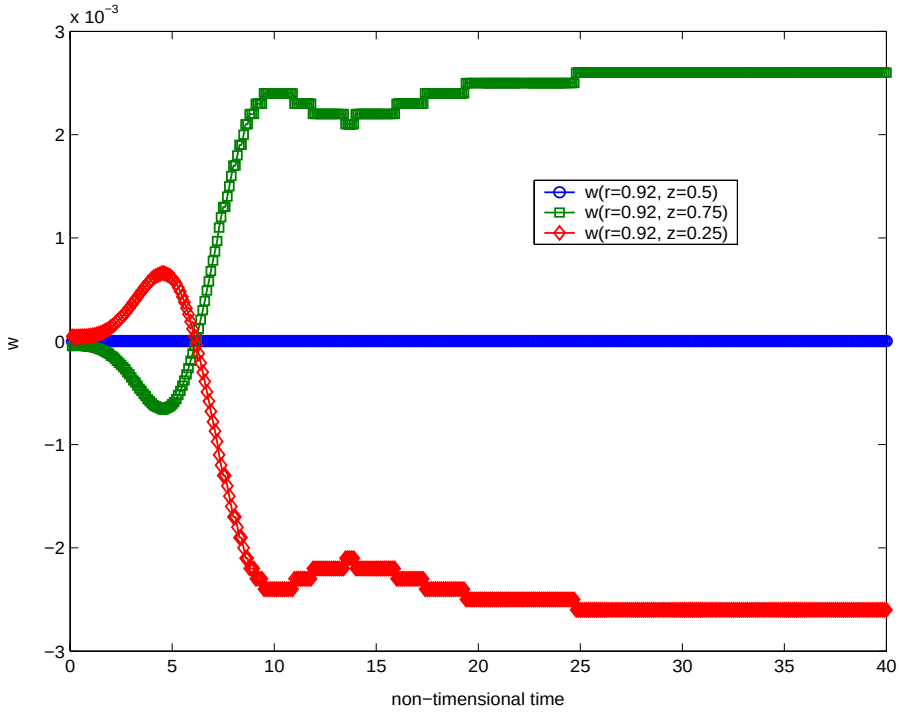

Figure 7.4: Radial and axial velocities variy with non-dimensional time on three points inside the gap. (a) Radial velocity, (b) Vertical (axial) velocity.

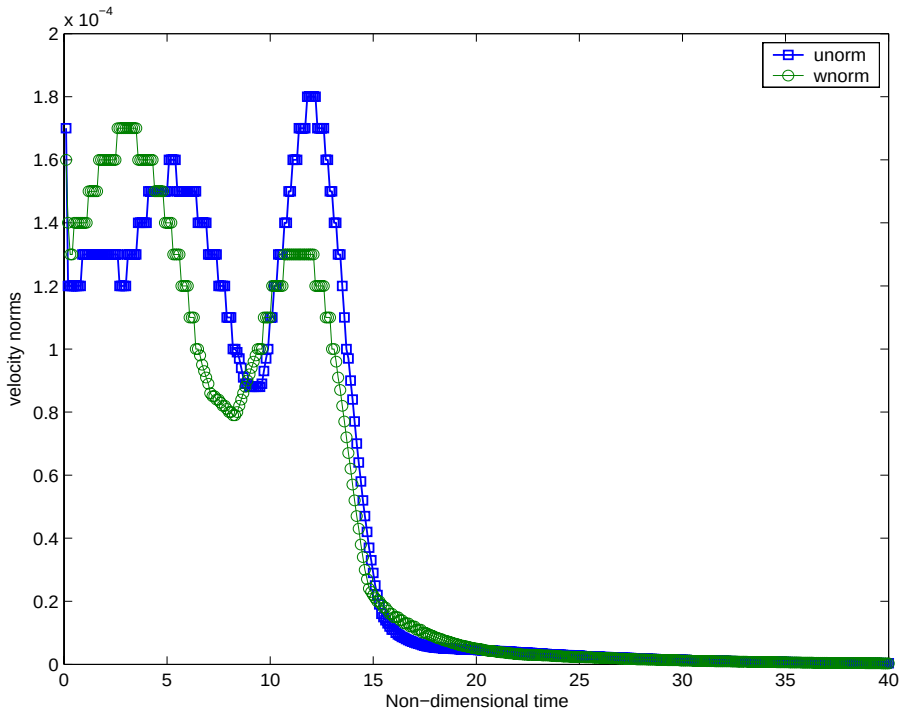

Figure 7.5: The velocity norms vary with non-dimensional time.

outer surface in Figure 7.7 (b), and the red (brightest) color represents the maximum outward radial velocity of 0.229 in (a) or the maximum azimuthal velocity of 1.01 (b). The wavy shapes of the Taylor vortices around the cylinder are easily recognized from these plots, similar to the pictures seen in the experiments [20], [5], [39].

Figures 7.8 (a), (b), and (c) plot the radial velocity contours, vertical (axial) velocity contours, and azimuthal velocity contours on $\theta = 0$ section. The Taylor cells are distorted compared to the normal cells with Taylor number just above the critical value (Figures 7.1 (a) - (c)). There are 8 cells in the axial direction, and the wave length in the z direction is 2.5, which is close to the value of 2.6 given by Koschmiemder [39] in a much taller annulus ($H/L = 122$). The wave number in θ direction is 8, compared with 6 in Koschmieder's experiment [39]. The differences may be caused by the difference in aspect ratio (20 in numerical study and 122 in experiment) and the difference in accelerating the inner cylinder (the speed of inner cylinder increases very slowly in the experiment [39], but the inner cylinder speed increases suddenly as a step function in this numerical study).

It has been well noticed that the wavelength for supercritical Taylor vortex flow is not unique for a given Taylor number. Koschmieder [39] showed that it varies from $\lambda_z = 1.53$ for a case of a sudden start of inner cylinder rotation, to 2.02 for the case by a quasi-steady increase, and 2.405 if the annulus is filled after the inner cylinder rotates with the full speed. Actually, in general there exists a discrete spectrum of allowable axial wavelength and azimuthal wave numbers [20], [42], [39]. Marcus concluded based on his numerical studies that Taylor vortex flow is stable with final

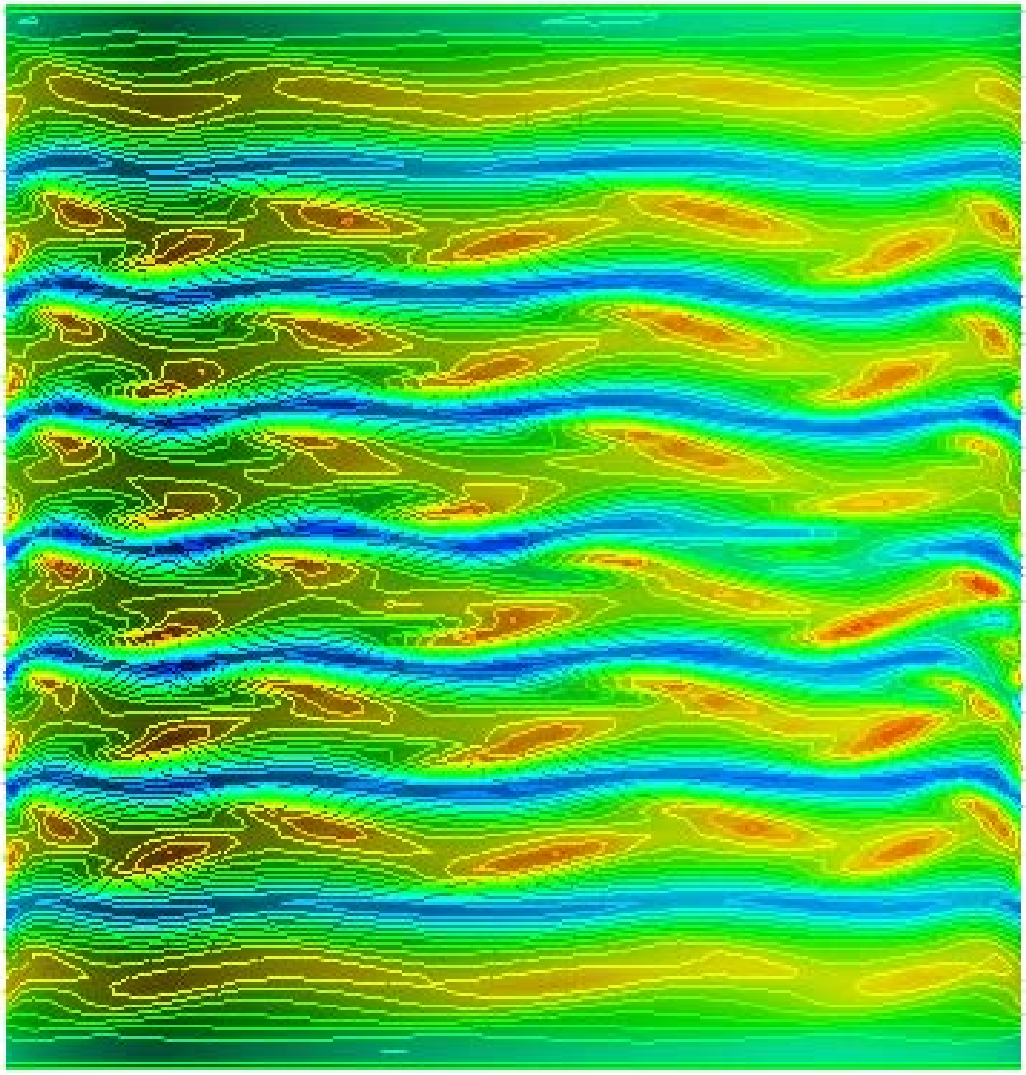

Figure 7.6: Radial velocity contours in the mid gap at (non-dimensional) time 100 (blue/darkest $= -0.171$, red/brightest $= 0.184$).

(a)

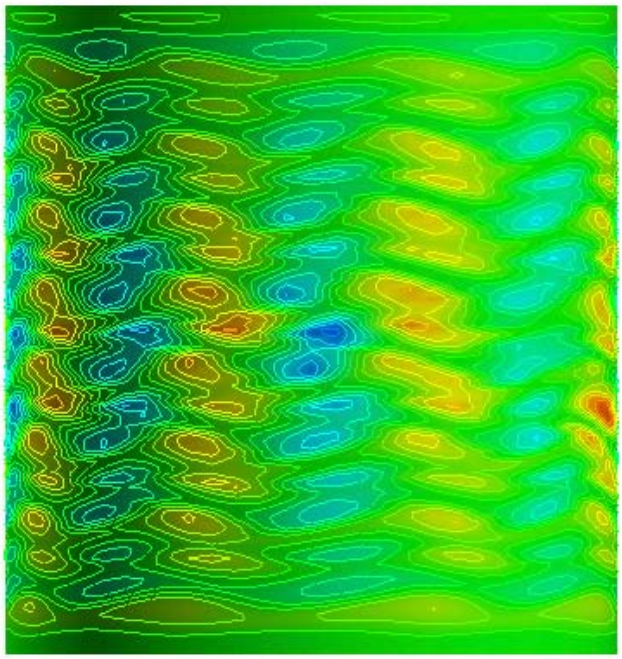

(b)

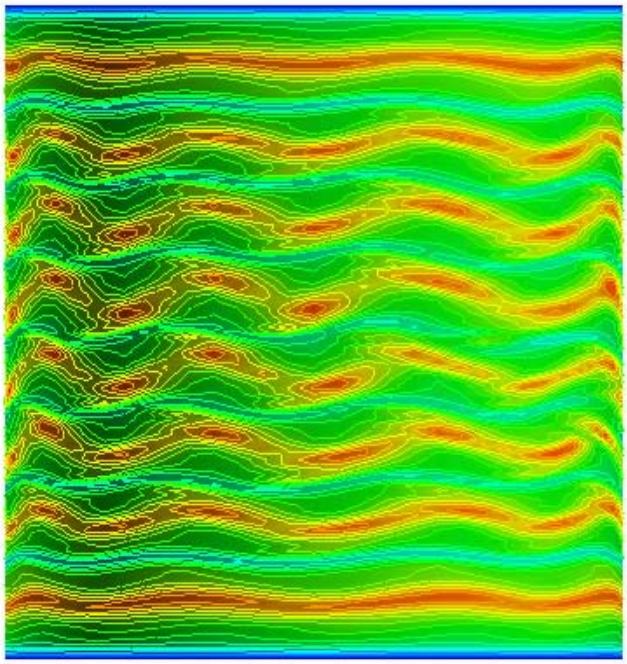

Figure 7.7: Velocity contours in the mid gap at (non-dimensional) time 100. (a) Vertical velocity (blue/darkest = -0.245, red/brightest = 0.229), (b) Azimuthal velocity (blue/darkest = 0, red/brightest = 1.01).

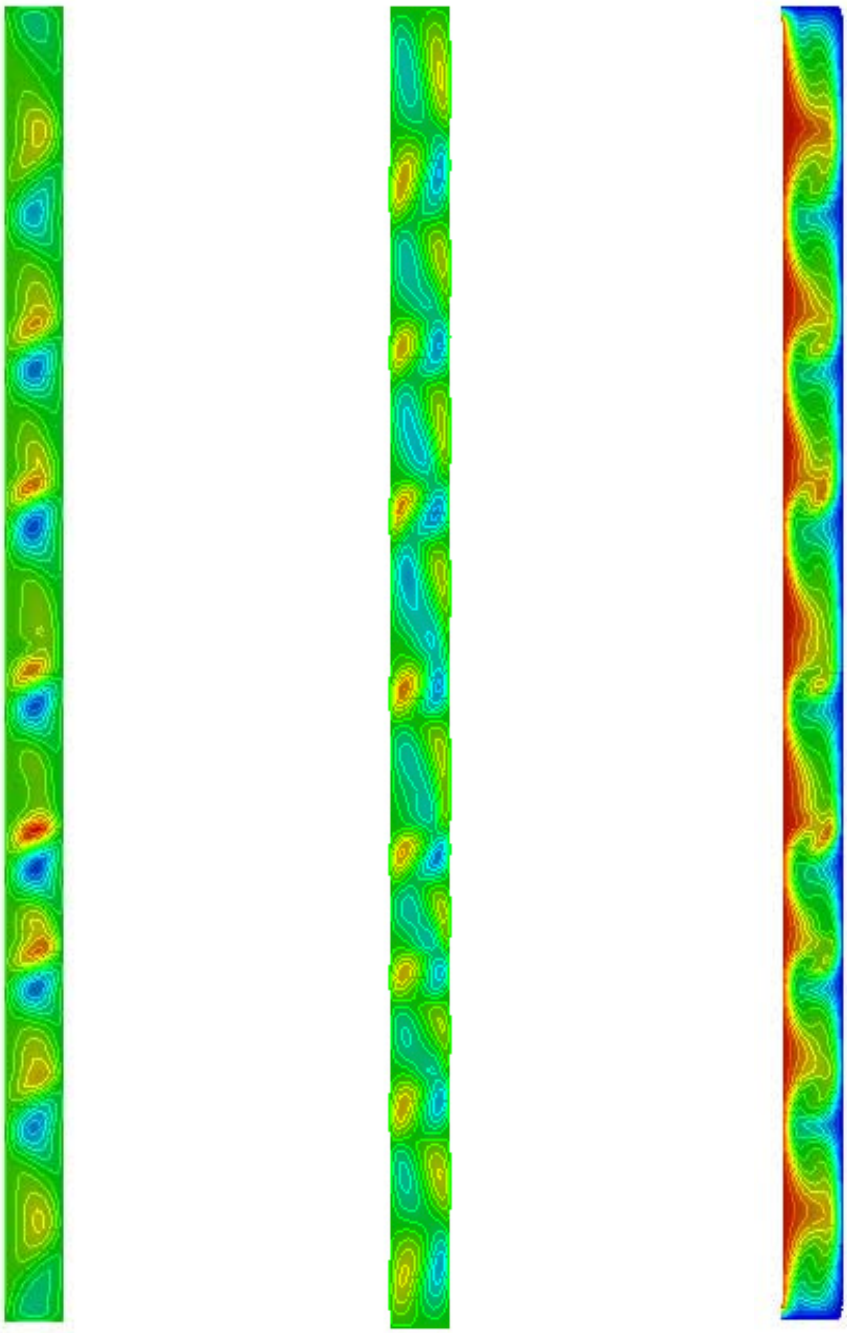

(a) (b) (c)

Figure 7.8: Velocity contours on $\theta = 0$ at (non-dimensional) time 100. (a) Radial velocity (blue/darkest $= -0.171$, red/brightest $= 0.184$), (b) Vertical (axial) velocity (blue/darkest $= -0.245$, red/brightest $= 0.229$), (c) Azimuthal velocity (blue/darkest $= 0$, red/brightest $= 1.01$).

steady state independent of the initial conditions only in a stable region when the Reylaigh number is slightly higher than the critical value [42].

The wavy Taylor vortex has been observed by experiments with large Taylor number and tall thin annuli [20], [31], and [39]. Koschimier's experiment [39] is produced here numerically, with a similar Taylor number but a smaller height to gap aspect ratio (19.2 verse 122 in [39]. The numerical results show that the flow first starts with circular Couette flow (not shown), then develops into Taylor vortex flow (Fig. 7.9 (a)) (wave length $\lambda_z = 1.8$) around non-dimensional time 10. A wavy vortex flow is then initiated from each of the two ends (10 waves in each vortex) around non-dimensional time 30, and propagates into the center region (Fig. 7.9 (b)). The two wavy vortices then merge in the middle around non-dimensional time 60 with increased wave length in axial direction (8 full waves with $\lambda_z = 2.5$) and reduced wave number in azimuthal direction (8 waves), as shown in Figure 7.6.

The flow is time-dependent and oscillatory, as shown in Figure 7.10 (a) which plots the time variation of the three velocity components at the center grid point ($r = 0.475$ or $r = (r_i + r_o)/2$, $z = 0.5$, and $\theta = \pi$), and Figure 7.10 (b) which plots the time variation of their norms (the absolute values of the velocity changes between the two immediate time steps).

The sequence of the wavy vortex flow development observed in this study matches the explanation by Marcus [42] who used a numerical simulation to demonstrate that energy is transferred from the motor that drives the inner cylinder to the circular

(a)

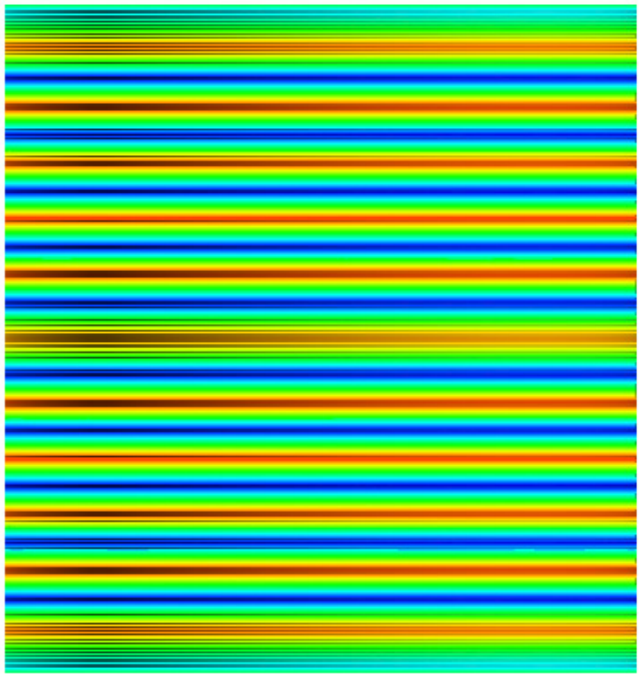

(b)

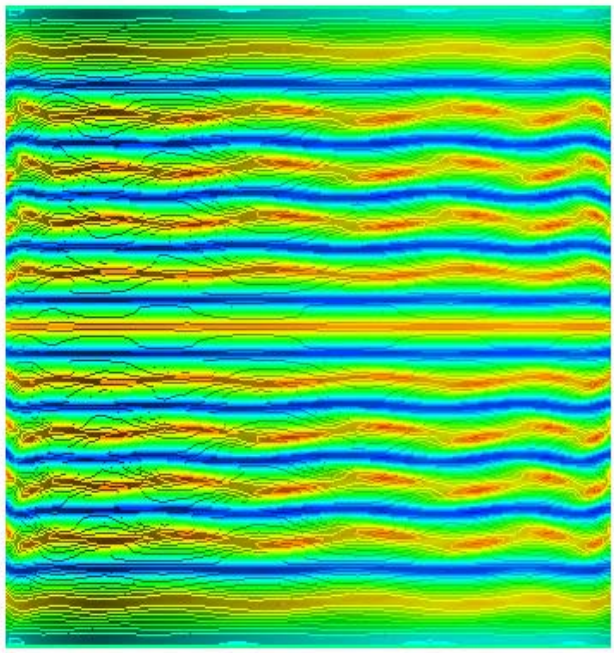

Figure 7.9: Radial velocity contours on the mid gap at (non-dimensional) time 10 and 50. (a) $time = 10$ (blue/darkest $= -0.124$, red/brightest $= 0.162$), (b) $time = 50$ (blue/darkest $= -0.142$, red/brightest $= 0.189$).

(a)

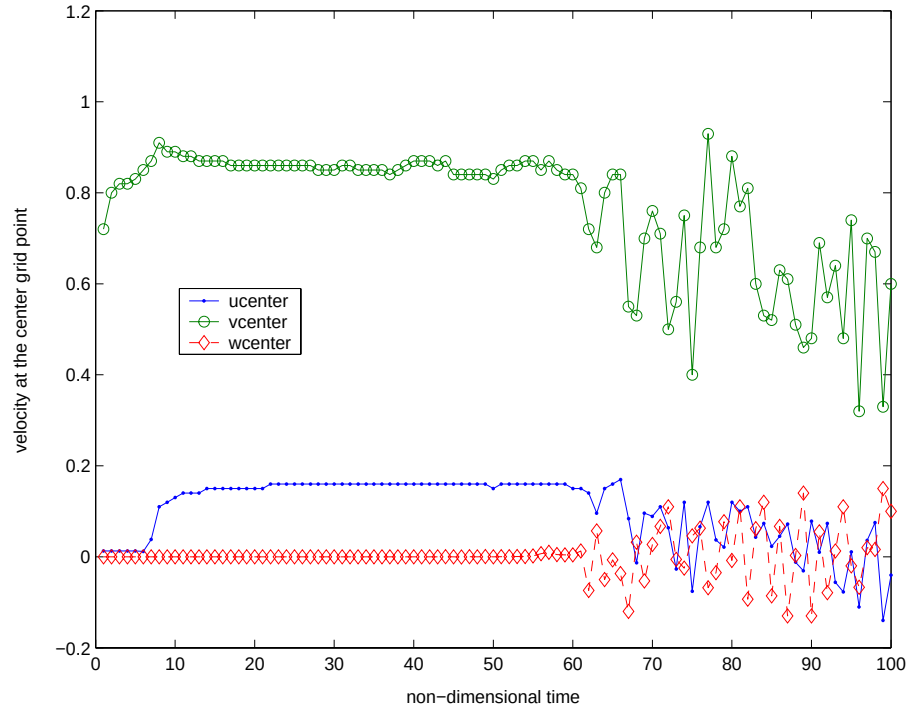

(b)

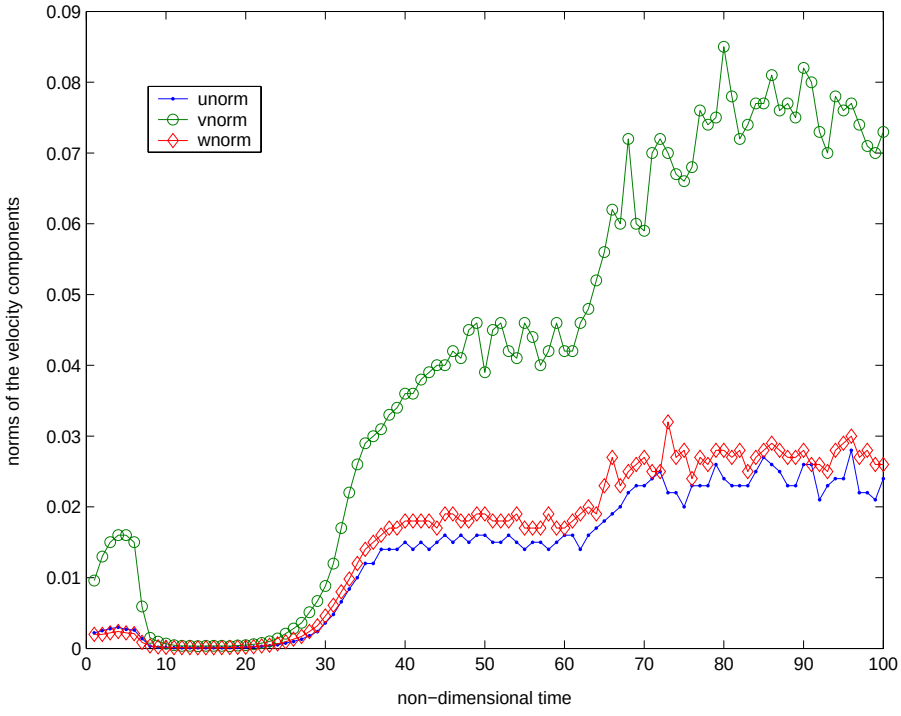

Figure 7.10: (a) Time variation of the velocity components on the center grid point ($r = 0.475$, $z = 0.5$, $\theta = \pi$). (b) Time variation of the three velocity norms.

Couette flow, to the axisymmetric Taylor-vortex flow, and then is distributed among the modes that make up the wavy-vortex flow.

At high Rayleigh numbers, the flow becomes time-dependent and complex with numerous states and transitions as observed by Coles [20]. The numerical study here is all based on a case of rotating inner cylinder and resting outer cylinder with a sudden start from the rest. It is considered exploratory to demonstrate the code's ability to solve three-dimensional flow in axisymmetric geometries with uniform boundary and initial conditions.

CHAPTER 8

CONCLUSION AND DISCUSSION

Pressure Poisson equation with Neumann boundary conditions results in a singular matrix for the difference equations. The solutions are not unique for it is additive to a constant. A fast direct inversion method developed in this dissertation to solve the Poisson equation in cylindrical coordinates has been found to be a fast and accurate. The coefficient matrix is first transformed to a symmetric matrix by a series of elementary operations, simultaneously with the source term of the difference equations. The generalized eigenvalues and eigenvectors solved from a smallest sub-matrix are used to attain the pressure through two levels of matrix inversions. The computer code was verified with analytical solution of a simple source term. Unlike in Cartesian coordinates in which there is no preference on the order of matrix inversions, in cylindrical coordinates the order of matrix inversions is important. The inner most matrix needs to be formed from θ level discretization and the outer most matrix is from r level discretization, and the z level is in between.

The method was used to solve incompressible Navier-Stokes equations in three-dimensional coordinates in primitive variables. The analytical known problems - flow in an annulus with the rotating inner cylinder (Couette flow), and free convection in a tall

narrow annulus - were used to validate the code. The more complicated flow in a lid-driven cavity was also used for validation and the results were compared with the data published in the literature. The code was then used to study different flow problems, including thermocapillary convection in an annulus, free convection in a shallow annulus heated from below (Rayleigh-Bénard convection), and flow in an annulus with a rotating inner cylinder (Taylor-Couette flow).

In the thermocapillary convection in an annulus with heated inner cylinder, the free surface was assumed to be flat as a first order approximation. The resulting flow is two-dimensional axisymmetric without azimuthal component, and a single vortex is formed below the free surface. The flow becomes three-dimensional (with all u, v, w components) and non-axisymmetric when a θ dependent temperature boundary condition is applied on the inner cylinder. However, although the three-dimensionality and non-axisymmtricity are seen everywhere in the flow domain, they become weaker away from the inner cylinder and free surface.

Numerical solution of natural convection in a shallow annular disk heated from the bottom (Rayleigh-Bénard convection) results in two-dimensional axisymmetric flow without azimuthal component when the Rayleigh number is above its critical value. A layer of rolls with azimuthal axes are formed inside the vertical gap encircling the inner cylinder. The number of rolls in the radial direction depends on Rayleigh number and the height to radial gap ratio. The axisymmetricity of the flow and the shape of the rolls are sensitive to initial and boundary conditions. The concentric rolls can be distorted by an initial temperature disturbance in a single grid point. With variable

temperature distribution on the bottom surface, the flow becomes three-dimensional and non-axisymmetric.

Numerical solution of flow in an annulus with a rotating inner cylinder (Taylor-Couette flow) results in r dependent flow away from the ends when the Taylor number is below a critical instability value. When the Taylor number exceeds the critical value, a series of toroidal rolls encircling the inner cylinder are developed between the cylinders and are stacked in the axial direction (Taylor vortex flow). As Taylor number further increases with sufficient height / gap ratio, azimuthal waves are formed and superimposed on the Taylor vortices (wavy vortex flow).

The numerical method is first order in time and second order in space in both solving the pressure Poisson equation and the momentum equation. Although the implicit method used in this study is second order in time, the linearization of the convective terms reduced the accuracy to first order.

The numerical algorithm and code developed in this dissertation has proven to be accurate and effective in studying thermal convection and fluid flow inside an annulus. This code will be a helpful tool in studying flow patterns and transitions observed in numerous experiments in Rayleigh-Bénard convection, Taylor-Couette flow, and other flows in annular geometries.

APPENDIX A

FREE SURFACE DEFLECTION

A.1 Overview

Although the formulation in the previous sections focuses mainly on the simplified case that assumes the geometry of the free surface is fixed and flat, it is also valid for the general free surface that is deflected and time dependent. In general, the shape of the surface is a function of r- and θ-coordinates, and the surface shape changes with time as the flow develops.

The way in which the free surface deforms has been worked on by many researchers. Orr and Scriven [48] gave a detailed introduction for the free surface problem of steady rimming flow in an infinitely long cylinder and discussed methods for solving the problem. Silliman and Scriven [61] determined the free surface shape for a steady two-dimensional discharge of liquid from a sharp-edged slot by the Galerkin finite element method. Sen and Davis [60], by expanding variables, including the surface height, in series of aspect ratios in a two-dimensional shallow slot, obtained the surface shape in addition to the fluid and thermal fields. Zebib et al. [67] expanded the surface height in a series for a small capillary number and then solved the

leading-order surface deflection numerically. Keunings [35] developed an algorithm to solve a transient problem of an isothermal flow by using a Galerkin finite element technique. Cuvelier and Driessen studied two-dimensional thermocapillary flows with a free boundary in the context of crystal growth. They investigated the influence of some parameters on the shape of the free boundary. Babu [8], following the method of Zebib et al. [67], formulated the equation for the leading-order surface deflection for a free surface in two-dimensional rectangular coordinates.

Reconsider the problem described in the early section. Initially, the flow is assumed to be motionless with a flat, free surface of height H. The gas above the free surface is assumed to be inviscid and massless and to have a constant temperature T_2. The thermocapillarity effect owing to the variation of temperature on the surface introduces a thermocapillary stress, which in turn causes fluid motion. The existence of capillarity on the free surface causes the free surface to depart from flatness.

The governing equations and the boundary conditions are the same as those in the early sections, except on the free surface. One additional unknown h is introduced for the new problem. Unlike the field variables (u, v, w, T, and p), h is a function of radius (r), angle (θ), and time (t) only, and does not depend on fluid depth z. That is, it appears in the boundary condition only.

A.2 Formulation

A.2.1 Kinematic condition

Let the free surface be given by

$$F(r,\theta,z,t) \equiv z - (1 + h(r,\theta,t)) = 0 \tag{A.1}$$

The time derivative of this yields the kinematic condition on the free surface

$$w = \frac{\partial h}{\partial t} + uh_r + v\frac{h_\theta}{r} \tag{A.2}$$

where h_r denotes $\frac{\partial h}{\partial r}$, and h_θ denotes $\frac{\partial h}{\partial \theta}$.

At steady state the flow normal to the surface vanishes, and the condition is simplified to

$$\mathbf{n} \cdot \mathbf{v} = 0 \tag{A.3}$$

where $\mathbf{n}$ is the unit vector normal to the surface

$$\mathbf{n} = -\frac{1}{N}\left(h_r \mathbf{e_r} + \frac{h_\theta}{r}\mathbf{e}_\theta + \mathbf{e_z}\right) \tag{A.4}$$

where $N = (1 + h_r^2 + \frac{1}{r^2}h_\theta^2)^{1/2}$

A.2.2 Dynamic conditions

The normal viscous stress on the free surface is balanced by gas pressure and capillary pressure. That is

$$\sigma_n \equiv \sigma_{ij} n_j n_i = 2\kappa\sigma_s - p_a \tag{A.5}$$

where κ is the mean curvature of the free surface.

The thermocapillary stress for the tangential components is

$$\sigma_{t_\ell} \equiv \sigma_{ij} n_j t_{i,\ell} = -\gamma \frac{\partial T}{\partial s_\ell} \tag{A.6}$$

where $\ell = 1, 2$, corresponding to two independent components on the tangent plane. In these equations σ_{ij} are the components of the stress tensor of the liquid

$$\sigma_{ij} = -p\delta_{ij} + 2\tau_{ij} \tag{A.7}$$

where δ_{ij} is Kronecker delta. The stress vector on the free surface is given by

$$\begin{aligned} \sigma = -p\ \mathbf{n} - \frac{1}{N} \Bigg[& \left(h_r \tau_{rr} + \frac{h_\theta}{r} \tau_{\theta r} - \tau_{zr} \right) \mathbf{e_r} \\ & + \left(h_r \tau_{r\theta} + \frac{h_\theta}{r} \tau_{\theta\theta} - \tau_{z\theta} \right) \mathbf{e}_\theta + \left(h_r \tau_{rz} + \frac{h_\theta}{r} \tau_{\theta z} - \tau_{zz} \right) \mathbf{e_z} \Bigg] \end{aligned} \tag{A.8}$$

The viscous stresses in cylindrical coordinates are given by

$$\begin{aligned} \tau_{rr} &= 2\mu \frac{\partial u}{\partial r} & \tau_{r\theta} &= \tau_{\theta r} = \mu \left[\frac{1}{r} \frac{\partial u}{\partial \theta} + r \frac{\partial}{\partial r} \left(\frac{v}{r} \right) \right] \\ \tau_{\theta\theta} &= 2\mu \left(\frac{1}{r} \frac{\partial v}{\partial \theta} + \frac{u}{r} \right) & \tau_{\theta z} &= \tau_{z\theta} = \mu \left(\frac{\partial v}{\partial z} + \frac{1}{r} \frac{\partial w}{\partial \theta} \right) \\ \tau_{zz} &= 2\mu \frac{\partial w}{\partial z} & \tau_{zr} &= \tau_{rz} = \mu \left(\frac{\partial w}{\partial r} + \frac{\partial u}{\partial z} \right) \end{aligned} \tag{A.9}$$

The left-hand side of the normal stress balance (A.5) is the normal component of the stress vector. According to (A.4) and (A.9) it is given by

$$\sigma_n = -p - \frac{1}{N^2}\left(h_r^2\tau_{rr} + \frac{h_\theta^2}{r^2}\tau_{\theta\theta} + \tau_{zz} + \frac{2h_r h_\theta}{r}\tau_{\theta r} - \frac{2h_\theta}{r}\tau_{z\theta} - 2h_r\tau_{rz}\right) \qquad \text{(A.10)}$$

The mean curvature κ is

$$2\kappa = \frac{1}{N^3}\left[(1+h_r^2)\frac{h_{\theta\theta}}{r^2} + \left(1+\frac{h_\theta^2}{r^2}\right)h_{rr} + (1+h_r^2)\frac{h_r}{r} + \frac{2h_r h_\theta}{r^2}\left(\frac{h_\theta}{r} - h_{r\theta}\right)\right] \qquad \text{(A.11)}$$

Substituting (A.11) and (A.9) into (A.5) yields the dynamic condition in the normal direction. This can be put into dimensionless form by introducing the surface tension $\sigma_s' = \sigma_s/\sigma_s^0$ and capillary number $C_a = \mu U_R/\sigma_s^0$. The non-dimensional form of the normal stress balance after dropping the primes is then

$$\begin{aligned} &-\frac{\sigma_s}{2C_a\ N}\left[(1+h_r^2)\frac{h_{\theta\theta}}{r^2} + \left(1+\frac{h_\theta^2}{r^2}\right)h_{rr} + (1+h_r^2)\frac{h_r}{r} + \frac{2h_r h_\theta}{r^2}\left(\frac{h_\theta}{r} - h_{r\theta}\right)\right] \\ &\quad -\frac{1}{2}R_e\ N^2\ p = h_r^2\frac{\partial u}{\partial r} + \frac{h_\theta^2}{r^2}\left(\frac{1}{r}\frac{\partial v}{\partial \theta} + \frac{u}{r}\right) + \frac{\partial w}{\partial z} + h_r h_\theta\left[\frac{\partial}{\partial r}\left(\frac{v}{r}\right) + \frac{1}{r^2}\frac{\partial u}{\partial \theta}\right] \\ &\quad -\frac{h_\theta}{r}\left(\frac{\partial v}{\partial z} + \frac{1}{r}\frac{\partial w}{\partial \theta}\right) - h_r\left(\frac{\partial w}{\partial r} + \frac{\partial u}{\partial z}\right) \end{aligned} \qquad \text{(A.12)}$$

The tangential stresses are considered next. For each point on the free surface there is a tangent plane on which the shear and thermocapillary stresses are balanced. Two linearly independent, not necessary orthogonal, unit tangent vectors determine the plane and the stresses on the plane. Assume one is independent of the θ-coordinate, $\mathbf{t_1}$, and another is independent of the r-coordinate, $\mathbf{t_2}$. The tangent unit vectors are then

$$\mathbf{t_1} = \frac{1}{(1+h_r^2)^{1/2}}(\mathbf{e_r} + h_r\mathbf{e_z}) \qquad \mathbf{t_2} = \frac{1}{(1+h_\theta^2/r^2)^{1/2}}\left(\mathbf{e}_\theta + \frac{h_\theta}{r}\mathbf{e_z}\right) \qquad \text{(A.13)}$$

The shear stresses can now be written as

$$\sigma_{\tau_1} = -\frac{1}{N(1+h_r^2)^{1/2}}\left[h_r(\tau_{rr}-\tau_{zz}) + \frac{h_\theta}{r}(\tau_{\theta r}+h_r\tau_{\theta z}) - (1-h_r^2)\tau_{zr}\right] \tag{A.14}$$

and

$$\sigma_{\tau_2} = -\frac{1}{N(1+\frac{1}{r^2}h_\theta^2)^{1/2}}\left[\frac{h_\theta}{r}(\tau_{\theta\theta}-\tau_{zz}) - \left(1-\frac{h_\theta^2}{r^2}\right)\tau_{\theta z} + h_r\left(\tau_{r\theta}+\frac{h_\theta}{r}\tau_{zz}\right)\right] \tag{A.15}$$

The tangential shear stresses on the free surface balance the thermocapillary stresses that are caused by the variation of surface tension:

$$\sigma_{\tau_1} = -\gamma\frac{\partial T}{\partial s_1} \qquad \sigma_{\tau_2} = -\gamma\frac{\partial T}{\partial s_2} \tag{A.16}$$

The temperature gradients along the surface can be put into the forms

$$\frac{\partial T}{\partial s_1} = \frac{1}{(1+h_r^2)^{1/2}}\left(\frac{\partial T}{\partial r} + h_r\frac{\partial T}{\partial z}\right) \tag{A.17}$$

and

$$\frac{\partial T}{\partial s_2} = \frac{1}{(1+\frac{1}{r^2}h_\theta^2)^{1/2}}\left(\frac{1}{r}\frac{\partial T}{\partial \theta} + \frac{h_\theta}{r}\frac{\partial T}{\partial z}\right)$$

The non-dimensional form of the tangential stress balances can now be written as

$$\begin{aligned}\frac{1}{N}\Bigg\{2h_r\left(\frac{\partial u}{\partial r}-\frac{\partial w}{\partial z}\right) + \frac{h_\theta}{r}\left[\frac{1}{r}\frac{\partial u}{\partial\theta} + r\frac{\partial}{\partial r}\left(\frac{v}{r}\right) + h_r\left(\frac{\partial v}{\partial z}+\frac{1}{r}\frac{\partial w}{\partial\theta}\right)\right] \\ - (1-h_r^2)\left(\frac{\partial w}{\partial r}+\frac{\partial u}{\partial z}\right)\Bigg\} \;=\; \frac{\partial T}{\partial r} + h_r\frac{\partial T}{\partial z}\end{aligned} \tag{A.18}$$

and

$$\frac{1}{N}\left\{\frac{2h_\theta}{r}\left[\left(\frac{1}{r}\frac{\partial v}{\partial \theta}+\frac{u}{r}\right)-\frac{\partial w}{\partial z}\right]+h_r\left[\frac{1}{r}\frac{\partial u}{\partial \theta}+r\frac{\partial}{\partial r}\left(\frac{v}{r}\right)+\frac{h_\theta}{r}\left(\frac{\partial w}{\partial r}+\frac{\partial u}{\partial z}\right)\right]\right.$$
$$\left.-\left(1-\frac{h_\theta^2}{r^2}\right)\left(\frac{\partial v}{\partial z}+\frac{1}{r}\frac{\partial w}{\partial \theta}\right)\right\}=\frac{1}{r}\frac{\partial T}{\partial \theta}+\frac{h_\theta}{r}\frac{\partial T}{\partial z} \tag{A.19}$$

A.2.3 Energy balance

The energy balance on the free surface is assumed to be insulated,

$$k\frac{\partial T}{\partial n}=0 \tag{A.20}$$

in which the temperature variation normal to the surface is

$$\frac{\partial T}{\partial n}=\mathbf{n}\cdot\nabla T=-\frac{1}{N}\left(h_r\frac{\partial T}{\partial r}+\frac{h_\theta}{r^2}\frac{\partial T}{\partial \theta}-\frac{\partial T}{\partial z}\right) \tag{A.21}$$

Introducing the dimensionless temperature $T'=(T-T_\infty)/(T_1-T_\infty)$ and the Biot number $B_i=\hbar\ H/k$ yields the energy balance on the free surface in a nondimensional form after the primes are dropped

$$-\frac{1}{N}\left(h_r\frac{\partial T}{\partial r}+\frac{h_\theta}{r^2}\frac{\partial T}{\partial \theta}-\frac{\partial T}{\partial z}\right)=0 \tag{A.22}$$

A.2.4 Global mass conservation

As the liquid is incompressible, its total volume remains unchanged,

$$\int_{r_{in}}^{r_{out}}\int_0^{2\pi}h(r,\theta,t)\,r\,dr\,d\theta=0 \tag{A.23}$$

This condition makes the problem well-posed. As the pressure field is determined only to an additive constant, (A.23) can be used to determine this constant.

A.2.5 Boundary conditions for free surface deflection

Two types of contact can be specified on the inner and outer cylinder walls [60]. Either the liquid sticks to a sharp edge at the end walls, in which case

$$h(r_{in}, \theta, t) = h(r_{out}, \theta, t) = 0 \tag{A.24}$$

or the contact angles ϑ_1 and ϑ_2 are prescribed on each end wall as

$$h_r(r_{in}, \theta, t) = -\cot(\vartheta_1) \qquad h_r(r_{out}, \theta, t) = \cot(\vartheta_2) \tag{A.25}$$

Sen and Davis [60] calculated surface shape in both cases, while Zebib et al. [67] considered the first case only. The problem in reality may be different from either of these two cases. The second case is considered in this study.

In addition, the free surface deflection must be periodic in the θ-direction,

$$h(r, \theta + 2\pi, t) = h(r, \theta, t) \tag{A.26}$$

A.3 Numerical method

The numerical procedure is complicated by the deflected and time dependent free boundary conditions. First, the equations for the boundary conditions themselves are complicated nonlinear partial differential equations. Five equations, kinematic

condition, normal stress balance, two tangential stress balances, and energy equation, yield the boundary conditions for the Poisson equation and other governing equations (Navier-Stokes energy equations). Second, the geometry is irregular and time dependent; thus, a grid transformation, which maps the physical domain to a regular computational domain, needs to be carried out for each time step.

All iteration schemes employ a similar strategy [48]. For each time step the shape of the free surface is first chosen by an informed guess. The governing equations for the entire domain are then solved in the transformed grid, but only four of the five free boundary equations are satisfied. The residue in the fifth equation is then used to decide how to alter the shape of the free surface. The process is repeated to convergence and then carried on to the next time step.

Iteration schemes can be classified according to which of the boundary conditions is used as the criterion for relocating the free surface [48]. In stream-surface schemes the kinematic boundary condition is employed, a new approximation to the position of the surface streamline being found from the velocity field determined with the preceding approximation. Normal stress schemes are those in which the imbalance in the normal-stress boundary condition is the basis for improving the surface location. Tangential-stress schemes would be those in which the residual viscous shear stress at the boundary is used, but no attempts have been reported that are based on these schemes.

In general, iterations on the normal stress condition are likely to converge [61] unless the surface tension is very small. The reason is that the kinematic and tangential stress boundary conditions depend on surface orientation but not on curvature whereas the normal stress boundary condition depends on the mean surface curvature of the surface, which is determined by the second derivatives of surface position. Thus, the normal stress condition is the least accurately known of the three conditions at any given state of a numerical solution.

A.3.1 Grid transformation

Existence of surface deflection h makes the physical domain in r-θ-z coordinates irregular. This domain can be transformed into a regular computation domain in ξ-ϑ-η-coordinates by using an algebraic method. To generate a uniform domain, we simply define

$$\xi = r, \qquad \vartheta = \theta, \qquad \eta = \frac{z}{1 + h(r, \theta)} \tag{A.27}$$

The nonuniform grid generation can be obtained by multiplying (A.27) with (3.24). The derivatives of h are evaluated as

$$\frac{\partial}{\partial z} = \frac{1}{1 + h(r, \theta)} \frac{\partial}{\partial \eta}, \qquad \frac{\partial^2}{\partial z^2} = \frac{1}{(1 + h(r, \theta))^2} \frac{\partial^2}{\partial \eta^2} \tag{A.28}$$

A.3.2 Normal stress iteration

In the procedure described in the following sections the normal stress iteration scheme is used to determine the free surface shape. The normal stress balance is employed to

calculate the surface deflection; the other conditions serve as the boundary conditions of the field variables. The procedure is described as follows:

1. Calculate the surface deflection from the normal stress balance. The normal stress balance (A.12) is simplified so that the Laplacian operator on h is kept on the unknown left-hand side while the other terms are moved to the right-hand side and are assigned the known values obtained from the previous iteration. That is,

$$\nabla^2 h^{n+1} \equiv \frac{\partial^2 h}{\partial r^2} + \frac{1}{r}\frac{\partial h}{\partial r} + \frac{1}{r^2}\frac{\partial^2 h}{\partial \theta^2} = c^n \tag{A.29}$$

with

$$c = -\frac{2C_a\ N}{1-\gamma(T-T_0)}\left\{h_r^2\frac{\partial u}{\partial r} + \frac{1}{r^2}h_\theta^2\left(\frac{1}{r}\frac{\partial v}{\partial \theta} + \frac{u}{r}\right) + \frac{\partial w}{\partial z}\right.$$

$$+ h_r h_\theta\left[\frac{\partial}{\partial r}\left(\frac{v}{r}\right) + \frac{1}{r^2}\frac{\partial u}{\partial \theta}\right] - \frac{1}{r}h_\theta\left(\frac{\partial v}{\partial z} + \frac{1}{r}\frac{\partial w}{\partial \theta}\right) - h_r\left(\frac{\partial w}{\partial r} + \frac{\partial u}{\partial z}\right)$$

$$\left. + \frac{1}{2}R_e\ N^2 p\right\}$$

$$-\frac{2}{r^2}h_r h_\theta\left(\frac{1}{r}h_\theta - h_{r\theta}\right) - \frac{1}{r^2}h_\theta^2 h_{rr} - \frac{1}{r}h_r^3 - \frac{1}{r^2}h_r^2 h_{\theta\theta} \tag{A.30}$$

The left-hand side of (A.29) is unknown at the time step $n+1$. The terms on the right hand side are the known from the time step n. Both sides of (A.29) are discretized by second-order central differences. The same procedure used in solving (3.27) can be used to solve (A.29), and the boundary conditions are treated in the same way.

2. Transform the grids to computational grids according to Eq. A.27.

3. Calculate the field variables p, u, v, w, and T by using the algorithm described in Chapter III. The boundary conditions are the same except on the free surface. The following treatments are used for the surface conditions:

   (a) The kinematic condition is used for the boundary condition of the vertical velocity,

$$w^{n+1}(z = 1 + h) = u\delta_r h + \frac{v}{r}\delta_\theta h + \frac{1}{\Delta t}(h^{n+1} - h^n) \tag{A.31}$$

   Here h^{n+1} is a known quantity from the previous iteration at the current time step $(n + 1)$th, and h^n is the deflection from the previous time step.

   (b) The tangential stress balances are used for the boundary conditions of radial velocity u and the angular velocity v.

$$\delta_z^- u^{n+1}(z = 1 + h) = \frac{1}{1 - (\delta_r h)^2}\Big[2\delta_r h(\delta_r u - \delta_z^- w - \frac{v}{r})$$

$$+\frac{1}{r}\delta_\theta h\left(\frac{1}{r}\delta_\theta u + \delta_r v - \frac{v}{r}\right) + \frac{1}{r}\delta_r h\,\delta_\theta h\left(\delta_z v + \frac{1}{r}\delta_\theta w\right)$$

$$-N(\delta_r T + \delta_r h\delta_z^- T)\Big] - \delta_r w \tag{A.32}$$

$$\delta_z^- v^{n+1}(z = 1 + h) = \frac{1}{1 - \frac{1}{r^2}(\delta_\theta h)^2}\left[\frac{2}{r}\delta_\theta h\left(\frac{1}{r}\delta_\theta v + \frac{u}{r} - \delta_z^- w\right)\right.$$

$$+\delta_r h\left(\frac{1}{r}\delta_\theta u + \delta_r v - \frac{v}{r}\right) + \frac{1}{r}\delta_r h\,\delta_\theta h(\delta_r w + \delta_z^- u)$$

$$\left.-N\left(\frac{1}{r}\delta_\theta T + \frac{1}{r}\delta_\theta h\delta_z^- T\right)\right] - \frac{1}{r}\delta_\theta w \tag{A.33}$$

The symbols δ and δ^- represent central and backward operators on the variables, respectively. $\mathcal{N}$ is the numerical representation of N

$$\mathcal{N} = \left[1 + (\delta_r h)^2 + \frac{1}{r^2}(\delta_\theta h)^2\right]^{1/2}$$

(c) The energy equation is used for the temperature boundary condition,

$$\delta_z^- T^{n+1}(z = 1 + h) = \delta_r h\, \delta_r T + \frac{1}{r^2}\delta_\theta h\, \delta_\theta T + N\, B_i\, T \tag{A.34}$$

(d) The pressure boundary condition is treated in the same manner as in the previous chapter for the Neumann conditions.

4. Repeat steps 1 to 3 until h value converges to a required accuracy.

5. Start for the next time step and repeat steps 1 to 4, until a steady solution or an oscillatory flow appears.

BIBLIOGRAPHY

[1] S. Abdallah. Numerical solutions for the pressure Poisson equation with Neumann boundary conditions using a non-staggerd grid, I. *Journal of Computational Physics*, 70:182–192, 12 1987.

[2] S. Abdallah. Numerical solutions for the pressure Poisson equation with Neumann boundary conditions using a non-staggerd grid, II. *Journal of Computational Physics*, 70:193–202, 12 1987.

[3] R.K. Agarwal. A third-order-accurate upwind scheme for Navier-Stokes solutions in three dimensions. In *Proceedings of the ASME/AIAA Conference on Computers in Flow Predictions and Fluid Dynamics Experiments, Washington, D.C*, pages 73–82, 1981.

[4] G. Ahlers, D.S. Cannell, and V. Steinberg. Time-dependence of flow patterns near the convective threshold in a cylindrical container. *Phys. Rev. lett.*, 54:1373–1376, 1985.

[5] C.D. Andereck, S.S. Liu, , and H.L. Swinney. Flow regimes in a circular Couette system with independently rotating cylinders. *Journal of Fluid Mechanics*, 164:155–183, 1986.

[6] D.A. Anderson, J.C. Tannehill, and R.H. Fletcher. *Computational Fluid Mechanics and Heat Transfer*. Series in Computational methods in mechanics and thermal sciences. McGraw-Hill, 1984.

[7] A. Aziz and J.D. Hellums. Numerical solution of the three-dimensional equations of motion for laminar natural convection. *The Physics of Fluids*, 10:314–324, 1967.

[8] V. Babu. *On the Numerical Solution of Incompressible Three-Dimensional Navier-Stokes Equations*. PhD thesis, Ohio State University, 1991. Advisor: S. A. Korpela.

[9] V. Babu and S.A. Korpela. On the direct solution of Poisson's equation on a non-uniform grid. *Journal of Computational Physics*, 104:93–98, 1993.

[10] J.B. Bell, P. Colella, and H.M. Glaz. A second-order projection method for the incompressible Navier-Stokes equations. *Journal of Computational Physics*, 85:257–283, 1989.

[11] W.R. Briley. Numerical method for predicting three-dimensional steady viscous flow in ducts. *Journal of Computational Physics*, 14:8–28, 1974.

[12] W.R. Briley and H. McDonald. On the structure and use of linearized block implicit schemes. *Journal of Computational Physics*, 34:54–73, 1980.

[13] D.L. Brown, R. Cortez, and M.L. Minion. Accurate projection methods for the incompressible Navier-Stokes equations. *Journal of Computational Physics*, 168:464–499, 2001.

[14] O.R. Burggraf. Analytical and numerical studies of the structure of steady seperated flows. *Journal of Fluid Mechanics*, 24:113–151, 1966.

[15] B. L. Buzbee, G. H. Golub, and C. W. Nielson. On the direct methods for solving Poisson's equations. *SIAM Journal on Numerical Analysis*, 7(4):627–656, 12 1970.

[16] S. Chandrasekhar. *Hydrodynamic and Hydromagnetic Stability*. Oxford at the Clarkndon Press, 1961.

[17] A.J. Chorin. A numerical method for solving incompressible viscous flow problems. *Journal of Computational Physics*, 2(1):12–26, 1967.

[18] A.J. Chorin. Numerical solution of the Navier-Stokes equations. *Mathematics of Computation*, 22(104):745–762, 1968.

[19] A.J. Chorin. On the convergence of discrete approximations to the Navier-Stokes equations. *Mathematics of Computation*, 23(106):341–353, 1969.

[20] D. Coles. Transition in circular Couette flow. *Journal of Fluid Mechanics*, 21:385–425, 1965.

[21] K.T. Coughlin and P.S. Marcus. Modulated waves in Taylor-Couette flow part 2. numerical simulation. *Journal of Fluid Mechanics*, 234:19–46, 1992.

[22] V. Croquette. Convective pattern dynamics at low Prandtl number: Part I. *Contemp. Phy.*, 30:113–133, 1989.

[23] V. Croquette. Convective pattern dynamics at low Prandtl number: Part II. *Contemp. Phy.*, 30:153–171, 1989.

[24] S.C.R. Dennis, D.B. Ingham, , and R.N. Cook. Finite-difference methods for calculating steady incompressible flows in three dimensions. *Jounral of Computational Physics*, 33:325–339, 1979.

[25] J.H. Ferziger and M. Peric. *Computational mathods for fluid dynamics*. Springer, 1999.

[26] J. Fromm and F.H. Harlow. Numerical solution of the problem of vortex sheet development. *Physics of Fluids*, 6:975, 1963.

[27] K.N. Ghia, W.L. Hankey, , and J.K. Hodge. Study of incompressible Navier-Stokes equations in primitive variables using implicit numerical technique. *AIAA J.*, 17:298, 1979.

[28] U. Ghia, K.N. Ghia, and C.T. Shin. High-re solutions for incompressible flow using the Navier-Stokes equations and a multigrid method. *Journal of Computational Physics*, 48:347–411, 1982.

[29] U. Ghia, K.N. Ghia, and C.J. Studerus. Three-dimensional laminar incompressible flow in straight polar ducts. *Computer and Fluids*, 5:205–218, 1976.

[30] K. Goda. A multistep technique with implicit difference schemes for calculating two- or three-dimensional cavity flows. *Journal of Computational Physics*, 30:76–95, 1979.

[31] M. Gorman and H.L. Swinney. Spatial and temporal characteristics of modulated waves in the circular Couette system. *Journal of Fluid Mechanics*, 117:123–142, 1982.

[32] P.M. Gresho and R.L. Sani. On the pressure boundary conditions for the incompressible Navier-Stokes equations. *International Journal for Numerical Methods in Fluids*, 7:1111–1145, 1987.

[33] F.H. Harlow and J.E. Welch. Numerical calculation of time-dependent viscous incompressible flow of fluid with free surface. *Physics of Fluids*, 8(12):2182–2188, December 1965.

[34] M. Kawaguti. Numerical solution of the Navier-Stokes equations for the flow in a two-dimensional cavity. *Journal of Physical Society of Japan*, 16(11), 1961.

[35] R. Keunings. An algorithm for the simulation of transient viscoelastic flows with free surface. *Journal of Computational Physics*, 62:199–220, 1986.

[36] J. Kim and P. Moin. Application of a fractional-step method to incompressible Navier-Stokes interaction in two and three dimensions. *Journal of Computational Physics*, 59, 1985.

[37] S.A. Korpela. *Convection Heat Transfer*. Unpublished, 1993.

[38] S.A. Korpela and Patrick Lequéré. *Hydrodynamic and Thermal Instability*. Unpublished, 1990.

[39] E.L. Koschmieder. *Bénard Cells and Taylor Vortices*. Cambridge University Press, 1993.

[40] G.D. Mallinson and G. de Vahl Davis. The method of the false transient for the solution of coupled elliptic equations. *Journal of Computational Physics*, 12:435–61, 1973.

[41] P.S. Marcus. Simulation of Taylor-Couette flow. part 1. numerical methods and comparison with experiment. *Journal of Fluid Mechanics*, 146:45–64, 1984.

[42] P.S. Marcus. Simulation of Taylor-Couette flow. part 2. numerical results for wavy-vortex flow with on etraveling wave. *Journal of Fluid Mechanics*, 146:65–113, 1984.

[43] K.A. Meyer. Los Alamos Rep. LA-3497. 1966.

[44] K.A. Meyer. Los Alamos Rep. LA-4202. 1966.

[45] K.A. Meyer. Three-dimensional study of flows between concentric rotating cylinders. *Phys. Fluids Suppl.*, 12:II.165–II.170, 1969b.

[46] K. Miyakoda. *Japan J. Geophys.*, 14:8, 1962.

[47] S. Nakamura. *Applied Numerical Methods with Software*. Prentice-Hall, New Jersey, 1991.

[48] F.M. Orr and L.E. Scriven. Rimming flow: numerical simulation of steady, viscous, free-surface flow with surface tension. *J. Fluid Mech.*, 84:146–155, 1978.

[49] G.A. Osswald, K.N. Ghia, and U. Ghia. A direct algorithm for the solution of incompressible three-dimensional unsteady Navier-Stokes equations. *AIAA Paper*, 87:1139, 1987.

[50] S.V. Pantankar. *Numerical Heat Transfer and Fluid Flow*. Hemisphere Publishing Corporation, New York, 1980.

[51] S.V. Patankar and D.B. Spalding. A calculation procedure for heat, mass and momentum transfer in three-dimensional parabolic flows. *International Journal of Heat and Mass Transfer*, 15:1787–1806, 1972.

[52] M.R. Paul and I. Catton. The relexation of two-dimensional rols in Rayleigh-Bénard convection. *Physics of Fluids*, 16(5):1262–1266, 2004.

[53] M.R. Paul, K.-H Chaim, M.C. Cross, P.F. Fischer, and H.S. Greenside. Pattern formation and dynamics in Rayleigh-Bénard convection: numerical simulation of experimentally realistic geometries. *Physica D*, 184:114–126, 2003.

[54] V.I. Polezhaev and V.P. Yaremchuk. Numerical modeling of unsteady two-dimensional convection in a finite-length horizontal layer heated from below. *Fluid Dynamics*, 36(4):556–565, 2001.

[55] N. Ramanan. *Multi-grid Solution of Thermocapillary Convection in Weld Pools*. PhD thesis, The Ohio State University, 1988. Advisor: S. A. Korpela.

[56] N. Ramanan and S.A. Korpela. Thermocapillary convection in an axi-symmetric pool. *Computers & Fluids*, 18:205–215, 1990.

[57] Lord Rayleigh. On convection currents in a horizontal layer of fluid when the high temperature is on the under side. *Phil. Mag.*, 32:529–546, 1916.

[58] Lord Rayleigh. On the dynamics of revolving fluids. *Proc. Roy. Soc. London*, A 93:148–154, 1916.

[59] H. Schlichting. *Boundary-Layer Theory*. McGraw-Hill, 1979.

[60] A.K. Sen and S.H. Davis. Steady thermocapillary flows in two-dimensional slots. *J. Fluid Mech.*, 121:163–186, 1982.

[61] W.J. Silliman and L.E. Scriven. Separating flow near a static contact line: Slip at a wall and shape of a free surface. *Journal of Computational Physics*, 34:287–313, 1980.

[62] F. Sotiropoulos and S. Abdallah. Coupled fully implicit solution procedure for the steady incompressible Navier-Stokes equations. *Journal of Computational Physics*, 87:328–348, 12 1990.

[63] J. C. Strikwerda and Y. M. Nagel. A numerical method for the incompressible Navier-Stokes equations in three-dimensional cylindrical geometry. *Journal of Computational Physics*, 78:64–78, 1988.

[64] H. Takami and K. Kuwahara. Numerical study of three-dimensional flow within a cubic cavity. *Journal of the Physical Society of Japan*, 37(6):1695–1698, 1974.

[65] G.I. Taylor. Stability of a viscous liquid contained between two rotating cylinders. *Phil. Trans. R. Soc. Lond.*, A(223):289–343, 1923.

[66] Y. Zang and R.L. Street. A composite multigrid method for calculating unsteady incompressible flows in geometrically complex domains. *Internaltional Journal of Numerical Methods in Fluids*, 20:341–361, 1995.

[67] A. Zebib, G. M. Homsy, and E. Meiburg. High Marangoni number convection in a squar cavity. *Physics of Fluids*, 28:3467–3476, 1985.